EXPERIMENTAL STUDY OF X-BAND DIELECTRIC-LOADED ACCELERATING STRUCTURES

BY

CHUNGUANG JING

DEPARTMENT OF ELECTRICAL AND COMPUTER ENGINEERING

Submitted in partial fulfillment of the
requirements for the degree of
Doctor of Philosophy in Electrical Engineering
in the Graduate College of the
Illinois Institute of Technology

Approved _____
Adviser

Chicago, Illinois
May 2005

ACKNOWLEDGEMENT

I am greatly honored to write this dissertation as a tribute to the great efforts many people have devoted to the research program, X-Band Dielectric Loaded Accelerator Structures. I could not have accomplished this dissertation without the help of many friends, colleagues, fellows, and my family.

I would like to thank my advisor, Prof. Thomas Wong, for steering me into the area of microwave engineering, and for his consistent advice and help during the period of my study at Illinois Institute of Technology. I am deeply grateful to Dr. Wei Gai, the leader of Argonne Wakefield Accelerator group in Argonne National Laboratory, for his inspiring guidance and strong encouragement when I was carrying out the research in his group. It has really been a precious experience for me to participate in the research work with all the fellows of the accelerator R&D group. I have been receiving the expert support from Dr. Wanming Liu in the EM simulation and structure design. I also have to express my gratitude to Mr. Richard Konecny for his valuable advice and great cooperation along the whole program. I would like to acknowledge Dr. Manuel Conde, Dr. John Power, Dr. Zikri Yusof, Mr. Felipe Franchini, and Mr. Haitao Wang for their active involvement throughout. Dr. Steve H Gold and Mr. Allen K. Kinkead are such good collaborators when I carried out all high power RF experiments at Naval Research Laboratory. I would like to thank them sincerely. This research program is supported by US Department of Energy, High Energy Physics Division, Advanced Technology Branch, under the contract No. W-31-109-ENG-38, and is conducted at the Accelerator R&D Group of High Energy Physics Division of Argonne National Laboratory.

This dissertation is dedicated to my parents and my wife. I feel deeply indebted to their love and consistent support that walked me through this journey. Again, my endless love goes to my wife, Jian.

TABLE OF CONTENTS

Page

ACKNOWLEDGEMENT iii

LIST OF TABLES vi

LIST OF FIGURES vii

LIST OF SYMBOLS xi

ABSTRACT xiv

CHAPTER

1. INTRODUCTION 1

1.1 Advanced Accelerator Concepts 1
1.2 Review of Dielectric-Loaded Accelerator 4
1.3 NRL/ANL Dielectric-Loaded Accelerator Test Facility 10
1.4 Organization of the Thesis 13

2. THEORY OF DIELECTRIC-LOADED ACCELERATING STRUCTURES 15

2.1 Electromagnetic Characteristics 15
2.2 Accelerating Parameters 22
2.3 Wakefields Calculation 25

3. TESTING ON X-BAND DIELECTRIC-LOADED ACCELERATING STRUCURES 40

3.1 Design and Fabrication 42
3.2 Bench Testing 54
3.3 Multipactor of Alumina Based DLA Structures 63
3.4 Local Field Enhancement of $Mg_xCa_{1-x}TiO_3$ Based DLA Structures 76

4. MULTILAYERED DIELECTRIC-LOADED ACCELERATING STRUCTURE 90

4.1 Introduction 90
4.2 Theoretical Analysis 93
4.3 Design of X-Band Four-layered DLA Structure 102
4.4 Parasitic Modes Damping 104

5. CONCLUSION 113

APPENDIX

A. RESONATE LOOP TECHNIQUE 117

B. DIRIECT WAKEFIELD MEASUREMENT 122

BIBLIOGRAPHY 123

LIST OF TABLES

Table Page

2.1 Geometric and Physical Properties of the 11.424GHz DLA Structures..... 26

4.1 Accelerating Modes RF Parameters Comparison for Different DLA Structure. 103

4.2 Parasitic Modes RF Parameters Comparison for Multilayered and Single Layered DLA Structures 110

LIST OF FIGURES

Figure Page

1.1 The Beamline of the Argonne Wakefield Accelerator (AWA) Facility..... 8

1.2 The New L-band 1.5 Cell Drive Gun and Test Beamline at AWA Facility.... 9

1.3 Couplers Developed at Argonne National Laboratory 11

1.4 Schematic Drawing of NRL/ANL Compact Dielectric-Loaded Accelerator Test Facility..... 12

2.1 Partially Dielectric-Loaded Circular Waveguide for Particle Acceleration. The Dielectric Tube has Inner Radius a and Outer Radius b..... 17

2.2 The Amplitude of Ez of the TM01 Mode along the Transverse Radius of the Dielectric-lined Circular Waveguide 20

2.3 The Propagation Constants of the TM01 Mode and the HEM11 Mode versus Frequency in the Dielectric-lined Circular Waveguide..... 21

2.4 Schematic Dielectric-Loaded Wakefields Structure 29

2.5 The Longitudinal Wakefield for the Monopole Mode (Beam Traverses on the Axial of the Circular DLA Structure) 33

2.6 Dielectric-Loaded Rectangular Waveguide 35

2.7 Calculated Longitudinal Wakefield in an X-Band Rectangular DLA Structure Using the Indirect Computational Method..... 39

3.1 The Schematic Drawing of the Modular Dielectric-Loaded Accelerating Structure Which Consists of Three Functional Parts: RF Input/Output Coupler; Tapered Impedance Matching Section; Central Particle Acceleration Section 41

3.2 Major Simulation Parameters for Optimizing Single Port Coupler 43

3.3 Electric Distribution of Single Port Coupler by Microwave Studio®. 44

3.4 Simulation Results of S-parameter for the Single Port Coupler by Microwave Studio®..... 45

3.5 The Tapered Impedance Matching Section of the Modular DLA Structure... 47

3.6 Simulated S-parameters with respect to the Dielectric Constant Varies 48

3.7 The New Dielectric Taper Design for MgxCa1-xTiO3 Based DLA Structure (with Dielectric Constant of 20) 49

3.8 With Properly Selected Dielectric Constant and Loading Geometry, the Wave in the Dielectric Loaded Accelerating Structure will Travel at the Speed of Light and its Pattern is Good for Accelerating the Particles at the Given Frequency, here, 11.424GHz 51

3.9 Mechanic Drawing of Designed Modular Accelerating Structure 52

3.10 Finished 11.424 GHz Dielectric Loaded Modular Accelerating Structure..... 53

3.11 Modular Accelerating Structure under Test by HP8510C Network Analyzer 56

3.12 Comparison of Transmission Performance, S21, Between the Measurement and Simulation Results of the Coupler to Coupler..... 57

3.13 Comparison of Transmission Performance, S21, Between the Measurement and Simulation Results of the Complete DLA Structure 58

3.14 MCT DLA Structure Bench Test Results before High Power RF Test at the Naval Research Laboratory 59

3.15 Block Diagram of the Time Response Test Bench 61

3.16 200ns Long Pulsed RF Response..... 62

3.17 Experimental Setup Used to Test DLA Structures with High Power RF 65

3.18 Alumina Based DLA Structure High Power Test Data 67

3.19 Model of Single-Surface Multipactor with Both Normal and Tangential RF Fields and Normal DC Field Caused by an Electron Cloud of Thickness t (shaded) in the Cylindrical DLA Structure..... 70

3.20 Comparison of Experimental Missing Power Data to the Model 73

3.21 Comparison of the Power Transmission Curves for the Coated and Non-Coated Alumina DLA Structures 75

3.22 Transmitted RF Power as a Function of Incident Power with and without an Axial Magnetic Field Applied..... 77

3.23 The High Power RF Testing Data of MCT DLA Structure 80

3.24 Bright Spot Observed During the High Power Testing of the MCT Based DLA Structure 81

3.25 Breakdown Signature of $Mg_xCa_{1-x}TiO_3$ Tube During the High Power RF Testing on MCT Based DLA Structure 82

3.26 Numerical Simulation Demonstrates the Field Enhancement in the Small Vacuum Gap. From the Magnified Picture on the Bottom, It Shows the Highest Electric Field Built Up in the Vacuum Gap 84

3.27 S-parameter of the Ceramic Joint Bonded MCT DLA Structure 86

3.28 High Power RF Response of the Epoxy Bonded MCT DLA Structure. 88

3.29 Comparison of High Power RF Transmission of Two Experiments, the Non-epoxy MCT DLA Structure and the Epoxy Bonding One 89

4.1 Cross-Section of the Multilayered Dielectric-Loaded Accelerating (DLA) Structure 92

4.2 Profile of Longitudinal Electric Fields for Several TM Modes and Parasitic Modes Built In a 4-layer Dielectric-Loaded Accelerating Structure 99

4.3 Dispersion Relations of Several Low Order Modes in 4-layer Dielectric-Loaded Metallic Cylindrical Waveguide with Same Dimension as Figure 4.2 100

4.4 Longitudinal Electric Field Distribution of Some Lower Order Modes in Cross-section of the 4-layer Dielectric-Loaded Waveguide Which Has Same Dimensions as Shown in Figure 4.2 101

4.5 Effect of Both Vacuum Core Size and Dielectric Permittivity Ratio on the Group Velocity. Still, This Model is Based on 4-layer Structure 105

4.6 Effect of Both Vacuum Core Size and Dielectric Permittivity Ratio on the R/Q. Still, This Model is Based on 4-layer Structure 106

4.7 Effect of Both Vacuum Core Size and Dielectric Permittivity Ratio on the Shunt Impedance. Still, This Model is Based on 4-layer Structure 107

4.8 Effect of Both Vacuum Core Size and Dielectric Permittivity Ratio on the Power Attenuation. Still, This Model is Based on 4-layer Structure 108

4.9 Parasitic Modes Damping by Thin Ferrite Foil. Dashed Lines Represent Longitudinal Electric Field without Damping and Solid Lines are those After Damping 112

A1 Diagram of the Active Bead-pull System. 118

A2 EM Field of the TM01 Mode in the L-Band Cavity 119

A3 The Phase and Amplitude Responses of the Resonant Loop by the Phase Scan 120

A4 Electric Field at the Center of the Cavity by Beadpull Experiment 120

B1 Block Diagram of Wakefield RF Measurement Technique 124

B2 Wakefield Signal Detected by a Fast Response Diode. The Charge is around 1nC 124

B3 Down Converted Wakefield Signal with the Major Frequency Shown at 3.4GHz 125

B4 Restored Wakefield Signal 125

B5 Synchronized Frequency of TM_{01} Mode vs. Dielectric Constant of the Loaded Ceramic tube 126

LIST OF SYMBOLS

Symbol	Definition
α_0	field attenuation parameter per unit length in the traveling-wave accelerator
β	longitudinal wave propagation constant relativistic parameter
ε	permittivity of material; dielectric constant of material
ε_0	permittivity of free space
ε_r	relative permittivity, dielectric constant
ρ	charge density
ϕ	phase, scalar potential
λ	wavelength
ω	angular frequency
σ	conductivity
μ	permeability of material
μ_0	permeability of free space
ΔW	energy gain of a given charged particle in accelerator
$\vec{A}$	vector potential
a	inner radius of dielectric-lined circular waveguide; iris radius of iris-loaded periodic structure; iris radius of hybrid dielectric-iris-loaded periodic structure
b	outer radius of dielectric-lined circular waveguide; iris radius of iris-loaded periodic structure; iris radius of hybrid dielectric-iris-loaded periodic structure
c	speed of light in the free space
$\vec{j}$	current density

k_0	wave number of TEM wave in free space
k_1	cutoff wave number of waveguide mode in the vacuum region of the dielectric-lined circular waveguide
k_2	cutoff wave number of waveguide mode in the dielectric region of the dielectric-lined circular waveguide
l	length
q	charge
r	location in r-direction in cylindrical coordinates; shunt impedance per unit length in traveling-wave accelerator
r	shunt impedance
t	time
$tan\delta_l$	loss tangent of dielectric
v_g	group velocity of RF wave
v_p	phase velocity of RF wave
z	location in z-direction in cylindrical coordinates; location along wave propagation
E	electric field magnitude
E_a	peak axial longitudinal electric field amplitude, accelerating field amplitude, acceleration gradient
$\vec{E}_t$	transverse electric field
E_z	longitudinal electric field magnitude
$\vec{E}_z$	longitudinal electric field
H	magnetic field magnitude
H_z	longitudinal magnetic field intensity
$\vec{H}_z$	longitudinal magnetic field

$\vec{H}_t$	transverse magnetic field
P_0	input power
P_{diss}	power dissipation in the structure
Q	quality factor
R_s	surface resistivity
U	time average stored energy per unit length
V	Volume
v	velocity of the charge

ABSTRACT

A joint Argonne National Laboratory (ANL)/ Naval Research Laboratory (NRL) program is under way to investigate X-band dielectric-loaded accelerating (DLA) structures, using high-power 11.424GHz radiation from the NRL Magnicon facility. As an advanced accelerator concepts, the dielectric-loaded accelerator offers the potential for a simple, inexpensive alternative to high-gradient RF linear accelerators. In this thesis, a comprehensive account of X-band DLA structure design, including theoretical calculation, numerical simulation, fabrication and testing, is presented in detail. Two types of loading dielectrics, alumina and $Mg_xCa_{1-x}TiO_3$ (MCT), are investigated. For alumina (with dielectric constant 9.4), no RF breakdown has been observed up to 5 MW of drive power (equivalent to 8MV/m accelerating gradient) in the high power RF testing at NRL, but multipactor was observed to absorb a large fraction of the incident microwave power. Experimental results on suppression of multipactor using TiN coating on the inner surface of the dielectric are also reported. For MCT (with dielectric constant 20), although we did not observe dielectric breakdown in the structures, breakdown did occur at the ceramic joint, where the electric field is greatly enhanced (estimated to be around 100MV/m) due to the micro-scale vacuum gap. In addition, the MCT structure showed significantly less multipactor for the same level of RF field. The thesis also introduced a new design, a multilayered dielectric-loaded accelerating structure, to improve the performance over the conventional one layer DLA structure. Results of analysis for the case of a four layered DLA structure indicate a large reduction of RF power attenuation and an increase of shunt impedance for the structure.

Beyond the main contents, the appendices of the thesis present two individual projects prompted by the experimental study of the dielectric-loaded accelerating structure. Appendix A shows a resonant loop technique that can be used in the bead-pull experiment on any cavity resonator. In appendix B, a direct wakefield measurement of the dielectric-loaded waveguide on the Argonne Wakefield Accelerator beamline is described.

CHAPTER 1

INTRODUCTION

Although superconducting technology has reached the implementation stage for building the International Linear Collider (ILC), research programs in another area, Advanced Accelerator Concepts (AAC), are still on the uphill side. Not only are some mainstream areas of AAC, like laser and plasma wakefields acceleration [1,2][1], inverse free electron laser accelerator [3,4], dielectric-loaded accelerator [5-7], making progress year by year, but also more exotic ideas have been brought forward, such as vacuum laser acceleration [8], optical bragg accelerating structure [9], and diverse schemes based on left-handed materials [10]. Here, we briefly overview some basic accelerator technologies in AAC regime, while concentrating on introducing the research program of dielectric-loaded accelerator developed at Argonne National Laboratory.

1.1 Advanced Accelerator Concepts

With the development of conventional iris-loaded accelerator, scientists have never stopped bringing up various advanced, even exotic, ideas to extend the limits of current accelerator technologies. Research programs on those advanced accelerator concepts have been sufficiently developed in the recent twenty years. Most of them have gone beyond theoretical studies, and accomplished initial but significant experimental demonstrations. To be briefly introduced in this section are Plasma Wakefield Acceleration (PWFA) and Inverse Free Electron Laser (IFEL) Acceleration. Another

[1] Corresponding to references in the Bibliography

mainstream of AAC, the dielectric-loaded accelerator, will be separately described in the next section.

Plasma Wakefield Acceleration (PWFA). There are two categories of plasma wakefield acceleration scheme defined by the wake driving source in the plasma. One is based on the beam, and the other is the laser. The basic idea for the beam-driven PWFA is to use a high-gradient wakefield induced by an intense, high-energy charged particle beam as it passes through a plasma to accelerate a second appropriately phased accelerating beam which contains fewer particles than the diving beam. The wake happens in the plasma blowout regime, for instance, the space-charge of the electron bunch blows out the plasma electrons, which rush back in and overshoot, setting up a plasma oscillation. The PWFA scheme is very attractive because of its potential to double the beam energy of a high energy accelerator beam in a single stage of acceleration that is only tens of meters long using existing state-of-the-art driver beams [11]. The first demonstration of the excitation of the wakefield by a relativistic beam was at Argonne National Laboratory in 1987. The peak acceleration gradient was just 1.6 MeV/m; however the experiment clearly showed the wakefield persisting for several plasma wavelengths. More recently at Fermilab's AO facility a magnetic chicane was used to compress the electron beam to a few picoseconds. Now the acceleration and deceleration gradients dramatically increased to ~150 MeV/m and some particles of the 15 MeV beam lost nearly all their initially to the plasma wake [12].In contrast to the modest beam energy experiments described above, a collaboration of scientists from SLAC, USC and UCLA are systematically addressing the relevant physics issues in PWFA in order to

realize a prototype of a meter-scale, high-gradient plasma wakefield acceleration stage [13]. In a series of experiments at the Final Focus Test Beam (FFTB) that use the 28.5 GeV electron and positron drive beams from the Stanford Linear Accelerator Center, these researchers have quantitatively elucidated the basic beam physical phenomena that determine the transport of such beams through a meter-scale column of plasma and energy loss (gain) to (from) the plasma wakefield[14].

Similarly, instead of a beam, a Laser driven plasma Wakefield Acceleration (LWFA) uses high intensity laser pulse or pulse train to excite the high gradient wakefield in a plasma guiding channel for accelerating charged particles [15]. In [16], experiments were reported that beams containing electrons with energy up to 200 MeV had been produced, using a 30 TW, 30 fs laser. Whereas the end point energy of the distribution had increased to several hundred MeV, all experiments reported electron distributions that had 100% energy spread, with a small amount of charge at the high energies (<< 1%). At the most recent Advanced Accelerator Concepts workshop (AAC2004), however, three different groups (L'OASIS at LBNL, LOA-France and RAL-UK) presented results on the observation of narrow energy spread beams, with 100 MeV-level mean energies, containing large amounts of charge (order 109 electrons/bunch) [17].All three experiments utilized a short pulse laser system, and extended the distance over which the laser beam remains at high intensity.

Inverse Free Electron Laser (IFEL) Acceleration. The principle of the IFEL acceleration is to accelerate an electron beam through its interaction with high-power laser radiation and a periodic wiggler field. This concept has been pursued at Brookhaven

National Laboratory for several years [18], most recently in the form of low-energy (<1 GeV), high-gradient, multistage, linear accelerators, Staged Electron Laser Acceleration (STELLA) [19]. The basic concept utilized by STELLA is to first group the electrons within the electron-beam (*e*-beam) into microbunches. Briefly, the initial *e*-beam energy is distributed uniformly over all phases of the accelerating electromagnetic wave (i.e., laser beam optical field). A sinusoidal energy modulation is imparted onto the *e*-beam using the intense electric field of the laser beam. This accelerates some of the electrons and decelerates others. The fast electrons are allowed to catch up with the slow ones resulting in grouping ("bunching") of the electrons into tiny clusters ("microbunches"). These microbunches can then be efficiently trapped and accelerated by a second laser acceleration device while maintaining a narrow energy spread. This process of trapping and acceleration by a second device is fundamental to staging multiple laser acceleration sections, which is necessary for enabling high net energy gains.

1.2 Review of Dielectric-Loaded Accelerators

The study of using RF driven dielectric-loaded circular waveguide for particle acceleration can be traced back to the early 1950's [20]. In recent years, because of its geometrical simplicity and availability of low loss dielectrics, the theoretical and experimental investigations on dielectric-loaded accelerating (DLA) structures have been intensively revived [21-24]. In addition to the conventional circular DLA structures, a rectangular structure has also brought much interest [25, 26]. Some related research programs like the Argonne Wakefields Accelerator [27], Argonne National Laboratory/ Naval Research Laboratory joint compact dielectric-loaded accelerator [28], DULY

ceramic RF power extractor [29], Yale's rectangular DLA structure based wakefield accelerator [30], SLAC W-band planar DLA structure [31], etc., have made significant progress on experiments. The advantages and potential problems of using dielectric-loaded waveguide as the accelerating structure are discussed in the above references and are only summarized here. ADVANTAGES: 1) Simplicity of fabrication: The device is simply a tube of dielectric surrounded by a conducting cylinder. The relatively small diameter of device is due to the high dielectric constant of the material used; this small size also facilitates the use of quadrupole lenses around the structure; 2) Potentially higher breakdown threshold than copper but with comparable shunt impedance; 3) Easy higher order mode damping. ISSUES: However, potential challenges of using dielectric materials in a high power RF environment are breakdown caused by the local field enhancement [32] and thermal heating.

Argonne Wakefield Accelerator. The Argonne Wakefield Accelerator (AWA) is specifically designed for accelerator research which requires intense, short pulse electron beams. It supports research that focuses upon the physics and technology of advanced methods to accelerate charged particles, in particular, dielectric based wakefield acceleration.

As shown in Figure 1.1, the AWA facility consists of two beamlines: one is a L-band photocathode RF gun (driven gun) plus two standing wave linac structures that can produce up to 100nC high charge bunches with 20~30 ps FWHM short bunch length at 14 MeV; the other is also a L-band photocathode RF gun (witness gun) that can generate 4 MeV 80~300pC low charge bunches. Both guns, as well as two linac tanks, are

powered by a single 30 MW L-band klystron. The laser system consists of a dye oscillator (496 nm) followed by a dye amplifier and an excimer amplifier; a doubling crystal is followed by a second excimer amplifier (248 nm), bringing the final pulse energy to 8 mJ, with a pulse duration of 6 to 8 ps FWHM. This facility can operate in either a Two Beam Accelerator scheme or a Collinear wakefield accelerator scheme. In the first case, the high intensity beam from the driven gun is used to excite the wakefields in the dielectric-loaded waveguide which is set up at the end of the driving beamline; and the low intensity beam from the witness gun will be accelerated in a high gradient dielectric-loaded accelerating structure which is powered by the RF extracted from the wakefields generated by the driven beam. In the collinear scheme, the high intensity bunches from the driven gun are bent into the witness beamline through a set of magnets, and the low intensity electron bunch from the witness gun will be set to trail behind the driving bunches in a dielectric-loaded structure so that it can be accelerated by the wakefields from the driving bunches if the witness bunch is synchronized at a right phase.

A numbers of milestones have been reached at the AWA facility in the past few years. The group measured the first ever wakefields in the dielectric-loaded waveguide through the witness beam technique [23]; they demonstrated the first ever collinear wakefield acceleration through the proper designed bunch train [33]; they demonstrated the first ever the RF extraction and two beam accelerator concept for the dielectric wakefield step-up transformer [34]; they built and tested the first ever transverse mode suppressor for the dielectric wakefield accelerator [35]; they were the first to complete high gradient dielectric wakefield device measurements [5] and other accomplishments.

Besides the main tasks on studying dielectric-loaded wakefield accelerator, the AWA facility has also been used to investigate high brightness beam [36], high QE photocathode [37], and other related topics.

In order to achieve a higher accelerating gradient in the dielectric-loaded accelerator, we need a higher quality drive beam which has a smaller emittance and shorter bunch length. For this purpose, the AWA facility is currently undergoing several major upgrades [38]. A new photocathode RF gun has been built to replace the old drive beam gun. The new 1.5 cell gun (see Figure 1.2) can produce an 8 MeV beam with 12 MW of RF power. Similar bunch charges (10 - 100 nC) will be generated by the new gun, but with shorter bunch lengths (2 - 5 ps rms) and much lower emittances (30 - 200 n mm mrad). The laser system has also been upgraded. The new system consists of a Spectra Physics Tsunami oscillator followed by a Spitfire regenerative amplifier and two Ti: Sapphire amplifiers (TSA 50). It produces 1.5 mJ pulses at 248 nm, with a pulse length of 6 to 8 ps FWHM and a repetition rate of up to 10 pps.

External RF Driven Dielectric-Loaded Accelerating Structure. The external RF driven DLA structure is a central part of the dielectric based accelerator. Unlike the entirely metal disc-loaded accelerating structure, the DLA structure employs a partially loaded dielectric to slow the wave propagating in the waveguide to the speed of charged particles, which is physically less but close to the speed of light. As we mentioned earlier, the geometry of dielectric-loaded accelerating structure is very simple; for example, the circular DLA structure may be made by just slipping a ceramic tube into a metal circular waveguide. However, there are other practical challenges encountered. The big issue

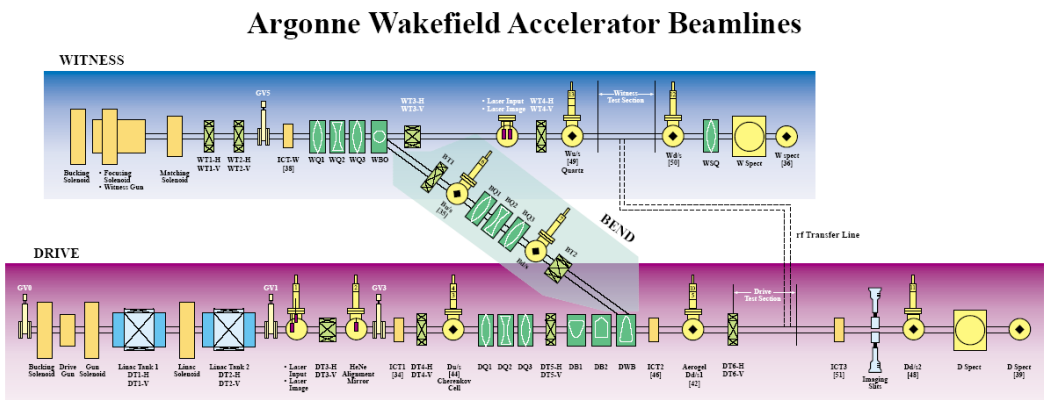

Figure 1.1. The Beamline of the Argonne Wakefield Accelerator (AWA) Facility.

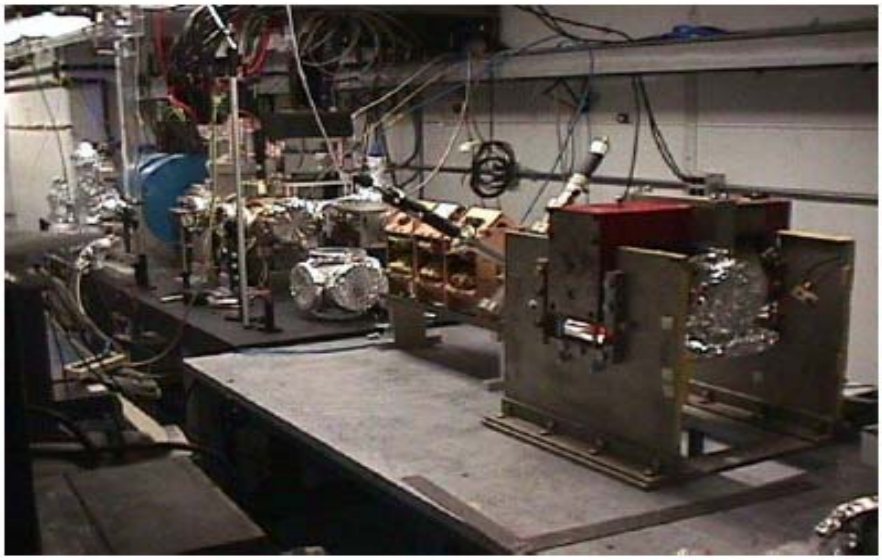

Figure 1.2. The New L-band 1.5 Cell Drive Gun and Test Beamline at AWA Facility.

behind the fabrication of DLA structure is the effective coupling the external RF energy into the dielectric-loaded waveguide. Previous attempts [7, 39] have been made to feed the RF power into the dielectric-loaded waveguide. Figure 1.3(a) and 1.3(b) show two typical coupler designs. The first one is fairly straightforward but it does not have a good coupling efficiency due to no impedance matching between the two waveguide joints. The second design shown in Figure 1.3(b) has a good coupling efficiency because of a tapered dielectric end being added for matching impedance. However, it has been demonstrated to have difficulty in handling a high power due to the coupling slot is near to the dielectric-loaded section so that iris break down can easily occur. In our work, a new coupler, the TE-TM mode converter [40], is designed and fabricated (Figure 1.3(c)). It first transmits the energy by a tapered transition section, and then converts the RF from TM_{01} mode to the TE_{10} mode in a pure metal section, which can provide high efficiency transmission from the dielectric accelerator section to the regular rectangular waveguide. Because there are no dielectrics near the RF coupler, this scheme overcomes RF breakdown problems near the coupling holes that occurred in the older designs. In addition, it is less sensitive to machine errors than the previous designs. A detailed design study will be presented in Chapter 3.

1.3 NRL/ANL Dielectric-Loaded Accelerator Test Facility

To demonstrate the feasibility of the dielectric-loaded accelerator as a high gradient accelerator and study the related physical phenomena as well, the Naval Research Laboratory (NRL) and Argonne National Laboratory (ANL) are constructing a 20MeV compact dielectric-loaded accelerator test facility [28]. The facility, shown in

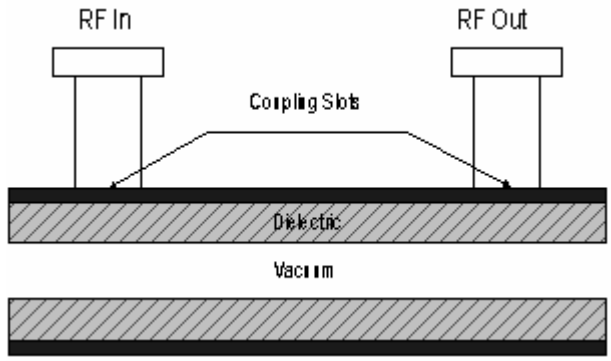

(a) Direct coupling slot.

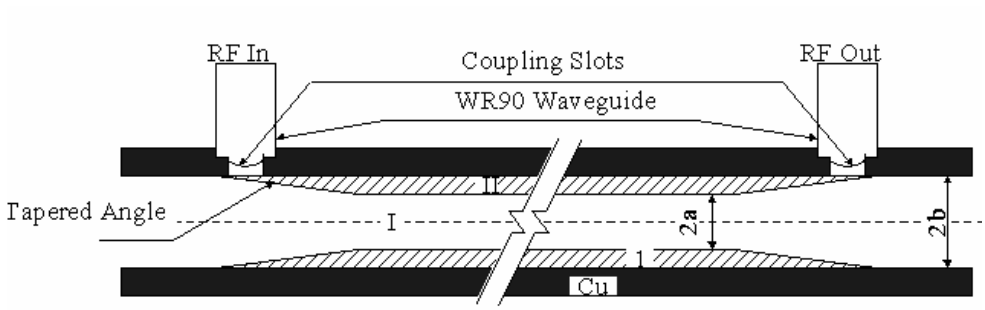

(b) Coupling slot around taper section.

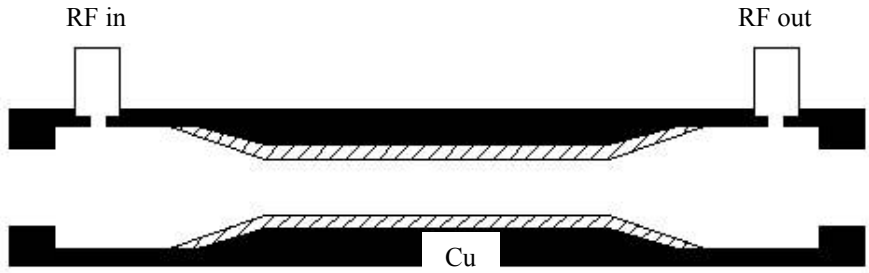

(c) Coupling slot apart from the taper section (modular design).

Figure 1.3. Couplers Developed at Argonne National Laboratory.

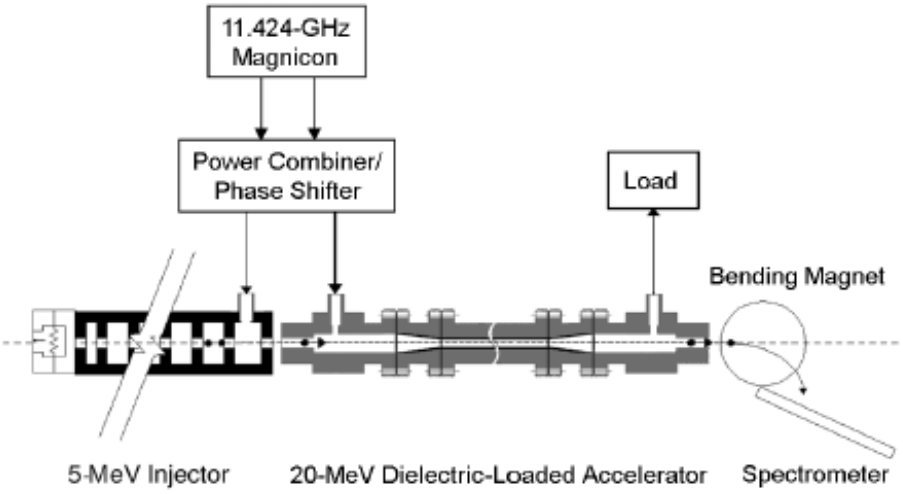

Figure 1.4. Schematic Drawing of NRL/ANL Compact Dielectric-Loaded Accelerator Test Facility.

Figure 1.4, consists of an X-band (11,424GHz) 5-MeV electron injector, an X-band dielectric-loaded accelerating structure, an X-band Magnicon which is used to power both the injector and DLA structure, and a magnetic dipole spectrometer to measure the beam energy. The Magnicon that was developed by NRL can produce 25 MW of output power in a 250ns pulse at 10Hz, and its final goal is to reach 50MW [41]. The two Magnicon output arms are combined to drive the injector and the DLA structure with a separate control of the power ratio and relative phase. The X-band injector, developed by Tsinghua University, China, consists of a thermal electron RF gun plus an X-band DAW (disk-and-washer) standing wave accelerating structure, which has very high coupling coefficient (~50%). The injector can provide >1pC electron bunch with emittance of 0.5mm mrad and energy spread of 2-3% [28].Currently, the Magnicon has been built and provides a good X-band RF source to test DLA structures with a variety of materials and configurations. In this thesis, all high power RF tests on the external DLA structure we developed were accomplished with the NRL Magnicon. The complete test facility is scheduled to be finished in the next two years, and will be a better platform for beam experiments of various DLA structures.

1.4 Organization of the Thesis

We start by introducing the related theories on dielectric-loaded accelerating structures in chapter 2. The leading part is the basic electromagnetic field analysis, where the general electromagnetic wave solution for the guided modes propagating in the circular dielectric-loaded waveguide will be obtained. This is followed by the discussion on a set of RF parameters which are used to characterize the performance of the

dielectric-loaded waveguide for use in particle acceleration. In the final section of this chapter, the wake fields calculation, a major concern in accelerating structure design, is presented.

As a major content of the thesis, we will describe the RF simulation, fabrication, bench measurement, and high power RF testing of the designed traveling wave dielectric-loaded accelerating structure in chapter 3. Specifically, the high power RF testing results will be discussed in detail. The DLA structures loaded with two different ceramic materials, Alumina and $Mg_xCa_{1-x}TiO_3$, have been tested. For the alumina tube, we concentrate on the study of the multipactor effect on the DLA structures under the high power RF field. For the $Mg_xCa_{1-x}TiO_3$, we mainly investigate the local field enhancement that caused dielectric joint breakdown of the DLA structures. In both cases, the physical models have been set up, and the corresponding engineering solutions are carried out.

In chapter 4, a new dielectric based accelerating structure design, multilayered DLA structure, will be presented. As seen from calculations based on analytical methods, this new structure shows a dramatic reduction of the RF power attenuation compared to the single layer DLA structure. Meanwhile, the shunt impedance is improved as well.

Chapter 6 is the conclusion of the thesis. Along with the summary of the research accomplished, the direction for the future study in the dielectric-loaded accelerating structures is outlined.

Two independent research projects, application of the resonant loop technique for the cavity beadpull experiment and direct wakefield measurement of the dielectric-loaded cavity on the beamline, are presented in the Appendices as well.

CHAPTER 2

THEORY OF DIELECTRIC-LOADED ACCELERATING STRUCTURES

2.1 Electromagnetic Characteristics

The proposed structure is shown in Figure 2.1. The analysis of the physics behind this partial dielectric loaded waveguide can be easily found in Zou's Ph.D. dissertation at Illinois Institute of Technology [42]. Here, we describe some important results and formulae that are frequently encountered.

It is well known that the general solution for the electric and magnetic field components in this partial dielectric-loaded circular waveguide can be derived from the wave equations with appropriate boundary conditions, which are shown in the following

$$E_z = \begin{cases} B_1 J_n(k_1 r)\cos(n\phi)e^{j(\omega t-\beta z)} & 0 \le r < a \\ B_2[J_n(k_2 r) - \dfrac{J_n(k_2 b)}{Y_n(k_2 b)} Y_n(k_2 r)]\cos(n\phi)e^{j(\omega t-\beta z)} & a \le r \le b \end{cases}$$

$$H_z = \begin{cases} A_1 J_n(k_1 r)\sin(n\phi)e^{j(\omega t-\beta z)} & 0 \le r < a \\ A_2[J_n(k_2 r) - \dfrac{J_n'(k_2 b)}{Y_n'(k_2 b)} Y_n(k_2 r)]\sin(n\phi)e^{j(\omega t-\beta z)} & a \le r \le b \end{cases} \tag{2.1a}$$

$$E_\phi = \begin{cases} \left[\dfrac{j\omega\mu_0}{k_1} A_1 J_n'(k_1 r) + \dfrac{j\beta n}{k_1^2 r} B_1 J_n(k_1 r)\right]\sin(n\phi)e^{j(\omega t-\beta z)} & 0 \le r < a \\ \left[\dfrac{j\omega\mu_0}{k_2} A_2 G_{nn}'(k_2 r) + \dfrac{j\beta n}{k_2^2 r} B_2 F_{nn}(k_2 r)\right]\sin(n\phi)e^{j(\omega t-\beta z)} & a < r \le b \end{cases}$$

$$E_r = \begin{cases} \left[-\dfrac{j\omega\mu_0 n}{k_1^2 r} A_1 J_n(k_1 r) - \dfrac{j\beta}{k_1} B_1 J_n'(k_1 r)\right]\cos(n\phi)e^{j(\omega t-\beta z)} & 0 \le r < a \\ \left[-\dfrac{j\omega\mu_0 n}{k_2^2 r} A_2 G_{nn}(k_2 r) - \dfrac{j\beta}{k_2} B_2 F_{nn}'(k_2 r)\right]\cos(n\phi)e^{j(\omega t-\beta z)} & a < r \le b \end{cases} \tag{2.1b}$$

$$H_\phi = \begin{cases} \left[-\dfrac{j\omega\varepsilon_0}{k_1} B_1 J_n{}'(k_1 r) - \dfrac{j\beta n}{k_1{}^2 r} A_1 J_n(k_1 r) \right] \cos(n\phi) e^{j(\omega t - \beta z)} & 0 \le r < a \\ \left[-\dfrac{j\omega\varepsilon_r\varepsilon_0}{k_2} B_2 F_{nn}{}'(k_2 r) - \dfrac{j\beta n}{k_2{}^2 r} A_2 G_{nn}(k_2 r) \right] \cos(n\phi) e^{j(\omega t - \beta z)} & a < r \le b \end{cases}$$

$$H_r = \begin{cases} \left[-\dfrac{j\omega\varepsilon_0 n}{k_1{}^2 r} B_1 J_n(k_1 r) - \dfrac{j\beta}{k_1} A_1 J_n{}'(k_1 r) \right] \sin(n\phi) e^{j(\omega t - \beta z)} & 0 \le r < a \\ \left[-\dfrac{j\omega\varepsilon_r\varepsilon_0 n}{k_2{}^2 r} B_2 F_{nn}(k_2 r) - \dfrac{j\beta}{k_2} A_2 G_{nn}{}'(k_2 r) \right] \sin(n\phi) e^{j(\omega t - \beta z)} & a < r \le b \end{cases} \tag{2.1c}$$

where B1, B2, A1 and A2 are the field amplitudes in the region I (vacuum) and II (dielectric) respectively, v_p is the phase velocity of the wave traveling inside the tube, and c is the speed of light in free space. k_1, k_2 are the cutoff wave number in the each region, and β is the wave propagation constant. They are defined as

$$\begin{aligned} k_1 &= \omega \sqrt{\frac{1}{c^2} - \frac{1}{v_p{}^2}} \\ k_2 &= \omega \sqrt{\frac{\varepsilon_r}{c^2} - \frac{1}{v_p{}^2}} \\ \beta^2 &= k_0{}^2 - k_1{}^2 = \varepsilon_r k_0{}^2 - k_2{}^2 \\ k_0{}^2 &= \omega^2 \mu_0 \varepsilon_0 \end{aligned} \tag{2.2}$$

$$\begin{aligned} F_{nn}(k_2 r) &= J_n(k_2 r) - \frac{J_n(k_2 b)}{Y_n(k_2 b)} Y_n(k_2 r) \\ G_{nn}(k_2 r) &= J_n(k_2 r) - \frac{J_n{}'(k_2 b)}{Y_n{}'(k_2 b)} Y_n(k_2 r) \\ F_{nn}{}'(k_2 r) &= J_n{}'(k_2 r) - \frac{J_n(k_2 b)}{Y_n(k_2 b)} Y_n{}'(k_2 r) \\ G_{nn}{}'(k_2 r) &= J_n{}'(k_2 r) - \frac{J_n{}'(k_2 b)}{Y_n{}'(k_2 b)} Y_n{}'(k_2 r) \end{aligned} \quad . \tag{2.3}$$

Using the boundary conditions at $r=a$ (E_z, E_ϕ, H_ϕ, and H_z continuous), the dispersion relation of guided wave traveling in this waveguide can be obtained as

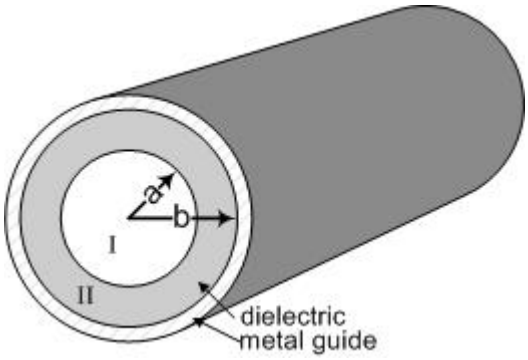

*Note: Region I is vacuum; region II is dielectric area; and the outmost layer is metal.

Figure 2.1. Partially Dielectric-Loaded Circular Waveguide for Particle Acceleration. The Dielectric Tube has Inner Radius a and Outer Radius b.

$$\left[\frac{\mu_0}{k_1 a}\frac{J_n{}'(k_1 a)}{J_n(k_1 a)}-\frac{\mu_0}{k_2 a}\frac{G_{nn}{}'(k_2 a)}{G_{nn}(k_2 a)}\right]\left[\frac{\varepsilon_0}{k_1 a}\frac{J_n{}'(k_1 a)}{J_n(k_1 a)}-\frac{\varepsilon_r\varepsilon_0}{k_2 a}\frac{F_{nn}{}'(k_2 a)}{F_{nn}(k_2 a)}\right]$$
$$=\frac{(\beta n\omega)^2}{(k_1 k_2 a)^4}(\mu_0\varepsilon_r\varepsilon_0-\mu_0\varepsilon_0)^2 \quad . \qquad (2.4)$$

In the application of particle acceleration, the dominant mode TM01 mode is of main interest. It is expected to have a phase velocity v_p=c, thus the velocity of charge particle can be synchronized with the propagation of RF wave that provides the accelerating electric field. For the TM_{01} mode, the electric and magnetic field components can be simplified as

$$E_z=\begin{cases} B_1 J_0(k_1 r)e^{j(\omega t-\beta z)} & 0\le r<a \\ B_2\left[J_0(k_2 r)-\dfrac{J_0(k_2 b)}{Y_0(k_2 b)}Y_0(k_2 r)\right]e^{j(\omega t-\beta z)} & a\le r\le b \end{cases}$$
$$E_r=\begin{cases} -\dfrac{j\beta}{k_1}B_1 J_0{}'(k_1 r)e^{j(\omega t-\beta z)} & 0\le r<a \\ -\dfrac{j\beta}{k_2}B_2 F_{00}{}'(k_2 r)e^{j(\omega t-\beta z)} & a<r\le b \end{cases}$$
$$H_\phi=\begin{cases} -\dfrac{j\omega\varepsilon_0}{k_1}B_1 J_0{}'(k_1 r)e^{j(\omega t-\beta z)} & 0\le r<a \\ -\dfrac{j\omega\varepsilon_r\varepsilon_0}{k_2}B_2 F_{00}{}'(k_2 r)e^{j(\omega t-\beta z)} & a<r\le b \end{cases} \quad . \qquad (2.5)$$

The electric fields in the vacuum region described by Equation (2.5) have very interesting characteristics. When the phase velocity of the wave is c, the transverse wave constant in vacuum region k_1=0 from Equation (2.2), which leads that E_z is constant in this region from Equation (2.5). This implies that there are no focusing and de-focusing forces for a relativistic particle traveling inside the vacuum chamber from Panofsky-Wenzel theorem [43]. This is critical for emittance preservation in linear accelerators, particularly for high brightness electron gun development. Figure 2.2 shows this characteristic of the longitudinal electric field.

Besides field components, the dispersion relation of the TM_{01} mode has been simplified from Equation (2.4) to be

$$\left[\frac{1}{k_1}\frac{J_0'(k_1a)}{J_0(k_1a)}-\frac{\varepsilon_r}{k_2}\frac{F_{00}'(k_2a)}{F_{00}(k_2a)}\right]=0 \quad . \tag{2.6}$$

From the Equation (2.2) we know the phase velocity of the guided wave in this waveguide can be slowed down below the speed of light due to the loaded ceramics with high dielectric constant. Meanwhile, the inner radius a is chosen based on the requirements of beam dynamics. Thus, governed by the mode dispersion relation (Equation (2.6)), the outer radius b should be adjusted accordingly to achieve the desired v_p.

The deflecting modes (hybrid modes) in dielectric-lined circular waveguides are the HEM_{nm} modes. The lowest deflecting mode is the HEM_{11} mode, and it is the most harmful mode for acceleration due to its transverse force to the charged particles [44, 45]. If the transverse electric force is too strong, the deflecting mode can cause beam break-up [46].

Figure 2.3 shows the dispersion curves of the propagation constant β, versus frequency for TM_{01} and HEM_{11} modes in a dielectric-lined circular waveguide with a=2.96 mm, b=4.53 mm, and ε_r=20. When β=0, the corresponding frequency is the cutoff frequency of such mode. The intersections of these two dispersion curves with the speed of light line indicate that the propagation constant of HEM_{11} mode is less than that of TM_{01} mode, at the location where these two modes have the same phase velocity as the speed of light c. Thus the amplitude of the transverse wake fields caused by particle beams passing through such dielectric-lined waveguide is smaller than that of the

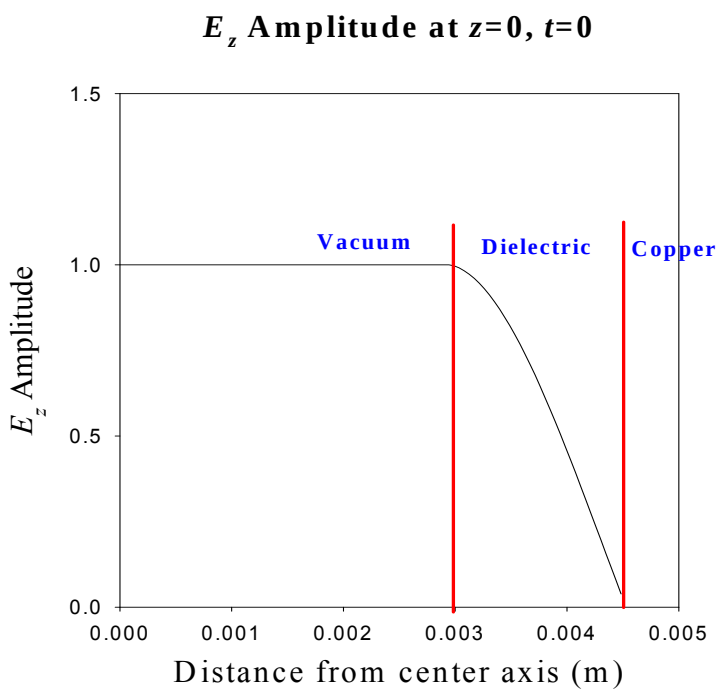

*Note: The geometry of the waveguide shown in Figure 2.1 with a=3 mm, ε_r=20, and b=4.57 mm. The phase velocity of the TM_{01} wave is equal to c.

Figure 2.2. The Amplitude of E_z of the TM_{01} Mode along the Transverse Radius of the Dielectric-lined Circular Waveguide.

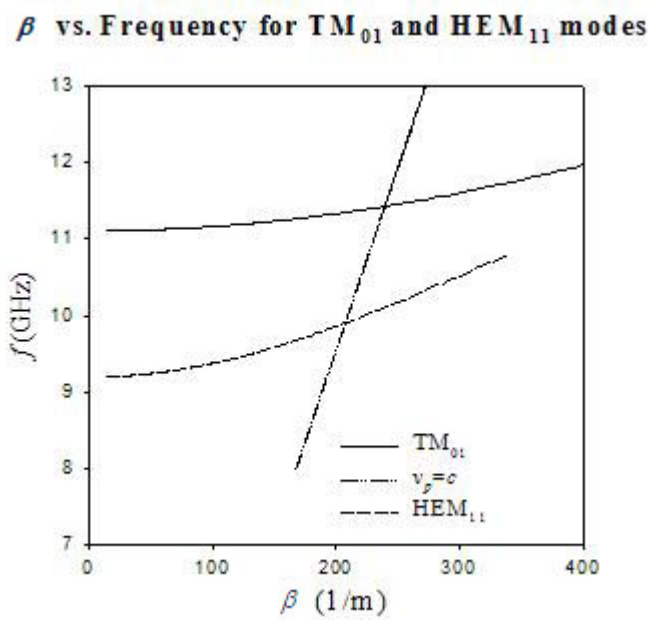

*Note: The geometry of the waveguide shown in Figure 2.1 with a=3 mm, ε_r=20, and b=4.57 mm.

Figure 2.3. The Propagation Constants of the TM_{01} Mode and the HEM_{11} Mode versus Frequency in the Dielectric-lined Circular Waveguide.

longitudinal wakefield [45], because all the wakefield modes have the same phase velocity. This is very important for preventing Beam Break UP (BBU), and it is one advantage of using dielectric-lined circular waveguides as accelerators. The detailed discussion of the characteristics of both TM_{01} and HEM_{11} modes, and their geometric dependence as well, are presented in [42].

2.2 Accelerating Parameters

To discuss and further compare the different accelerating structures quantitatively, it is helpful to introduce some commonly used accelerator properties related parameters. In this section, we will calculate some standard accelerator figures of merit and compare the multilayered DLA structure to the single-layered DLA structure to show the advantages of the former.

We begin by recalling some of the basic figures of merit for a traveling wave structure. The parameters are: the group velocity v_g, the shunt impedance per unit length r, the attenuation constant per unit length α_0, and the ratio of the shunt impedance per unit length to the quality factor (r/Q) and are defined [47] as,

$$\begin{cases} v_g = \dfrac{d\omega}{d\beta} = \dfrac{P}{U} & (2.7a) \\ \dfrac{r}{Q} = \dfrac{E_a^{\,2}}{\omega U} & (2.7b) \\ r = \dfrac{E_a^{\,2}}{-dP/dz} & (2.7c) \\ \alpha_0 = \dfrac{\omega}{2Qv_g} & (2.7d) \end{cases}$$

where, P and U represent the TW power (energy flow) in the structure and the time-averaged stored energy per unit length in the structure respectively;

$$\begin{cases} P = \frac{1}{2}\oint_S \vec{E} \times \vec{H}^* \cdot d\vec{s} & (2.8a) \\ U = \frac{\varepsilon}{4}\mathrm{Re}\left(\int_V \vec{E} \times \vec{E}^* dv\right) + \frac{\mu}{4}\mathrm{Re}\left(\int_V \vec{H} \times \vec{H}^* dv\right) & (2.8b) \end{cases}$$

and v_g is group velocity; E_a is acceleration gradient. Q is quality factor which is defined in terms of the time average power loss P_{loss} per unit length for the traveling wave DLA structure as

$$Q = \frac{\omega U}{P_{loss}} \tag{2.9}$$

where

$$P_{loss} = \frac{R_s}{2}\int_S \left|H_\perp\right|^2_{r=b} ds + \frac{1}{2}\int_{\substack{Dielectric \\ UnitLength}} \omega\varepsilon_r\varepsilon_0 \tan\delta_l E^2 dV \tag{2.10}$$

S is the surface area of the wall of unit length, R_s is the surface resistance of copper per unit length, $H_\perp(r=b)$ is the transverse magnetic field on the wall, and $\tan\delta_l$ is the loss tangent of the dielectric material. The surface resistivity R_s is defined as

$$R_s = \sqrt{\frac{\mu_0\omega}{2\sigma}} \tag{2.11}$$

where σ is the conductivity of copper. In Equation (2.10), $\omega\varepsilon_r\varepsilon_0 \tan\delta_l$ is an equivalent conductance of the dielectric, thus the second part of such equation is the average power dissipation in the dielectric material per period per unit length. For high frequency band structures, the power dissipation in the wall is much more than that in the dielectric, because of the largely increased skin effect.

The shunt impedance per unit length, r, is a measure of the effectiveness in producing an axial accelerating field amplitude, Ea, for a given power dissipated per unit length $-dP_{loss}/dz$, (which is equal to -dP/dz). In particular, for a constant impedance TW

accelerator, r is related to particle energy gain ΔW within an accelerating distance L and can be expressed as [47]

$$\Delta W = q\sqrt{rP_0 L}\frac{1-e^{-\alpha_0 L}}{\sqrt{\alpha_0 L}}\cos\varphi, \tag{2.12}$$

where P_0 is the incident RF power, and φ is the particle phase relative to the crest of the RF wave.

Another useful figure of merit is the so-called r over Q (r/Q) which measures the efficiency of acceleration, E_a, per unit stored energy, U, at a given frequency, ω. Combining Equation (2.7a) and Equation (2.7b) we get,

$$E_a^{\ 2} = P\frac{r}{Q}\frac{\omega}{v_g}, \tag{2.13}$$

which shows that for a given incident power the accelerating gradient, E_a, is proportional to r/Q and inversely proportional to the group velocity, v_g. This means that even when a structure has a high r/Q, it may not be an efficient accelerator if v_g is also high. Aside from using r/Q to characterize the accelerating efficiency of a constant impedance TW accelerator, once we know r/Q of each mode [18,19], it also reveals the amplitude of the wakefields generated by charged particles traveling through the structure without having to solve the inhomogeneous Maxwell's equations. For this application of r/Q, one will see details in the next section when we discuss how to calculate wakefields in a DLA structure. Finally, in Equation (2.7d), α_0, is defined as field attenuation per unit length, which satisfies

$$P(z) = P_0 e^{-2\alpha_0 z}. \tag{2.14}$$

where, P is traveling wave power (energy flow) and z is the direction of propagation.

Based on the above definitions, we see that all of the acceleration parameters are related to one another. For example, according to Equation (2.13), for a given incident RF power, P_0, a high accelerating gradient, E_a, is obtained when r/Q is large and v_g is small. However, according to Equation (2.7d), we prefer v_g to be high to keep the *RF* power attenuation, α_0, small and thus reduce the drop in the accelerating gradient along the structure length. For a constant-impedance, TW structure, the maximally efficient particle acceleration may be evaluated with Equation (2.12), in which the shunt impedance dominates particle energy gain after the structure length is optimized [47].

The detailed investigation of the relation between the geometric and accelerating parameters is given by P. Zou [42]. Table 2.1 shows the designed parameters for two typical X-band circular traveling wave dielectric-loaded accelerating structures. The used ceramic materials are compound of Mg-Ti oxide (dielectric constant of 20) and Alumina oxide (dielectric constant of 9.4) respectively. Both materials have very low loss tangent so that they have not been taken into account when calculating the parameters Q and power attenuation in the Table 2.1. In addition, one should keep in mind that all the RF parameters is based on the accelerating mode, here TM_{01} mode at synchronous condition ((phase velocity equal to particle velocity, typically close to the speed of light, *c*) for circular DLA structure.

2.3 Wakefields Calculation

The concept of wakefields is very important for the accelerator design because it is the major reason to cause beam instabilities such as bunch lengthening, head-tail turbulence and emittance growth. However, the wakefields energy generated by a

Table 2.1. Geometric and Physical Properties of the 11.424GHz DLA Structures

PARAMETERS	Alumina based DLA structure	MgCaTi based DLA structure
Material	Alumina	$Mg_xCa_{1-x}TiO_3$
Inner Radius	5mm	3mm
Outer Radius	7.185mm	4.567mm
Dielectric Constant	9.4	20
Group Velocity	0.134c	0.057c
R/Q	6.9kΩ/m	8.8kΩ/m
Shunt Impedance	30.3 MΩ/m *	25.1 MΩ/m*
Q	4378*	2865*
Power ATTN	1.8dB/m*	6.6dB/m*
RF power needed to support 1MV/m gradient	80kW	27kW

* Loss tangent of the dielectrics are not included in the calculations.

traveling beam can also be used to accelerate the particles behind after a certain proper time slot arrangement. Dielectric-loaded structure has been demonstrated to be a good candidate for the application of wakefield acceleration at Argonne Wakefield Accelerator facility since late 1980s [23]. In this section, we briefly introduce two methods to calculate wakefields in the dielectric-lined waveguide. One is to directly find solutions from Maxwell's equations; the other is an indirect way by using the accelerating parameter of the structure, *r*/Q.

Direct Computational Methods. Normally, the wakefields calculation is tedious and cumbersome. The complete solution calls for solving the inhomogeneous wave propagation equations. For the wakefields in circular dielectric-loaded accelerating structure, a clear derivation and certain results can be found in [44] and [45].

First we will consider the electromagnetic field radiated by a particle with charge e moving at velocity v along a line parallel to the axis of the tube at distance r_0 as shown in Figure 2.4. Because of the presence of the dielectric material, the Cherenkov radiation conditions will be satisfied when the particle velocity $\beta = v/c > \varepsilon^{-0.5}$ and the particle will generate wake fields behind it. The wakefields produced by the motion of a charged particle are given by Maxwell's equations:

$$\nabla \times \vec{E} = -\frac{\partial \vec{B}}{\partial t}, \quad \nabla \cdot \vec{B} = 0$$
$$\nabla \cdot \vec{D} = \rho, \quad \nabla \times \vec{H} = \frac{\partial \vec{D}}{\partial t} + \vec{j} \quad . \tag{2.15}$$

As a standard way of solving electrodynamics problems we introduced a scalar and a vector potential ϕ and $\vec{A}$, and under the Lorentz gauge they satisfy uncoupled inhomogeneous wave equations respectively as

$$\nabla^2\phi + \omega^2\mu\varepsilon\frac{\partial^2\phi}{\partial t^2} = -\frac{\rho}{\varepsilon}, \quad \nabla^2\vec{A} + \omega^2\mu\varepsilon\frac{\partial^2\vec{A}}{\partial t^2} = -\mu\vec{j} \quad . \tag{2.16}$$

For a charged particle moving at the velocity v in the cylindrical coordinates z direction, the charge and current density are

$$\rho = \frac{e\delta(r-r_0)}{r}\delta(\theta)\delta(z-vt), \quad \vec{j} = \vec{v}\rho \quad . \tag{2.17}$$

Then we solve for the scalar and vector potentials and bring them into equation

$$\vec{E} = -\nabla\phi - \frac{\partial\vec{A}}{\partial t}, \quad \vec{H} = \frac{1}{\mu}\nabla\times\vec{A} \quad , \tag{2.18}$$

so that we can obtain electric and magnetic field components. We will omit the details here and only give the expression of longitudinal components. The detail derivation can be found in [45].

For a given nth mode (n=0 is monopole, n=1 dipole, n=2 quadrupole), the longitudinal EM fields are

$$E_z^n(r,\theta,z) = -8e\cos(n\theta)\cos(\frac{k_0}{\beta}(z-vt))\cdot I_n(k_1r)I_n(k_1r_0)\cdot\frac{K_n(k_1a)}{I_n(k_1a)}\frac{T(k_2)}{k_2\, dC(k_2)/dk_2}\Bigg|_{k_2=k_{2\lambda}} \tag{2.19}$$

$$H_z^n(r,\theta,z) = -8e\sin(n\theta)\sin(\frac{k_0}{\beta}(z-vt))\cdot I_n(k_1r)I_n(k_1r_0)\cdot\frac{K_n(k_1a)}{I_n(k_1a)}\frac{T(k_2)}{k_2\, dC(k_2)/dk_2}\Bigg|_{k_2=k_{2\lambda}} \tag{2.20}$$

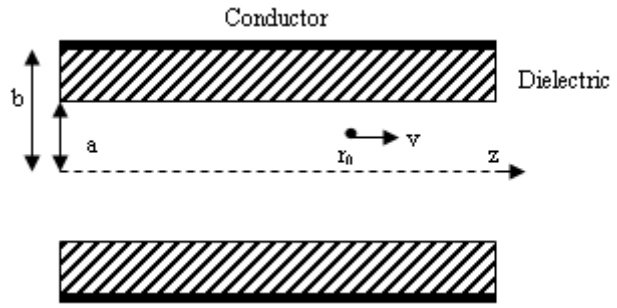

Figure 2.4. Schematic Dielectric-Loaded Wakefields Structure.

where

$$T(k_2)=k_2^2k_1^2\left[\frac{k_1G_{nn}{}'(k_2a)}{G_{nn}(k_2a)}+\frac{k_2I_n{}'(k_1a)}{I_n(k_1a)}\right]\cdot\left[\frac{k_2I_n{}'(k_1a)}{I_n(k_1a)}+\frac{\varepsilon k_1F_{nn}{}'(k_2a)}{F_{nn}(k_2a)}\right]-\frac{n^2}{a^2}k_1^4\beta^2\left(\frac{\varepsilon-1}{1-\beta^2}\right)^2 \quad (2.21)$$

$$C(k_2)=\frac{n^2k_2}{a^2}k_1^2\beta^2\left(\frac{\varepsilon-1}{1-\beta^2}\right)^2-k_2^3\left[\frac{k_1G_{nn}{}'(k_2a)}{G_{nn}(k_2a)}+\frac{k_2I_n{}'(k_1a)}{I_n(k_1a)}\right]\cdot\left[\frac{k_2I_n{}'(k_1a)}{I_n(k_1a)}+\frac{\varepsilon k_1F_{nn}{}'(k_2a)}{F_{nn}(k_2a)}\right] \quad (2.22)$$

and

$$\begin{aligned} k_1{}^2 &= \frac{\omega^2}{v^2}(1-\beta^2) \\ k_2{}^2 &= \frac{\omega^2}{v^2}(\varepsilon\beta^2-1) \\ k_0 &= \frac{\omega}{c} \end{aligned} \quad (2.23)$$

J_n and Y_n are nth-order Bessel functions of the first and second kinds respectively. I_n and K_n are nth-order modified Bessel functions of the first and second kinds. F_{nn}, F'_{nn}, G_{nn} and G'_{nn} are defined in equation (2.3). θ is azimuthal angle of the structure. β is relativistic parameter, and $k_{2\lambda}$ are zeros of C(s).

When particle moving at center of circular waveguide ultrarelativisticly, that is, r_0 is zero, n=0 and β=1, then Equation (2.19) and Equation (2.20) can be simplified as

$$E_z(r,z_0)=\frac{4e}{\varepsilon a}\sum_{\lambda}\left(\frac{F_{00}(k_2a)Y_0(k_2b)}{\frac{d}{dk_2}\left(F_{00}{}'(k_2a)Y_0(k_2b)-\frac{k_2a}{2\varepsilon}F_{00}(k_2a)Y_0(k_2b)\right)}\right)_{k_2=k_{2\lambda}}\cos(\frac{\omega_\lambda}{c}z_0) \quad (2.24)$$

$$H_z(r,z_0)=0 \quad (2.25)$$

where $k_{2\lambda}$ satisfies the condition

$F_{00}{}'(k_2a)-\frac{k_2a}{2\varepsilon}F_{00}(k_2a)=0$. $z_0=z-vt$ is the distance behind the charge.

These monopole modes are equivalent to TM_{0n} modes in guided wave decomposition in which dominant TM_{01} mode contribute significantly to the total excited energy. As in all the wakefield calculations, if the particles traverse at an offset of the axial, the dipole or other high order wakefield modes will be excited, which make the particle behind experiencing transverse forces. The transverse forces can be directly calculated from the longitudinal field E_z by using Panofsky-Wenzel theorem [43]

$$\frac{\partial \vec{F}_{\perp}}{\partial z} = e\nabla_{\perp} E_z \tag{2.26}$$

which gives

$$F_r = e\left(E_r - \beta B_\theta\right) = e\int \frac{\partial E_z}{\partial r} dz$$

$$F_\theta = e\left(E_\theta + \beta B_r\right) = e\int \frac{\partial E_z}{r\partial \theta} dz\,. \tag{2.27}$$

For the circular DLA structure, there will be no transverse focusing force from the on-axial particles due to no r dependence of E_z in Equation (2.25). That means that the transverse beam profile will not be influenced by the wakefields in the monopole modes.

In general, with assumption of a Gaussian line charge with rms bunch length σ, the wakefields can be expressed as the integration

$$E_z^m(r,\theta,z_0) = \frac{N}{\sigma\sqrt{2\pi}} \int_{-\infty}^{z_0} E_z^m(r,\theta,z) e^{-[(z_0-z)/\sigma]^2} dz\,. \tag{2.28}$$

Here N is the total number of charges in the driving bunch and z_0 is the distance behind the center of the driving bunch where the field is measured.

Figure 2.5 is an example of the longitudinal wakefield generated by the charged particles traveling on the axial of the circular DLA structure. The electron bunch is 100nC total charge with rms bunch length of 1mm. The loaded dielectric tube has inner

radius 2mm, outer radius 5mm and dielectric constant 3. The figure shows that the peak wakefield gradient on the axial is around 240MeV/m.

Indirect Computational Method. Rather than solving the bunch-excited fields through Maxwell's equations directly, the wakefields can be expressed as a sum over waveguide parameter *r*/Q, or equivalent of loss factor in most literatures (a function of the structure geometry only) for each mode [48,49]. The summation is an infinite series and it can be truncated by the finite bunch length of the drive beam, as in case of most wakefields calculations. Equation (2.29) shows the relation of the longitudinal wakefields amplitude excited by a point charged particle and the *r* over Q for each guided wave mode at the accelerating waveguide:

$$E_{0i} = 2k_{l\,i}q = \frac{q\omega_i}{2}\left(\frac{r}{Q}\right)_{(x_0,y_0)_i}, \tag{2.29}$$

where, the subscript *i* indicates the ith mode; E_0 is the amplitude of longitudinal wakefields, k_l is a normalized loss factor, $(r/Q)_{(x0,y0)}$ is calculated while charged particles traveling at a certain position (x_0, y_0) for each mode, and q is the charge. The mode selection for the longitudinal wakefields calculation is based on the relation between the system response and signal excitation. The accelerating structure (waveguide) can be considered to be a passive system, and the traveling electron bunch is equivalent to be a point particle with $j_z = ev\delta(z - vt)\delta(x - x_0)\delta(y - y_0)$, in Cartesian coordinate and z is chosen to be beam launching direction. Then, the guided wave modes in the waveguide system selected to compute wakefields are under the criterion of the electromagnetic fields' patterns matching, i.e. mode matching between the excited wakefields mode

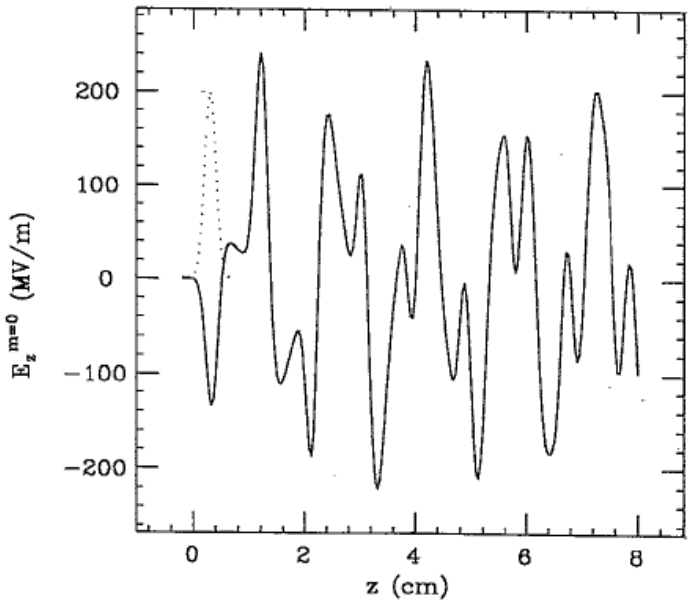

* Note: The dotted line is the longitudinal distribution of the driving beam.

Figure 2.5. The Longitudinal Wakefield for the Monopole Mode (Beam Traverses on the Axial of the Circular DLA Structure).

(classified by the leading-order azimuthal harmonic) and the guided wave modes (waveguide intrinsic modes) that let them have similar field's space distributions. The transverse wakefields are also obtained from Panofsky-Wenzel theorem.

Now, we briefly introduce this indirect computational method to calculate the wakefields of a dielectric-loaded rectangular waveguide accelerating structure, another widely investigated DLA structure. Reference [50] and [51] showed the detailed process for computing the longitudinal (monopole modes) and transverse (dipole modes) components respectively. For comparison, one can make a comparison by referring to Reference [23], which provides the direct computational method to solve wakefields in rectangular DLA structure.

The geometry of the rectangular DLA structure to be analyzed is shown in Figure 2.6. Before calculating the wakefield, we need to find the EM solution of all guided modes (intrinsic modes) of this waveguide. The normal modes propagating in rectangular DLA structures are no longer pure TE or TM mode but either LSM (longitudinal section magnetic) or LSE (longitudinal section electric) modes that, respectively, have no ***H*** or ***E*** components normal to the air-dielectric interface.

The field components of the LSM and LSE modes in a dielectric-loaded rectangular waveguide can be derived from the solution of vector potential wave equations: LSM mode:

$$\vec{\psi}_e = \vec{\alpha}_y \psi_e(x, y, z)$$

$$\begin{cases} E_x = -j\dfrac{1}{\omega\mu\varepsilon}\dfrac{\partial^2\psi_e}{\partial x\partial y} & H_x = -\dfrac{1}{\mu}\dfrac{\partial\psi_e}{\partial z} \\ E_y = -j\dfrac{1}{\omega\mu\varepsilon}(\dfrac{\partial^2}{\partial y^2} + \beta^2)\psi_e & H_y = 0 \\ E_z = -j\dfrac{1}{\omega\mu\varepsilon}\dfrac{\partial^2\psi_e}{\partial y\partial z} & H_z = \dfrac{1}{\mu}\dfrac{\partial\psi_e}{\partial x} \end{cases} \tag{2.30a}$$

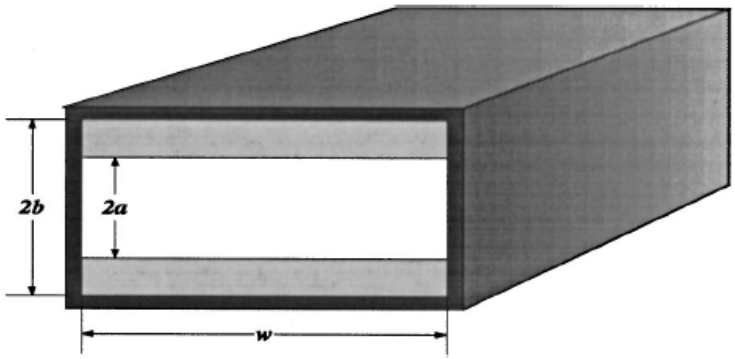

Figure 2.6. Dielectric-Loaded Rectangular Waveguide.

LSE mode: $\vec{\psi}_h = \vec{\alpha}_y \psi_h(x, y, z)$

$$\begin{cases} E_x = \dfrac{1}{\varepsilon}\dfrac{\partial \psi_h}{\partial z} & H_x = -j\dfrac{1}{\omega\mu\varepsilon}\dfrac{\partial^2 \psi_h}{\partial x \partial y} \\ E_y = 0 & H_y = -j\dfrac{1}{\omega\mu\varepsilon}(\dfrac{\partial^2}{\partial y^2} + \beta^2)\psi_h \\ E_z = -\dfrac{1}{\varepsilon}\dfrac{\partial \psi_h}{\partial x} & H_z = -j\dfrac{1}{\omega\mu\varepsilon}\dfrac{\partial^2 \psi_h}{\partial y \partial z} \end{cases}, \tag{2.30b}$$

where ψ_e and ψ_h must satisfy the scalar wave equations:

$$\nabla^2 \psi_q(x, y, z) + \beta^2 \psi_q(x, y, z) = 0 \qquad q = e, h\,. \tag{2.30c}$$

Applying the boundary conditions, the potential functions are obtained, shown in Equation (2.31) and Equation (2.32)

$$\psi_{emn} = \begin{cases} A_{mn} \sin \dfrac{m\pi}{w}(x + \dfrac{w}{2}) \sin k_{ymn}^{(0)} y \cdot e^{-j\beta_{mn} z}, & 0 < y < a \\ B_{mn} \sin \dfrac{m\pi}{w}(x + \dfrac{w}{2}) \cos k_{ymn}^{(1)} (b - y) \cdot e^{-j\beta_{mn} z}, & a < y < b \end{cases} \tag{2.31}$$

$$\psi_{hmn} = \begin{cases} C_{mn} \dfrac{1}{j\omega\mu_0} \cos \dfrac{m\pi}{w}(x + \dfrac{w}{2}) \sin k_{ymn}^{(0)} y \cdot e^{-j\beta_{mn} z}, & 0 < y < a \\ D_{mn} \dfrac{1}{j\omega\mu_0} \cos \dfrac{m\pi}{w}(x + \dfrac{w}{2}) \sin k_{ymn}^{(1)} (b - y) \cdot e^{-j\beta_{mn} z}, & a < y < b \end{cases} \tag{2.32}$$

where $\dfrac{A_{mn}}{B_{mn}} = \dfrac{\varepsilon_r \cos k_{ymn}^{(1)} (b - a)}{\sin k_{ymn}^{(0)} a}$, and $\dfrac{C_{mn}}{D_{mn}} = \dfrac{\sin k_{ymn}^{(1)}(b-a)}{\sin k_{ymn}^{(0)} a}$, and the transverse propagation constants are expressed in terms of the longitudinal propagation constant β_{mn} using the following conditions:

$$k_{ymn}^{(0)\,2} = k_0^2 - (\frac{m\pi}{w})^2 - \beta_{mn}^2 \tag{2.33a}$$

$$k_{ymn}^{(1)\,2} = \varepsilon_r k_0^2 - (\frac{m\pi}{w})^2 - \beta_{mn}^2 \quad . \tag{2.33b}$$

The $k_0 = 2\pi f/c$ is the propagation constant in free space and the superscript (0) or (1) refers to the vacuum or dielectric region of the waveguide respectively.

The second step to calculate wakefields is the mode matching. When a short electron bunch traveling through dielectric-loaded rectangular waveguide along the center, it will generate only monopole modes; but if it traveling at a transverse offset (x_0, y_0) both x- and y-dipole modes will be excited. Based on the field distribution pattern, we choose monopole mode to be superposition of LSM_{mn} and LSE_{mn} (m=1,3,5…; n=1,2,3…); the x-dipole mode can be expressed as a superposition of $LSM_{mn}^{(open)}$ and $LSE_{mn}^{(open)}$ (m=2,4,6…) modes and y-dipole as $LSM_{mn}^{(short)}$ and $LSE_{mn}^{(short)}$ (m=1,3,5…) modes. Here, the superscript (short) or (open) designates to assumed short ($E_{||} = 0$) or open symmetric boundary conditions at the midplane of the rectangular waveguide. The detailed description of mode matching for the dipole modes can be found in [51].

Then we can calculate the geometric dependent parameter *r*/Q for each intrinsic mode through computing the stored energy U per unit length and accelerating electrical field E_z

$$\left[\frac{r_{x_0,y_0}}{Q}\right]_i = \left[\frac{\left|E_z\right|_{x_0,y_0}^{2}}{\omega U}\right]_i \tag{2.34}$$

where (x_0, y_0) is the particle trajectory position along the structure.

Eventually, the amplitude of the longitudinal wakefields is easily obtained from Equation (2.29), and its space related field distribution is the same as the matched intrinsic modes. For example, the longitudinal wakefield of the monopole mode in the rectangular DLA structure is

$$E_z = \sum_i E_{0i} \sin\left(\frac{\pi}{w}\left(x + \frac{w}{2}\right)\right)\cos\left(k_{yi}^{0} y\right)e^{-j\beta z}. \tag{2.35}$$

One should notice that, unlike the circular DLA structure, the longitudinal wakefield of the monopole mode in the rectangular structure is dependent on the coordinate x and y. Therefore, it has a transverse focusing force in both x and y directions.

Figure 2.7 shows an example of the longitudinal wakefields in a rectangular DLA structure obtained using the indirect computational method introduced above. The particle bunch used in this example is 1 nC with bunch length 2mm and moving along the center.

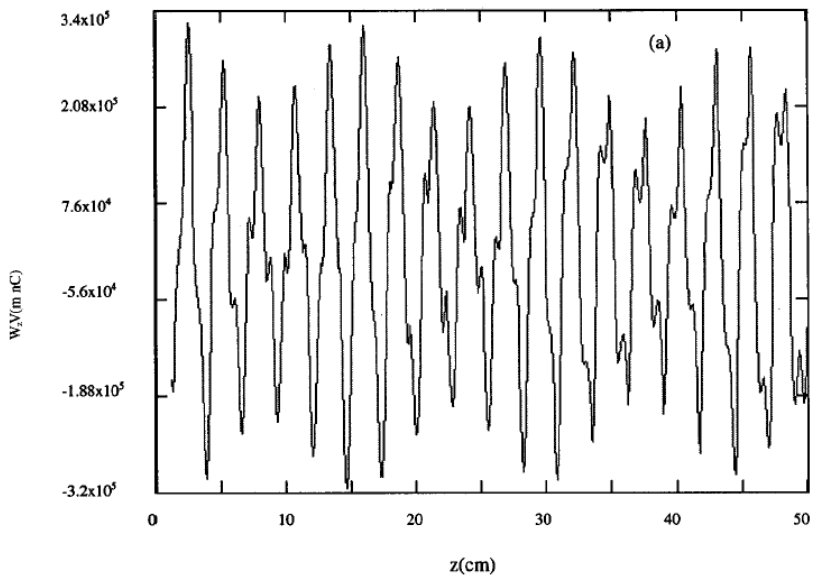

*Note: The geometric dimensions are a=3mm, b=5mm, w=23mm, ε_r=10 referred to Figure (2.5).

Figure 2.7. Calculated Longitudinal Wakefield in an X-Band Rectangular DLA Structure Using the Indirect Computational Method.

CHAPTER 3

TESTING ON X-BAND DIELECTRIC-LOADED ACCELERATING STRUCUTRES

Unlike our previous designs [7], we adopt a new modular concept to design our accelerating structure. Figure 3.1 shows the schematic drawing of our design that consists of three functional modules, (1) RF couplers that convert between the TE_{10} mode in the rectangular waveguide and the TM_{01} mode in the circular copper waveguide at the input and output ends. (2) Tapered dielectric matching sections to match the impedance of the TM wave between the coupler and the acceleration section. (3) The partially loaded dielectric accelerating section is used to accelerate particles. This design overcame the arcing problem that has been observed in the RF coupler of a previous DLA structure by separating the coupling and accelerating sections [39]. The coupler is implemented on a section of regular circular waveguide so that the aperture of the coupling slot is much bigger than in the old scheme and this makes the peak value of EM field much smaller than that of the old scheme under the same power input. And because of its broadband design, the coupler can be reused to test various dielectric based X-band DLA structures that lead dramatic reduction of the experimental period. So far, we have fabricated and tested two different ceramic based modular DLA structures, Alumina (with dielectric constant of 9.4) and $Mg_xCa_{1-x}TiO_3$ (with dielectric constant of 20). Their geometric and accelerating parameters are shown in Table 2.1. In this section, both structures are included in our discussion.

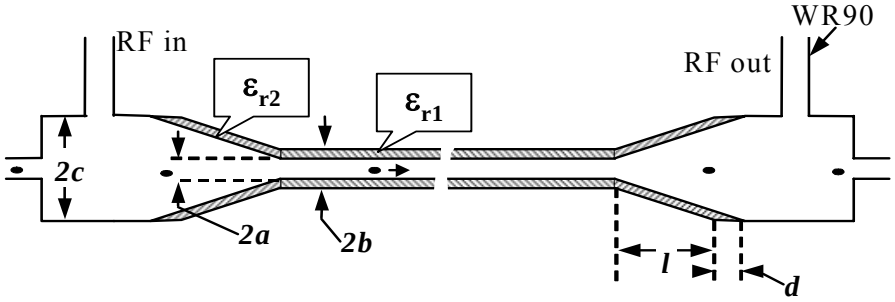

Figure 3.1. The Schematic Drawing of the Modular Dielectric-Loaded Accelerating Structure Which Consists of Three Functional Parts: RF Input/Output Coupler; Tapered Impedance Matching Section; Central Particle Acceleration Section.

3.1 Design and Fabrication

We use Microwave Studio®, a commercial EM simulation tool, to simulate the coupler, taper and entire structure respectively. The S parameters are obtained, and dimension tolerance is computed as well. In the second part of this section, we will present the fabrication of this modular DLA structure.

RF Simulation of the Coupler. We have developed a single port design by optimizing a set of parameters shown in Figure 3.2 to maximize the efficiency of mode conversion from the dominant mode, TE_{10}, in the rectangular waveguide to the accelerating mode, TM_{01}, in the circular waveguide. The length l is to determine the distance of the rectangular waveguide to the wave stopper in the circular waveguide (a smaller radius circular waveguide which is cutoff for X-band but can make the beam go through). The 3-D coupling slot is optimized by two dimensions, the height h and length a_l, but with the width fixed at the same as the width of WR90 waveguide.

The electric field distribution and S parameters of the optimized single side structure are given in Figure 3.3 and Figure 3.4 respectively. As shown in Figure 3.4, S21 is almost 0 dB in the region of 11.424GHz, which means that nearly 100% of energy from rectangular TE_{10} mode has been converted into circular TM_{01} mode. The peak electrical fields around the corners (blended at a radius of 2mm) of the coupling slot are to be less than 40 MV/m for 100 MW RF power, which is well below the copper surface breakdown threshold.

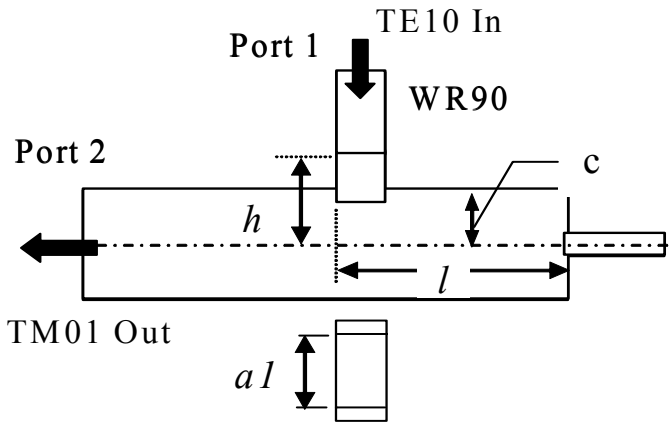

Figure 3.2. Major Simulation Parameters for Optimizing Single Port Coupler.

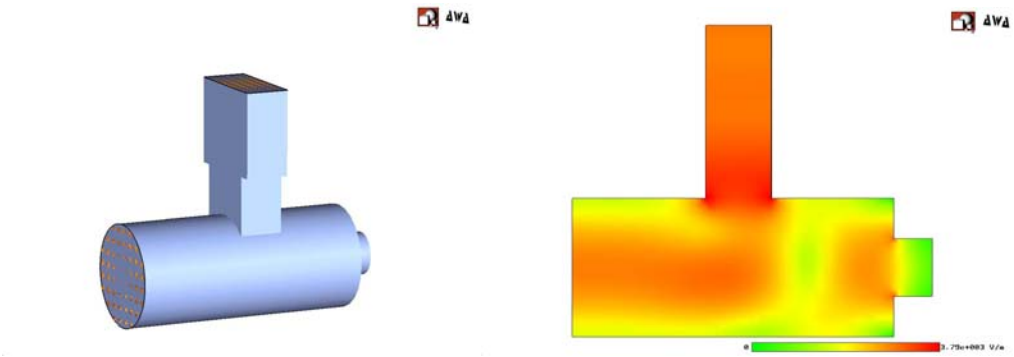

Figure 3.3. Electric Distribution of Single Port Coupler by Microwave Studio®.

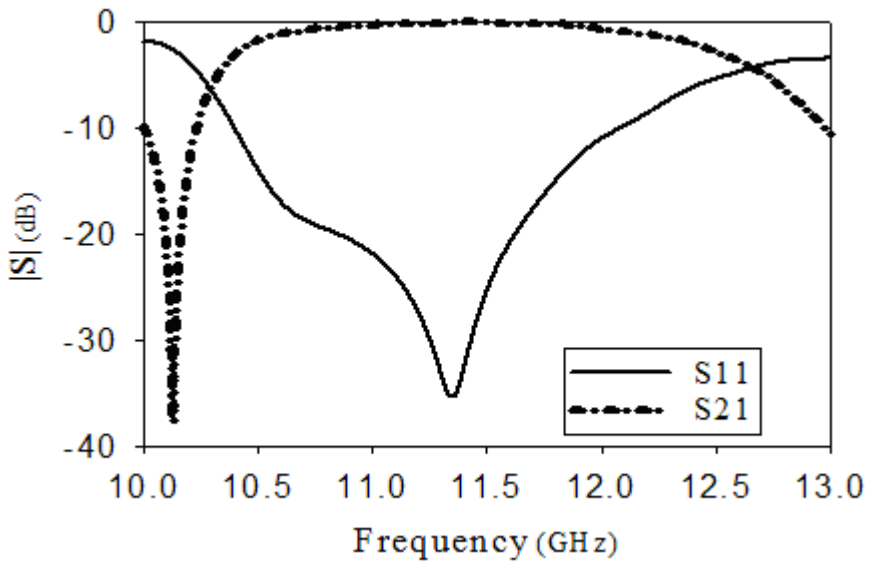

Figure 3.4. Simulation Results of S-parameter for the Single Port Coupler by Microwave Studio®.

RF Simulation of the Dielectric Taper. The purpose of the tapered matching section is to match the wave impedance between the dielectric loaded circular waveguide (dielectric loaded accelerator section) and the regular circular waveguide where the RF coupling structure is implemented, thus achieve high transmissions. As shown in Figure 3.5(a), the geometry of taper section is determined by its length *l* when the diameters of both the dielectric-loaded waveguide and the regular waveguide are predetermined. The dielectric constant of the taper can be somehow slightly different from the dielectric in accelerating section due to the different material suppliers. The parameter d is determined by $d = \frac{b-a}{c-b}\lambda$. The goal of taper section design is to find out a proper length *l* with acceptable S_{11}, which is a measure of the reflection coefficient. Here, we take alumina based DLA structure as an example to show the simulation results. Figure 3.5(b) gives the electric field pattern of a taper section for a dielectric accelerating structure with dielectric constant ε_{r1}=9.4 where a=5mm, b=7.185mm and c=12.079mm. In Figure 4.6, the reflection coefficient S_{11} is simulated with the dependence on the taper length and dielectric constant. In our final drawing, the length *l* is chosen to be 40 mm with the expected S_{11} would be -19 dB for alumina material ε_{r2}=9.4.

It is barely hard to imagine that the better performance will be obtained with the longer dielectric taper due to the smoother impedance transition. However, practically the impedance matching section is not allowed to be long due to the limitation of the total structure length. Figure 3.7(a) shows another dielectric taper geometric design [52] for $Mg_xCa_{1-x}TiO_3$ based DLA structure, which we can reach a lower reflection with a wider frequency range in a shorter length relative to the old design (Figure 3.5(a)). The new taper design adds an additional geometric parameter *t*1 so that the optimization becomes

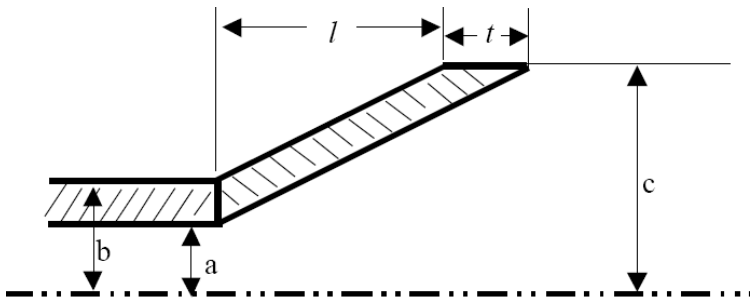

(a) Geometric design of the dielectric taper.

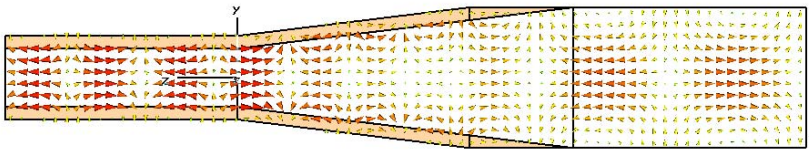

(b) Electric pattern.

Figure 3.5. The Tapered Impedance Matching Section of the Modular DLA Structure.

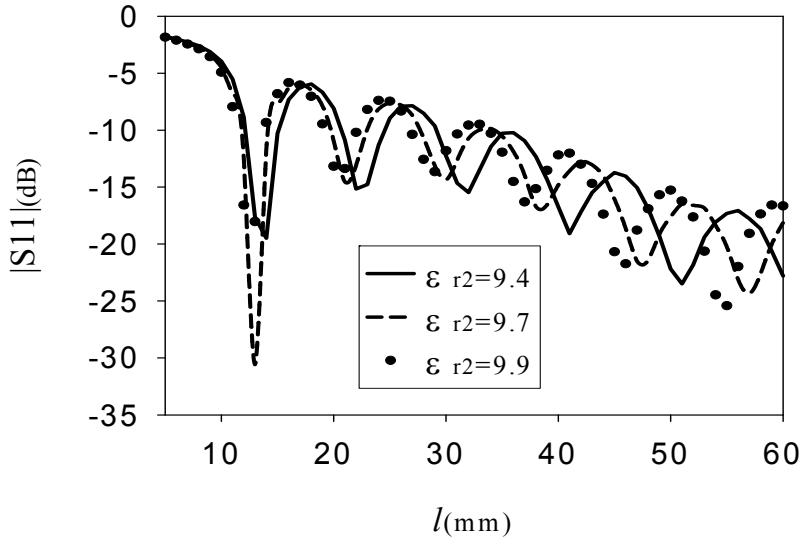

Figure 3.6. Simulated S-parameters with respect to the Dielectric Constant Varies.

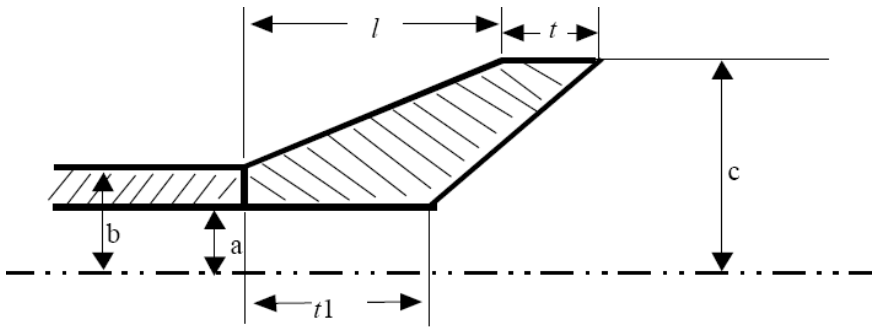

(a) Dimensions.

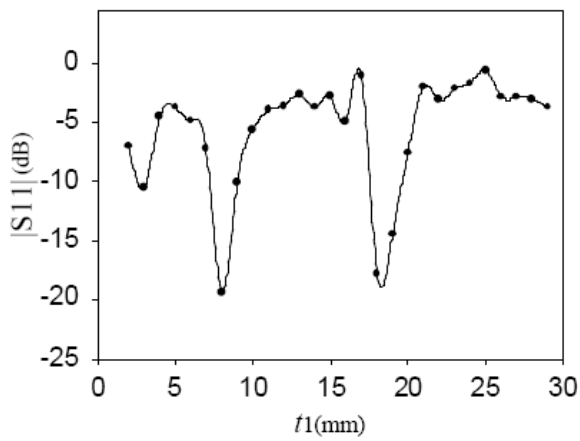

(b) The reflection performance of the dielectric taper made by $Mg_xCa_{1-x}TiO_3$ with the fixed *l*=30mm and t=15mm.

Figure 3.7. The New Dielectric Taper Design for $Mg_xCa_{1-x}TiO_3$ Based DLA Structure (with Dielectric Constant of 20).

more flexible, and also make it possible to refine its properties by modifying t*l* even after the copper housing of the dielectric taper has been made. Figure 3.7(b) shows the reflection performance of the dielectric taper with fixing *l*=30mm and t=15mm. Dimension a and b for the $Mg_xCa_{1-x}TiO_3$ based DLA structure are 3mm and 4.567mm, and the coupler radius c is the same as the used in the alumina based DLA structure, 12.079mm.

RF Simulation of the Complete DLA Structure. The complete traveling wave accelerating structure is simulated by Microwave Studio® as well. Figure 3.8 plots the simulation results on the alumina based DLA structure which has the geometric and accelerating parameters shown in Table 2.1. We see in Figure 3.8, by a carefully designed coupler and taper, almost all of the microwave energy from the rectangular waveguide (TE_{10} mode) goes through the dielectric loaded traveling wave accelerating structure (TM_{01} mode) at the designed operating frequency, 11.424GHz. The S-parameter of the whole structure will be presented in the section 3.2 as a comparison with the bench measurement results.

Fabrication. The each section of this modular structure is machined separately. Because the coupler is designed to be a wide bandwidth coupler, it can be reused for any dielectric material based X-Band DLA structures. Only the dielectric taper and acceleration sections, and their own copper housing need to be specifically machined. Figure 3.9 shows the mechanical drawing of the assembly, in which, obviously, machining taper section is very critical. Because the entire structure is connected by four

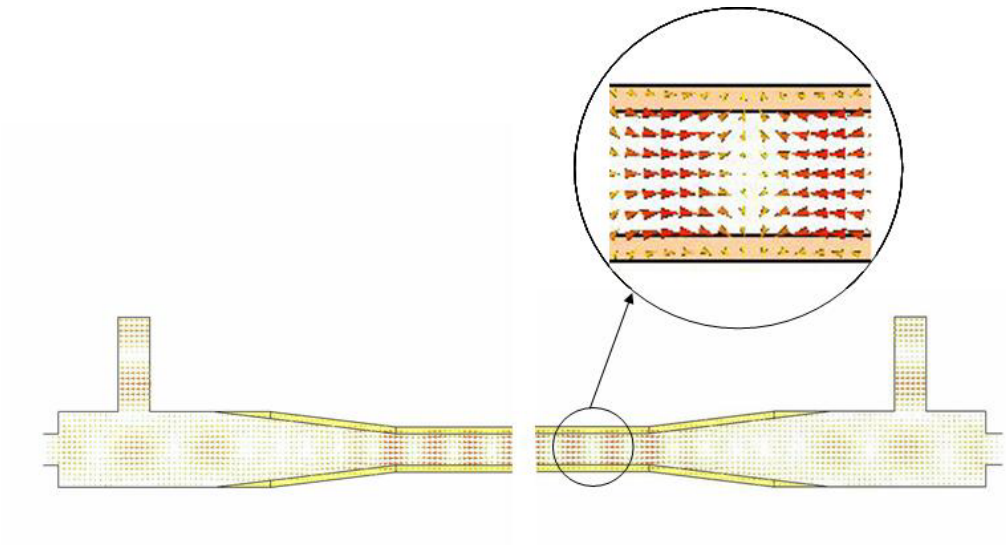

Figure 3.8. With Properly Selected Dielectric Constant and Loading Geometry, the Wave in the Dielectric Loaded Accelerating Structure will Travel at the Speed of Light and its Pattern is Good for Accelerating the Particles at the Given Frequency, here, 11.424GHz.

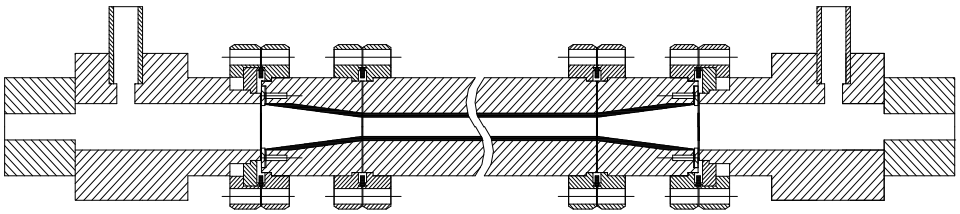

Figure 3.9. Mechanic Drawing of Designed Modular Accelerating Structure.

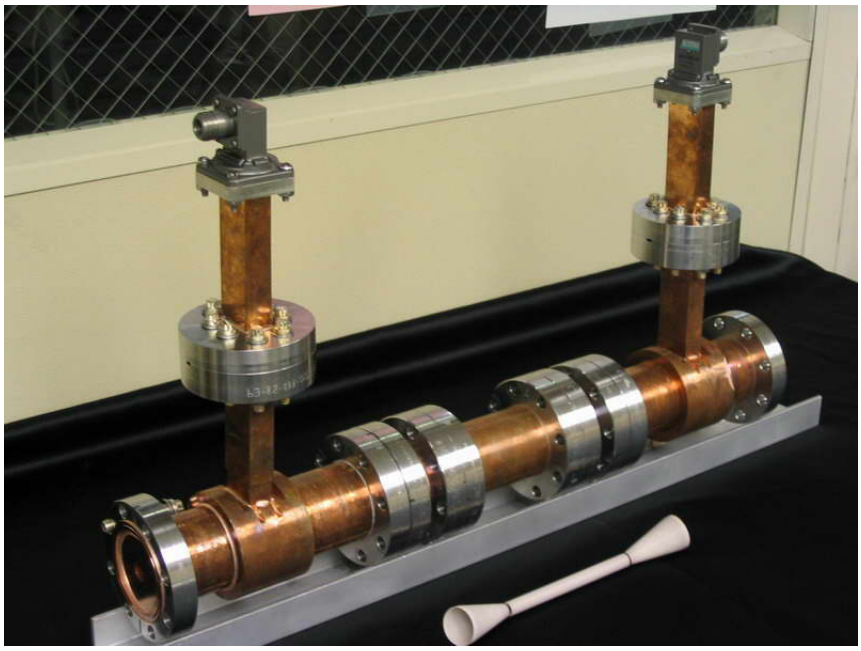

Figure 3.10. Finished 11.424 GHz Dielectric Loaded Modular Accelerating Structure.

flanges, it must be designed properly for meeting both the vacuum and electrical requirements. For example, if the outer face of dielectric taper does not match with inner face of copper taper, i.e., there exist a vacuum chamber between them, the transmission coefficient will drop for the structure. Also, if either the dielectric or copper sections cannot touch evenly, i.e., there exist a vacuum gap between the sections, it will lead to a strong local field enhancement that may cause dielectric breakdown under the high RF field condition.

All flanges and copper section were brazed at SLAC. The ceramic taper is machined by Advanced Ceramics Company and all ceramic components were cleaned and baked. Dielectric tube is fixed inside the copper tube by custom-made gaskets for keeping the vacuum requirement and face contacts between the taper and the accelerating section. The picture of the finished assembly of 11.424GHz traveling wave accelerating structure is shown in Figure 3.10, in which the up-end of the two arms are coaxial-to-rectangular waveguide adapters for use in bench measurements only.

3.2 Bench Testing

To evaluate the performance of the DLA structures after machining we have a set of RF bench measurements on it. First of all, we use RF Network Analyzer to measure the transmission and reflection performances of the device in our interested frequency range; then we set up a short pulsed RF circuits to test the time response of the structure; the third step is a beadpull experiment that provides us the profile of the accelerating gradient on the axis.

S-Parameter Measurement. Figure 3.11 shows the assembly under the test by HP-8510C vector network analyzer. The corresponding result is shown in Figure 4-10(a) and (b), in which Figure 4-10(a) is the coupler to coupler tests result and its comparison with s-parameter S21 from EM simulation, and Figure 4-10(b) is that of the whole assembly.

Figure 3.12 shows good agreement between HP analyzer test result and EM simulation result except that the HP analyzer result shows more discontinuities which the EM mode does not reveal. These discontinuities are believed to be caused by the gap between the standard vacuum flanges and machine errors. As expected, these discontinuities have very small effect to the performance of coupler in the frequency range where we are interested in. But from Figure 3.13 which plots the data of both measurement and simulation of the alumina based DLA structure, a big difference is noticed between them. The tested S21 is much lower than that from the EM simulation. Such difference tells us that there exists some unexpected mismatching in the whole assembly. A speculation could be the machine error in the tapered matching section and/or the faces of dielectric were not perfectly touched between the dielectric tube and the dielectric taper. EM simulation shows that the small chamber formed inside the flange may be the biggest source of mismatching. Figure 3.14 shows the S-parameters of the $Mg_xCa_{1-x}TiO_3$ based DLA structure. The transmission coefficient, S_{21}, is -2.4 dB and the reflection coefficient S_{11} is –10 dB at the frequency 11.427 GHz. Considering that there will be different ambient temperature and vacuum condition at NRL where we test the structure with a high power RF, these S-parameter curves will shift down a few MHz to ~11.424GHz.

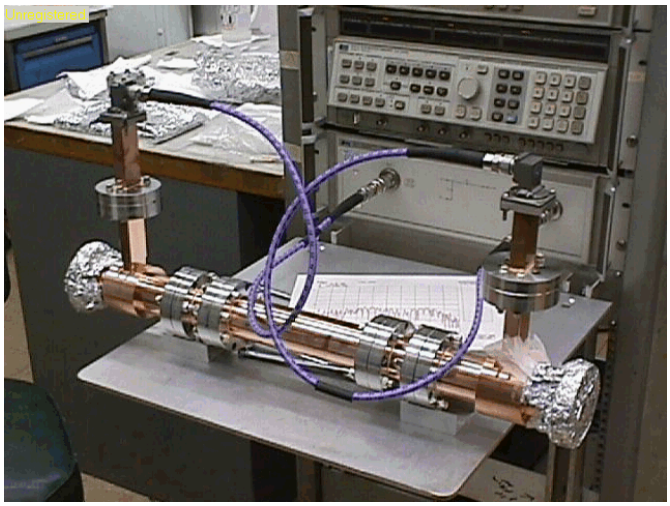

Figure 3.11. Modular Accelerating Structure Under Test by HP8510C Network Analyzer.

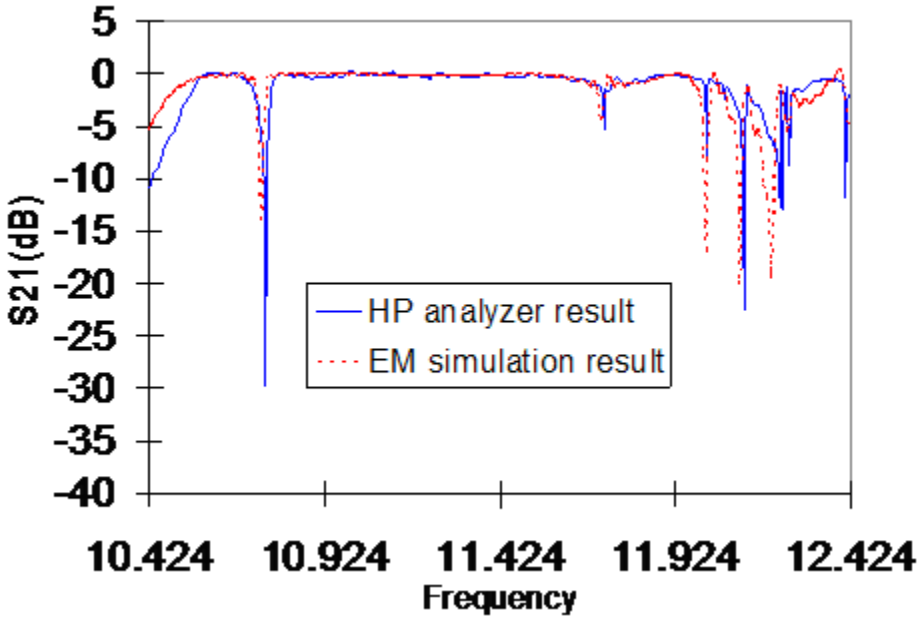

Figure 3.12. Comparison of Transmission Performance, S21, Between the Measurement and Simulation Results of the Coupler to Coupler.

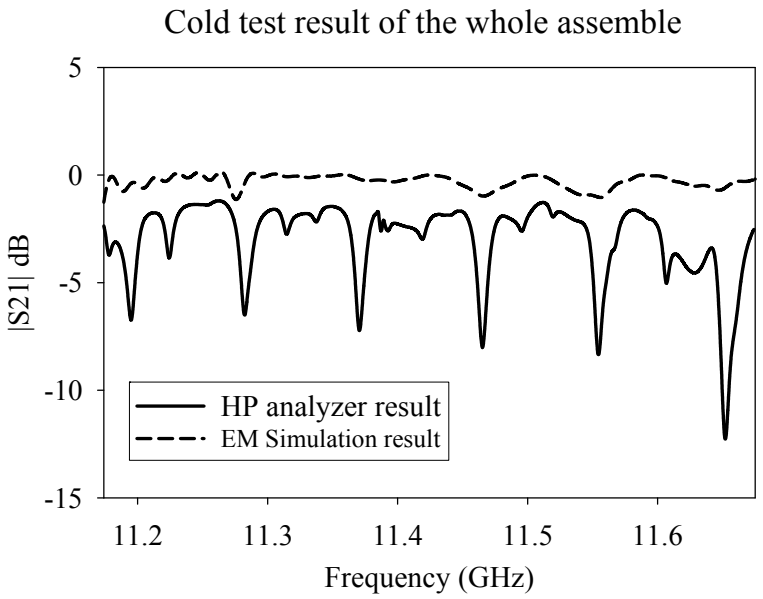

Figure 3.13. Comparison of Transmission Performance, S21, Between the Measurement and Simulation Results of the Complete DLA Structure.

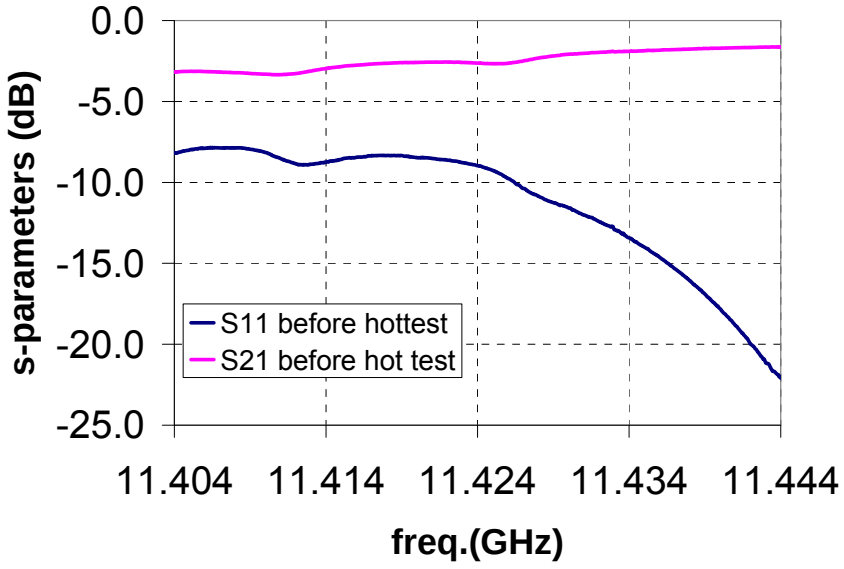

Figure 3.14. MCT DLA Structure Bench Test Results Before High Power RF Test at the Naval Research Laboratory.

Time Response Measurement. To test the up-limit of pulsed RF for that the dielectric based tube can handle, we use available 11.4GHz Magnicon at NRL to do high power test. Before that hot test, we established a short pulsed RF time response test bench in the lab to simulate and check the time response of our under test structure so that it can provide some information as reference to high power test. The configuration of the test bench is shown in Figure 3.15. Due to the unavailable RF source over 8GHz at the lab we adopt a frequency doubler to reach the frequency we need. A PIN switch is used to set up down to 10ns RF pulsed. The time response at each port is detected by the directional coupler and the connected crystal detectors, and shown in an oscilloscope. We generate 200ns duration and 10Hz the RF pulse, which is same as what we used in hot test. Result is presented in Figure 3.16.

Bead-pull Experiment. Slater's theorem [53] states, in cavity, the fractional change in frequency is proportional to the fractional change in stored energy which in turn is proportional to the square of the field times the polarizability of the perturbation

$$\frac{\Delta\omega}{\omega} = -\frac{\varepsilon\alpha_e}{4U}|E|^2 \tag{3.1}$$

where E is the unperturbed electric field, U is the stored energy in the empty cavity and α_e is electric polarizability of the perturbing object provided that the perturber is dielectric material. In [54] Carter derived formula for perturbation of a pill-box cavity by a dielectric sphere and analyzed and verified its accuracy under some assumptions. For traveling wave structure, Steele [55] developed a non-resonant perturbation theory, which determines the phase and field strength at a point inside a microwave structure by measuring the reflection produced at the input port by a perturbing object. The relation is

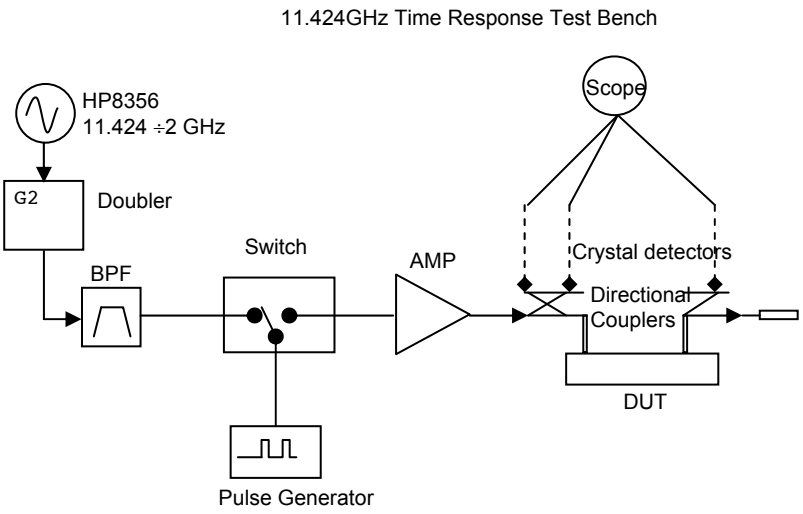

Figure 3.15. Block Diagram of the Time Response Test Bench.

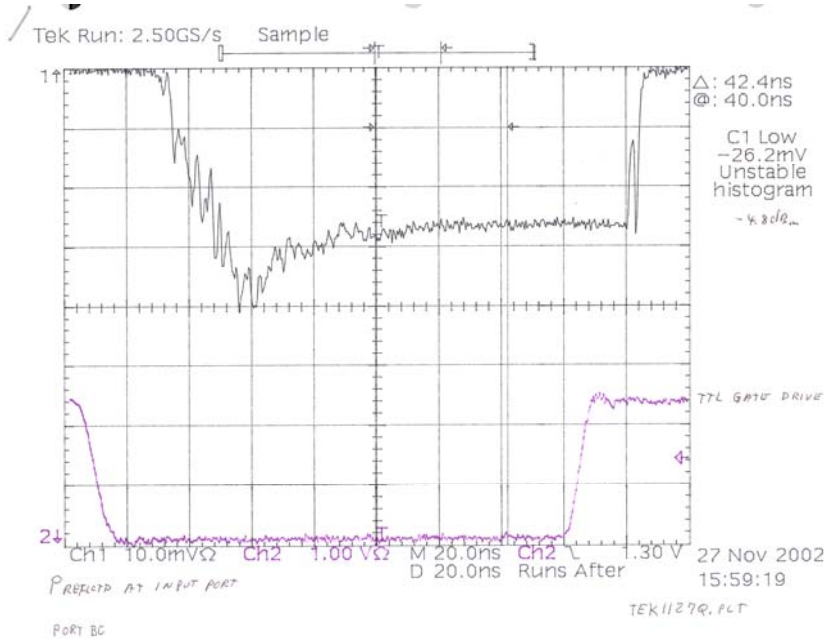

(a) Reflect power

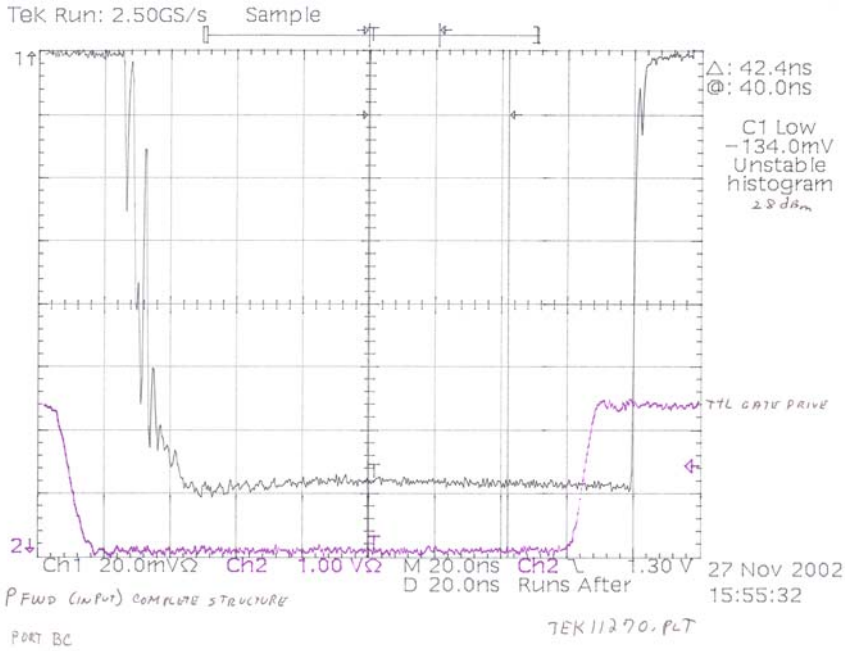

(b) Forward power

Figure 3.16. 200ns Long Pulsed RF Response.

$$\Delta S_{11} = -\frac{j\omega}{2P_i}(\varepsilon\alpha_e|E|^2 - \mu\alpha_m|H|^2)e^{j2\varphi} \quad , \tag{3.2}$$

where P_i is input RF power, and α_e and α_m are tensor polarizabilities. For dielectric bead in our perturbation measurement, $\alpha_e=4\pi r^3$ (r is radius of bead), and$\alpha_m=0$ [56]. In [57], the authors suggested the test bench in which Steele's theory was applied. More recently, the method is used to measure traveling wave muffin-tin accelerating structure at SLAC [58].

3.3 Multipactor of Alumina Based DLA Structures

Although the RF signal response can be characterized through the cold tests described in the previous section, some fundamental issues, such as RF breakdown and vacuum properties, have to be answered by the real high power RF experiment. In this section, we mainly report the results from Argonne National Laboratory / Naval Research Laboratory joint programs, in which we use the X-band Magnicon as high power RF source to test our designed Alumina based X-band modular DLA structures.

The X-band Magnicon developed at the Naval Research Laboratory [41] has been used as the external high-power RF source to test the DLA structures. The Magnicon can provide currently ~12 MW, up to 50MW in future goal, RF signal with a 200 ns pulse length from either of its two output arms. Figure 3.17 shows the experimental layout and diagnostics used: directional couplers are used to monitor the reflected, incident and transmitted signals; four ion pumps are used to evacuate and to monitor the vacuum level in the system; and two CCD cameras are used to look for visible light along the axis of the structure (in the event of arcing) from both the upstream and downstream ends. The vacuum pressure of the system was kept under 10^{-7} Torr during the high power test.

Observation of Multipactor. The design parameters of the tested alumina based modular DLA structure are shown in Table 2.1. After vacuum baking for two days at 100°C, we began the high power test and observed a considerable increase in pressure (1e-7 Torr) due to outgassing at low power (10 kW). As expected, the outgassing steadily decreased during RF conditioning and we eventually reached 2e-8 Torr. The incident power has been increased up to 5 MW (equivalent to an accelerating field of 8 MV/m) with an RF pulse length of 150 ns (FWHM) with no signs of breakdown observed. However, in the experiment some unexpected physical phenomena were observed (1) the fraction of transmitted power decreased with the amplitude of incident power; and (2) light was being emitted from the inner surface of the dielectric. These surprising phenomena were eventually understood to be caused by single-surface multipactor on the dielectric surface driven by the normal component of the TM01 mode of the DLA structure. Multipactor is an electron multiplication process that can take place on surfaces exposed to RF fields in vacuum. It occurs when an electron gains energy from the RF field and strikes the surface with an impact energy K in an energy range with secondary electron yield δ (t) (the ratio of electrons emitted from the surface to electrons impacting the surface) greater than 1. This energy range is confined within the two thresholds, e_1 and e_2, which are known as the first and second crossover points of the secondary electron emission curve [59], respectively. However, unlike the common dielectric multipactor happened in the application of RF window where typically multipactor saturates with the power absorption only a few percent of the incident RF, the multipactor in this DLA structure case absorbs considerably high power from the incident RF.

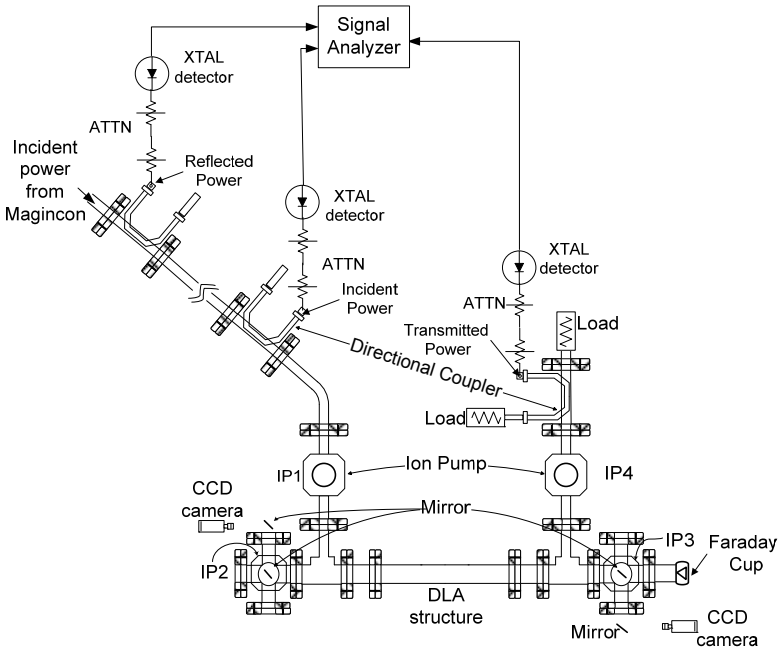

Figure 3.17. Experimental Setup Used to Test DLA Structures with High Power RF.

Figure 3.18 shows the measured transmission and reflection coefficients, and the light intensity vs. incident RF power. It shows that the transmission coefficient is constant for incident power less than ~80 kW. Then it decreases from 75% to less than 25% as power goes from this level to 5 MW. The incident RF power at this knee point on the RF transmission coefficient curve is defined to be the transmitted power dropping threshold, and is a parameter used to compare characteristics of different material under the similar experimental conditions. However, in this same interval of power, the reflection coefficient is approximately constant, indicating that the power was lost inside the dielectric tube. We term this lost power the missing power. In Figure 1.16b, we see that the missing power follows approximately the same trend as the emitted light intensity. Note that in the case of the high power RF window, multipactor causes power loss of about a few percent, but here significantly higher loses are observed due to the presence of both the longitudinal and radial electric field [60].

Physical Model. To explain these results, a new physical model was developed by Power [60] and coauthors. This multipactor model computes electron trajectories inside the structure under the influence of the dc and RF fields. The dc field E_{dc} arises from the radial space-charge field of a thin cylindrical shell of secondaries [Figure 3.19(a)] with trajectories near the surface of the dielectric (Because of symmetry, the surface charge on the dielectric does not contribute to the dc field in the vacuum region.). The RF field in the central vacuum region of the acceleration section of the DLA structure has pattern of TM_{01} mode which can be simply expressed as

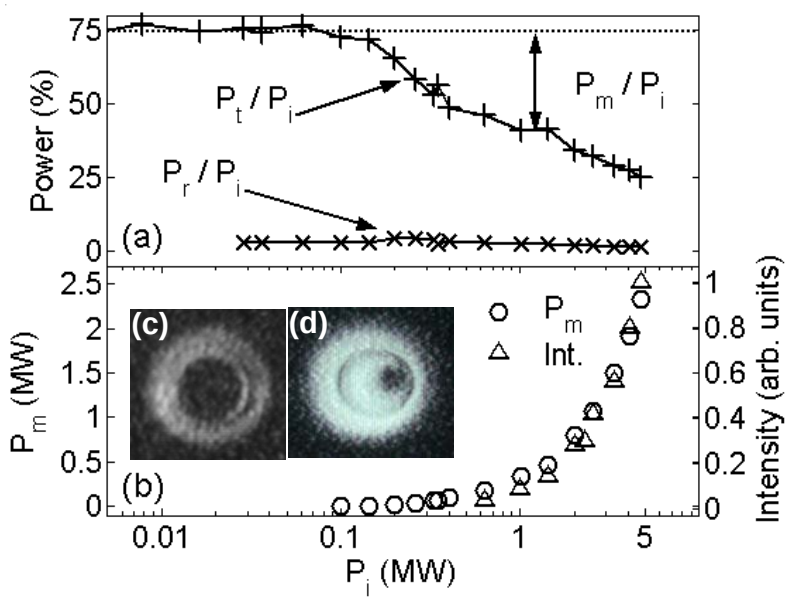

(a) The transmission and reflection coefficients; (b) The missing power and the time integrated light intensity as a function of incident power; (c) The image of light observed during the experiment with a camera focused on the center line of the dielectric tube; (d) The image of light with camera focused on the off-center position. P_i is incident power, P_t transmitted power, P_r reflected power, P_m missing power. This figure is courtesy to reference [60].

Figure 3.18. Alumina Based DLA Structure High Power Test Data.

$$\begin{cases} E_z = E_{rf} I_0(k_r r)\cos(\omega t - k_z z) \\ E_r = E_{rf}(\frac{k_z}{k_r}) I_1(k_r r)\sin(\omega t - k_z z) \\ H_\varphi = E_r / Z_{TM} \end{cases}, \tag{3.3}$$

where E_{rf} is the RF field amplitude, k_r and k_z are the radial and longitudinal wave numbers, respectively, ω is the angular frequency, $I_n(x)$ is the modified Bessel function of the first kind, and Z_{TM} is the impedance of the TM wave.

The assumption of a thin shell distribution of electrons near saturation is justified since the computed trajectories stay near the surface. The comparatively low velocity of the secondary electrons allows us to neglect the azimuthal RF magnetic fields, permitting us to reduce the problem to 2D [Figure 3.19(b)], in which the equations of motion near the surface become

$$\begin{cases} m\ddot{z} = -eE_{rf}\cos(\omega t - k_z z + \theta) & (3.4a) \\ m\ddot{r} = -eE_{dc} - eE_{rf}\left(\frac{\pi a}{\lambda_z}\right)\sin(\omega t - k_z z + \theta) & (3.4b) \end{cases},$$

where the dot represents differentiation with respect to time, θ is the RF phase at the instant of emission, λ_z= 2.6 cm is the guide wavelength, a is the inner radius of dielectric tube, and we have used $I_0(k_r r)$= 1 throughout the vacuum region and $\frac{k_z}{k_r} I_1(k_r r) \cong \left(\frac{\pi a}{\lambda_z}\right)$ near the surface (See chapter 2 for details). Note that the coordinate r in the equation (2) is defined so that r = 0 corresponds to the surface of the dielectric. As shown in Figure 3.19(b), the electrons are emitted from the surface with emission angle ϕ_0 and emission velocity $v_0 = \sqrt{2e_0 / m}$, where e_0 is the emission energy and m is the mass of the electron.

Multipactor growth begins when electrons strike the surface with an impact energy K greater than the minimum energy for the material which δ is greater than 1. This energy threshold, e_1, was estimated by calculating the energy gained at impact within one RF period by electrons launched from rest ($e_0 = 0$), over all possible emission phases ($0° < \theta < 360°$), as a function of the RF field amplitude E_{rf}, with E_{dc} set to 0 (i.e., no initial space-charge cloud). Solving Equation (3.4a) with $E_{rf} \approx 1$ MV/m (Fig. 1, power loss at $Pi \approx 80$ kW) gives that the maximum impact energy is $K \approx 60$ eV, which falls within the expected range for alumina: $3 < e1 < 300$ eV [61, 62]. Once the multipactor threshold is crossed ($K > e1$), the number of electrons inside the DLA structure will rapidly increase until saturation, which occurs when the space charge field due to the secondary electrons becomes large enough to suppress further electron multiplication. To simplify our model, we assume that secondary electrons are emitted normal to the surface [$\phi_0 = \pi/2$ in Figure 3.19(b)]; are mono-energetic, with energy e_0; and experience a space-charge field E_{dc} due to the total number of electrons in the structure is not adjusted to take into account the instantaneous radius of the electron.

The essential features of the saturation condition are most easily understood by temporarily setting the emission energy e_0 to 0. (Realistic values are used in the detailed simulations.) Electron trajectories were computed for a uniform distribution of emission phase angles θ. For each value of E_{rf}, E_{dc} was systematically raised from zero until saturation occurred. In this model, the trajectories are permitted to hop along the surface by the immediate emission of new electrons at the point of impact, when the RF phase permits this to occur. Trajectories that can propagate indefinitely will lead to exponentiation of the electron density, provided that $K > e_1$. Slightly below saturation,

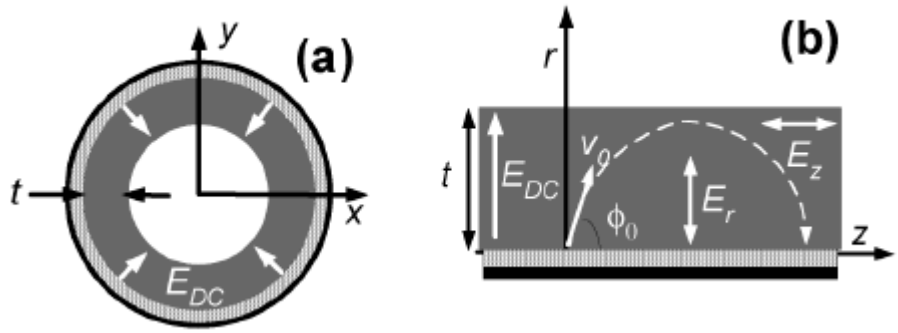

(a) End view (b) side view.

Figure 3.19. Model of Single-Surface Multipactor with Both Normal and Tangential RF Fields and Normal DC Field Caused by an Electron Cloud of Thickness t (shaded) in the Cylindrical DLA Structure.

such trajectories fall within a narrow range of emission phases θ_{min} to θ_{max}, with the hop time $\tau \approx T_{rf}$, the RF period. After a few hops along the surface, these trajectories undergo phase focusing until $\tau = T_{rf}$. Trajectories just outside this narrow range of emission phases fall out of phase with the RF field after several hops and end when the RF phase at impact suppresses reemission. All the other trajectories either stop after their first hop or do not leave the surface at all. As E_{dc} is increased toward saturation, τ decreases, and θ_{max} approached θ_{min}. Saturation is reached when E_{dc} has increased to a value such that the duration of the longest trajectory is exactly T_{rf}. This resonant trajectory occurs when the sum of E_{dc} and the normal component of E_{rf} goes through zero and points into the surface, so that electrons can be accelerated outward.

Further insight can be gained by solving the equations of motion under the approximation that the k_z dependence can be ignored, since $\omega/k_z \approx c >> \ddot{z}$. Solving Equation (3.4b) with e_0 =0 shows that the above-mentioned resonant trajectory begins at the surface with RF phase $\theta = \pi + \arctan(1/\pi)$, occurs at dc field $E_{dc} \approx 0.303E_{rf}(\pi a/\lambda_z)$, and has an impact velocity $v = 2\pi e E_{dc}/m\omega$ normal to the surface. Solving Equation (3.4a), we see that the tangential velocity at impact is equal to its initial velocity (zero), since the trajectory lasts exactly one RF period. Thus, this regime of multipactor is driven by the normal component of the RF field. Since electrons gain energy from the RF field and lose it in collisions with the surface, the power lost is $P=N_eK/\tau$, where N_e is the number of electrons with impact energy K striking the surface per hop time $\tau = T_{rf}$. Since $N_e \propto E_{dc} \propto E_{rf}$ and $K \propto v^2 \propto E^2_{rf}$, the absorbed power scales as $P^{1.5}_i$ for this approximation, which shows reasonable agreement with detailed modeling. To check the validity of our model, we set e_1 =60 eV and varied e_0 over the expected range of 1.75–6.5 eV [61, 62]. To

estimate N_e, we calculated the charge enclosed per unit length, $\rho_e = eN_e/L$, where L, the effective length of the alumina DLA structure, should fall between the length of the center section alone, 200 mm, and the total length of 308 mm. Applying Gauss's law in cylindrical coordinates gives $\rho_e = 2\pi a \varepsilon_0 E_{\mathrm{dc}}$, where E_{dc} is the value of the space-charge field at saturation for a given RF field E_{rf}. The RF field amplitude E_{rf} in the DLA structure was estimated from the average power in the RF tube by averaging P_i and P_t. (Shielding of the RF at the surface by the electron layer is not a factor, because the plasma frequency is below the RF frequency.) The best fit to the experiment was found by setting e_0 = 2 eV and L =250 mm. The excellent agreement for this choice of values, as shown in Figure 3.20, suggests that this simple model is capturing the essential physics of this multipactor process.

Multipactor Suppressing. In order to suppress multipactor in the alumina DLA structure, the inner surface of alumina tube was coated with 20 nm thick TiN film. TiN is commonly used for lowering the secondary emission coefficient in high power RF window applications. The test shows an obvious reduction in the amount of power absorbed due to multipactoring.

Figure 3.21 compares the normalized power transmission (S21) curves for the coated and non-coated DLA structures. (Due to the slightly different values of the transmission coefficient at low incident power, caused by assembly variation, we normalized the transmission percentage for easy comparison between structures.) This comparison reveals two main differences between the two structures: multipactor initiation and multipactor saturation. (1) Multipactor initiation, as indicated by the

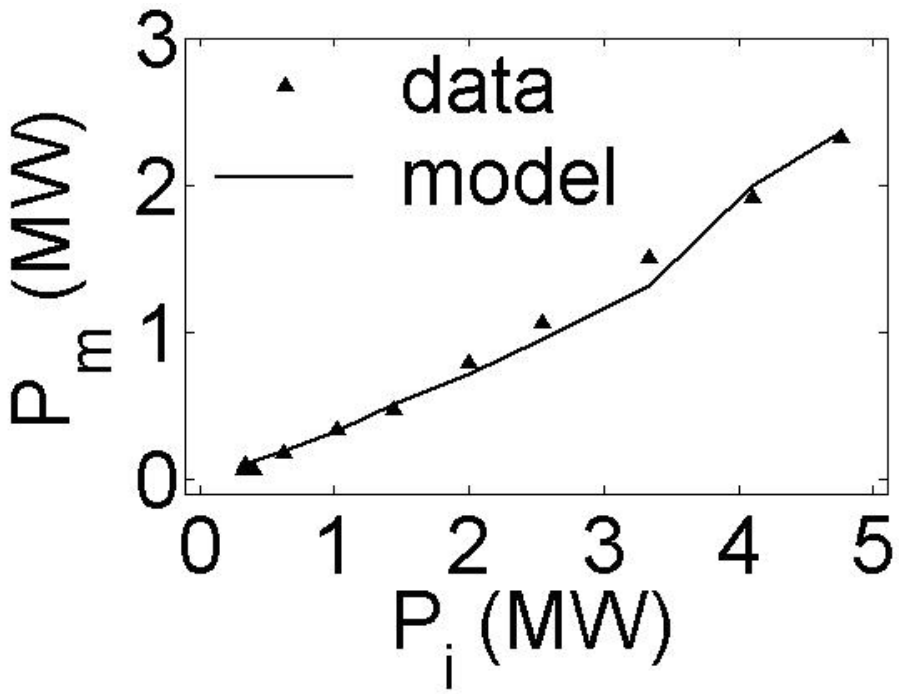

Figure 3.20. Comparison of Experimental Missing Power Data to the Model.

transmitted power dropping threshold, occurs at ~200 kW (corresponding to 1.6 MV/m accelerating gradient built up at upstream end) in the coated structure and at ~80 kW (1 MV/m) for the non-coated structure. (2) Over the incident power range of 1 MW to 5 MW (which is equivalent to accelerating gradients of 3.7 MV/m to 8 MV/m respectively) S21 no longer decreases with increasing incident power for the coated structure; i.e. it saturates.

As described above, the multipactor process only occurs when electrons strike the dielectric surface with a kinetic energy of impact (K) in the multiplication range between the first cross-over energy e_1 (typically for alumina, 10-100eV) and the second cross-over energy e_2 (typically for alumina, 1-10keV). While multipactor is occurring in the structure, an electron cloud is formed inside the dielectric tube and with large kinetic energy distribution range, K from e_1 to e_2. In general, the multipactor suppression coating (TiN) will shrink the multipactor range by raising e_1 and lowering e_2. With this in mind, we can now try to understand the differences between the coated and non-coated structures. Multipactor initiation occurs at a higher electric field level because the K required to initiate multipactor is now higher, e_1. On the other hand, the reason for the saturation of transmitted RF power is not fully understood, but it is believed to occur because some electrons with $K > e_2$ do not multiply. The reason that saturation was not observed in the non-coated tube was because the maximum K achieved was only ~2 keV [60] while e_2 was possibly near 10 keV so $K < e_2$. But in the case of the coated tube e_2 was estimated to be 1.5 keV which corresponds to an incident power of 1 MW.

In addition to the coating just described, we studied other method to suppress multipactor in dielectric-lined waveguide under strong RF field. During the high power

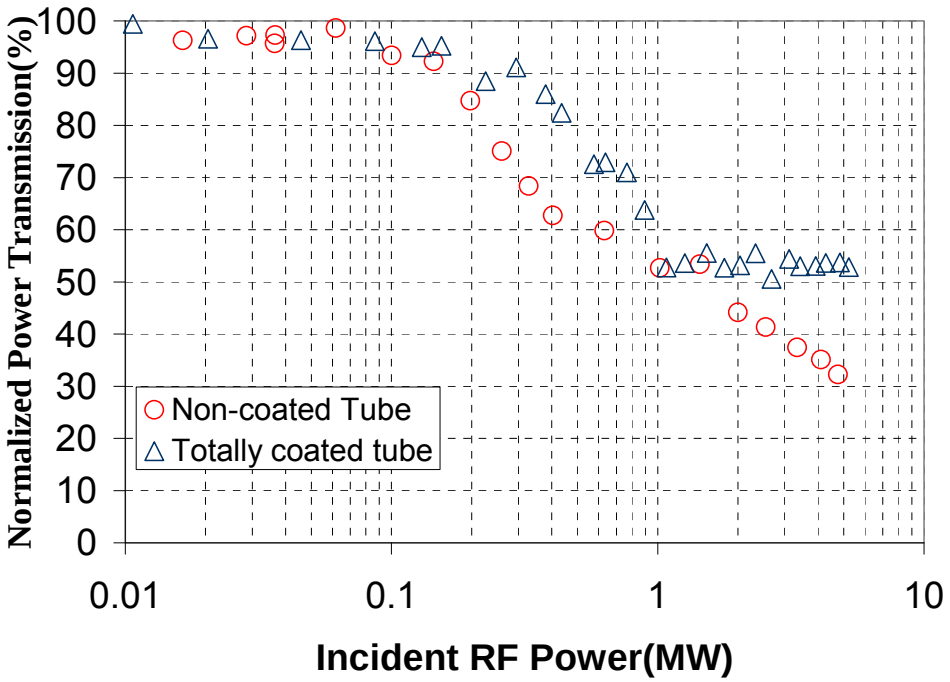

Figure 3.21. Comparison of the Power Transmission Curves for the Coated and Non-coated Alumina DLA Structures.

testing of the coated alumina DLA structure we introduced a uniform longitudinal magnetic field by using a solenoid installed outside the structure. Figure 3.22 shows the effect of the solenoid for a 150 Gauss axial magnetic field. In both the non-multipactor region (incident power below 200 kW) and the saturation region (incident power above 1 MW) the RF power transmission is not significantly affected. However, in central region this solenoid field caused an increase of RF power absorption by reinforcing the multipactor process. A model to explain this effect is under construction, and we will present it in future.

3.4 High Power RF Testing on $Mg_xCa_{1-x}TiO_3$ Based DLA structures

In general, DLA structures using high dielectric constant materials will obtain higher initial accelerating field for a given incident RF power [7]. For instance, an alumina-based DLA structure requires 80 kW of incident power while an $Mg_xCa_{1-x}TiO_3$, hereafter called MCT also, based structure needs only 27 kW to sustain a 1 MV/m initial electric field. This is because (Table 1) MCT's dielectric constant (20) is twice as large as Alumina's (dielectric constant 9.4), and the MCT-based DLA structure has a smaller hole size.

Observation of Dielectric Joint Breakdown. The high power RF testing of MCT based DLA structure shared the same location and configuration as the alumina tube. The detailed experimental results can be obtained from reference [32].The transmitted power proceeded smoothly from low power to 1 MW, which corresponds to 5.7MV/m (this is the field at the upstream end with reflection power considered). Unfortunately, the

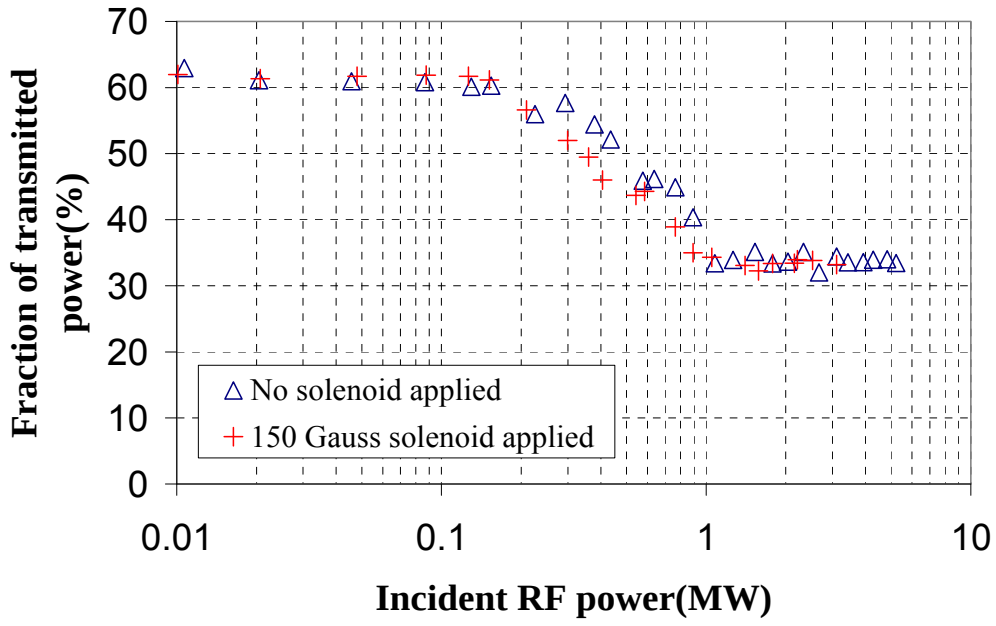

Figure 3.22. Transmitted RF Power as a Function of Incident Power With and Without an Axial Magnetic Field Applied.

structure arced when the incident RF power exceeded 1MW. Figure 3.23(a) shows the latest testing results. From the plot we can see that S21 starts dropping (multipactor initiation) at ~600 kW of incident power (equivalent to 4.5MV/m initial accelerating gradient), which is much higher than in the alumina experiment (1 MV/m). At the same time, the reflection curve did not have a corresponding increase. This indicates that the existence of multipactoring is much weaker than that shown in the alumina DLA structure. However, we did observe a permanent arcing point at 1 MW incident power (see Figure 3.24), which corresponds to 5.7 MV/m at the upstream end (10% power reflection considered). Thereafter, the light due to both multipactor and arcing coexisted as data was collected. The RF power applied to the MCT structure was stopped at 1.9 MW due to multiple arcing spots that appeared at a dielectric joint between the upstream end taper and the uniform acceleration section. During this time we observed typical breakdown traces on the oscilloscope (see Figure 3.23(b)). The transmitted signal was cut off and a strong reflected signal was observed during the second half of the RF pulse. After the experiment, we disassembled the tube and found clear burned marks showed on the end surfaces of the dielectric joint between the taper and straight sections. Figure 3.25 shows some Scanning Electron Microscope (SEM) images of the MCT sample taken from the tested DLA structure. As in the case of the RF window breakdown we find streamer tree marks on the gap surface.

Local Field Enhancement. Altogether we have accomplished three high power experiments on the MCT based DLA structure. But all of them showed the similar arcing phenomena. Combined with all high power tests on the MCT DLA structures, the

breakdown is believed to be caused by the existence of a micro scale vacuum gap in the dielectric joint. Because of the large dielectric constant discontinuity at the joint, it will have a strong local electric field enhancement. Based on the continuity of electric flux, the local longitudinal electric field should be enhanced by 20 (ε) times compared to the ideal (joint free) case. For this MCT DLA structure, the accelerating field is around 5.7 MV/m (10% power reflection considered) at the upstream end taper when 1 MW of incident power is applied. We can then estimate that the electric enhancement at the gap to be 100 MV/m. The distance of the vacuum gap is also directly related to absolute energy gain for electron emission when arcing happened.

The structure has been simulated by Microwave Studio® [63] with the parameters shown in Table 2.1 and a 20μm vacuum gap in the joint between the straight and the tapered dielectric tube near the downstream side. The numerical simulation (see Figure 3.26) shows that the highest electric field exists at the vacuum gap, which is 10 - 15 times higher than the gapless case (not shown). However, it should be pointed out that this electric field enhancement is probably higher due to the relatively coarse mesh applied to the simulation model (limited by our computer capability). Interestingly, this indirectly shows that the MCT DLA structure handled 60~100MV/m electric field without breakdown.

For metallic structures it is known that field emission can be the source of electrons for triggering an ionization breakdown. In our case, the physical process of the breakdown in the dielectric joints is not totally understood. A plausible explanation is that the electrons on the surface of dielectrics are driven out by the strong local field in the gap. When those electrons gain energy they heat the end surface of the dielectrics which

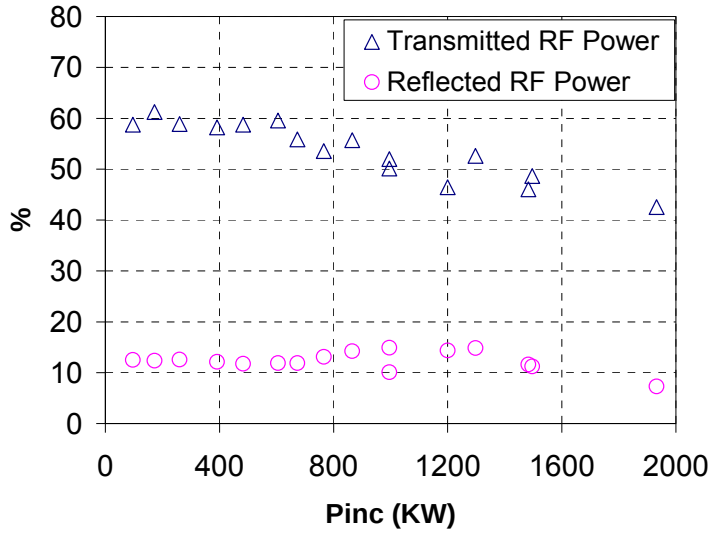

(a)Transmission and reflection data.

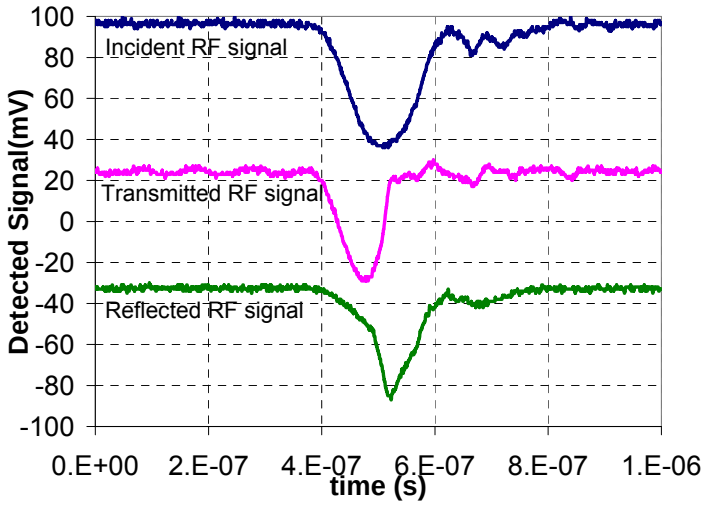

(b) Typical breakdown scope trace shown up at 1.9MW incident power.

Figure 3.23. The High Power RF Testing Data of MCT DLA Structure.

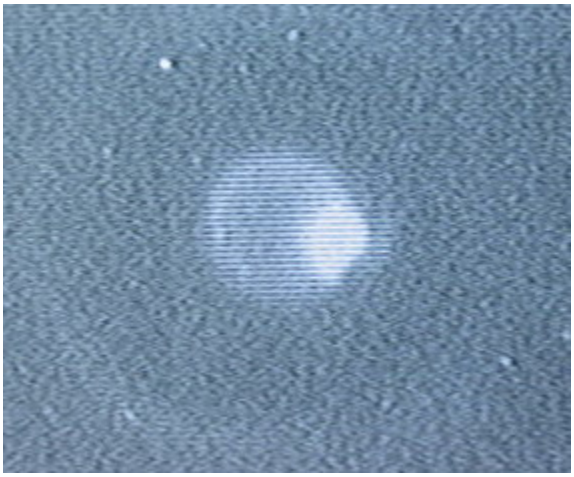

Figure 3.24. Bright Spot Observed During the High Power Testing of the MCT Based DLA Structure.

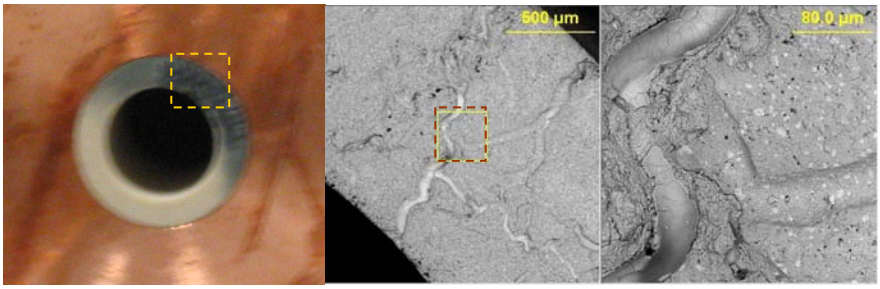

(a) (b) (c)

(a) Picture of breakdown marks on the dielectric end surface (in picture, outside of dielectric tube is a part of copper jacket). (b) SEM image of streamer-tree-like breakdown marks in 500 micron scale. (c) SEM image in 80 micron scale.

Figure 3.25. Breakdown Signature of $Mg_xCa_{1-x}TiO_3$ Tube During the High Power RF Testing on MCT Based DLA Structure.

then releases locally-available gas. Electrons also ionize the gas to form plasma. After that sparks occur because of the recombination of electrons and ions. If the field continues to increase, the plasma ions are accelerated back toward the now-cathode-like surface, releasing more gas. This positive feedback mechanism may lead to an enhancement of the plasma density, and eventually stop the RF signal propagation and form a destructive breakdown.

Dielectric Joint Bonding Experiment. Although the accurate physical mechanism of dielectric breakdown at the ceramic joint has not been totally understood yet, we have known that it initiates due to the local field enhancement at the micro-scale vacuum gap of the ceramic joint. To solve this problem, we may fill the joint with some bonding material which has dielectric constant higher than vacuum, therefore, field enhancement ratio would be reduced from 20 to a certain level for the $Mg_xCa_{1-x}TiO_3$ based DLA structure, and the higher accelerating gradient could be built up before reaching the dielectric breakdown threshold.

Our first try is to use a selected epoxy resin which has a very high dielectric strength (2400 V/mil) and a comparable dielectric constant (5.2). This means that the local field enhancement ratio is reduced to be 3.8, and higher built-up accelerating gradient is expected during the high power RF testing. However, the cons for epoxy as the fillings are its relatively poor vacuum performance and high volatility. The demonstration experiment was carried out on January 2005. For the MCT based DLA structure, a thin film of epoxy was put on the end surface of two taper joints respectively. But in the process, the thickness and the flatness of the filling are hard to control due to

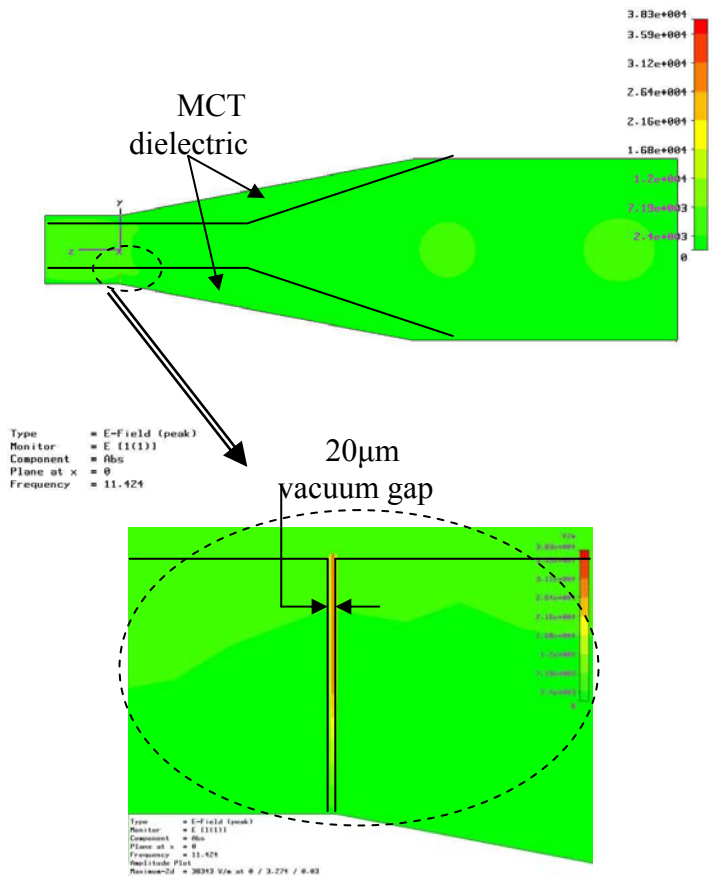

Figure 3.26. Numerical Simulation Demonstrates the Field Enhancement in the Small Vacuum Gap. From the Magnified Picture on the Bottom, It Shows the Highest Electric Field Built Up in the Vacuum Gap.

its viscidity increased by volatilization. The tube was baked 30 mins @177 °C to get it cured. Figure 3.27 gives a plot of S-parameter for this ceramic joint bonded MCT DLA structure. The fillings induced loss and electric discontinuities make the RF transmission and reflection degraded compared to the non-epoxy tube (Figure 3.14). For example, S21 drops to -3.8 dB and S11 of -5.5 dB at 11.43GHz.

While the high power RF testing at Naval Research Laboratory, we observed a different RF characteristics with the previous experiments on non-epoxy DLA structures. An observable bright spot showed up periodically at the upstream ceramic joint at a very low incident RF power (~60KW). However, unlike the dielectric arcing in our previous experiments on dielectric-loaded accelerating structure, this bright spot did not come with the apparent vacuum degradation and it appeared along the whole process of raising the incident RF power. After the high power RF experiment, at this lighting spot, we observed the biggest epoxy droplet at the inner surface of the upstream ceramic joint that formed by gravity while the tube lay horizontally for the epoxy curing.

Figure 3.28 shows the high power RF performance of the epoxy bonded MCT DLA structure. The fraction of the transmitted RF power keeps dropping very fast at the beginning (from 50% to 30%), and then the dropping speed becomes very slow. The reflection performance corresponds to the transmission roughly. From the curve, one signature of the multipactoring process of the loaded dielectric, that is knee-point curve [32, 60], did not show up along with the observation of secondary electron emission light inside the tube starting from a certain level of the incident RF power during the experiment, that is another signature of multipactor in our previous high power testing on the dielectric-loaded accelerating structures. The reason of the typical RF performance

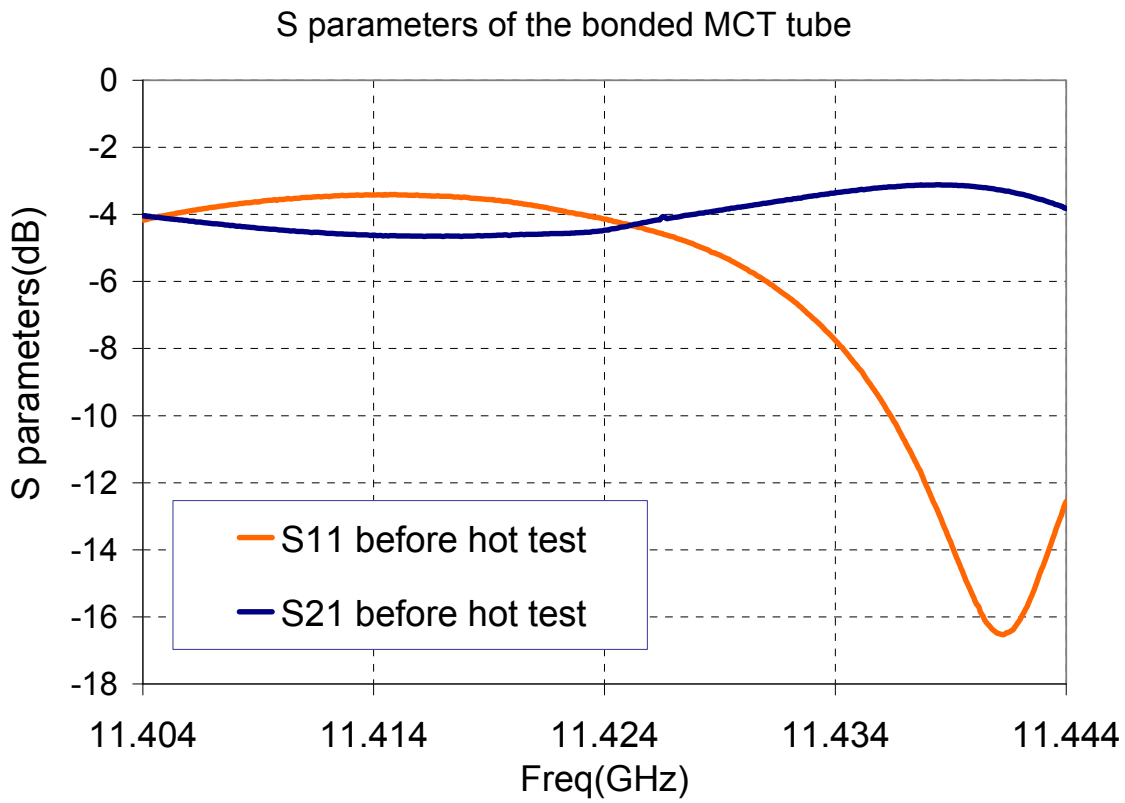

Figure 3.27. S-parameter of the Ceramic Joint Bonded MCT DLA Structure.

curve has not been obtained for the epoxy bonded DLA structure is because that the characteristics of the epoxy under the high vacuum and high field condition dominated the overall RF responses we measured in the experiment. The dielectric tube had suddenly broken down (with strong transmitted RF signal shutdown and total RF reflection) at the incident power of 1.9MW where the accelerating gradient had reached 7.3 MV/m, and the local electric filed at the upstream ceramic joint should be around 30MV/m by the enhancement ratio of 3.8. Compared to the non-epoxy MCT DLA structure experiment shown in Figure 3.29, which obtained the accelerating gradient of 5.7MV/m, the epoxy filling does have a certain level of improvement but only limited by the epoxy breakdown voltage instead of the loaded dielectric, $Mg_xCa_{1-x}TiO_3$.

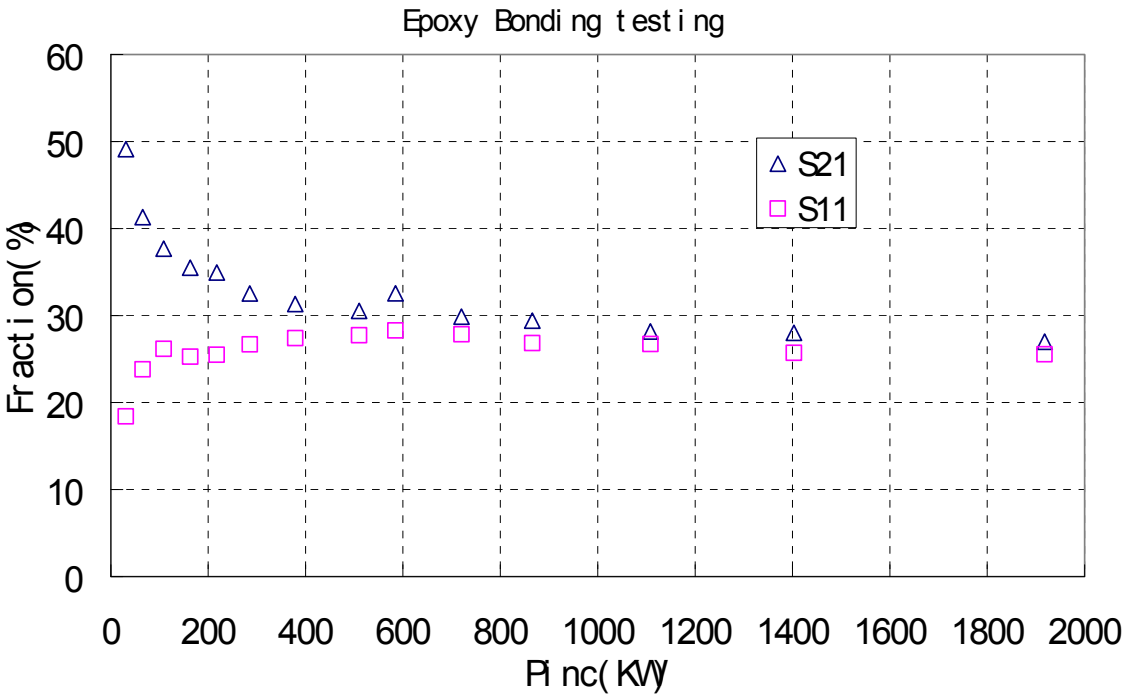

Figure 3.28. High Power RF Response of the Epoxy Bonded MCT DLA Structure.

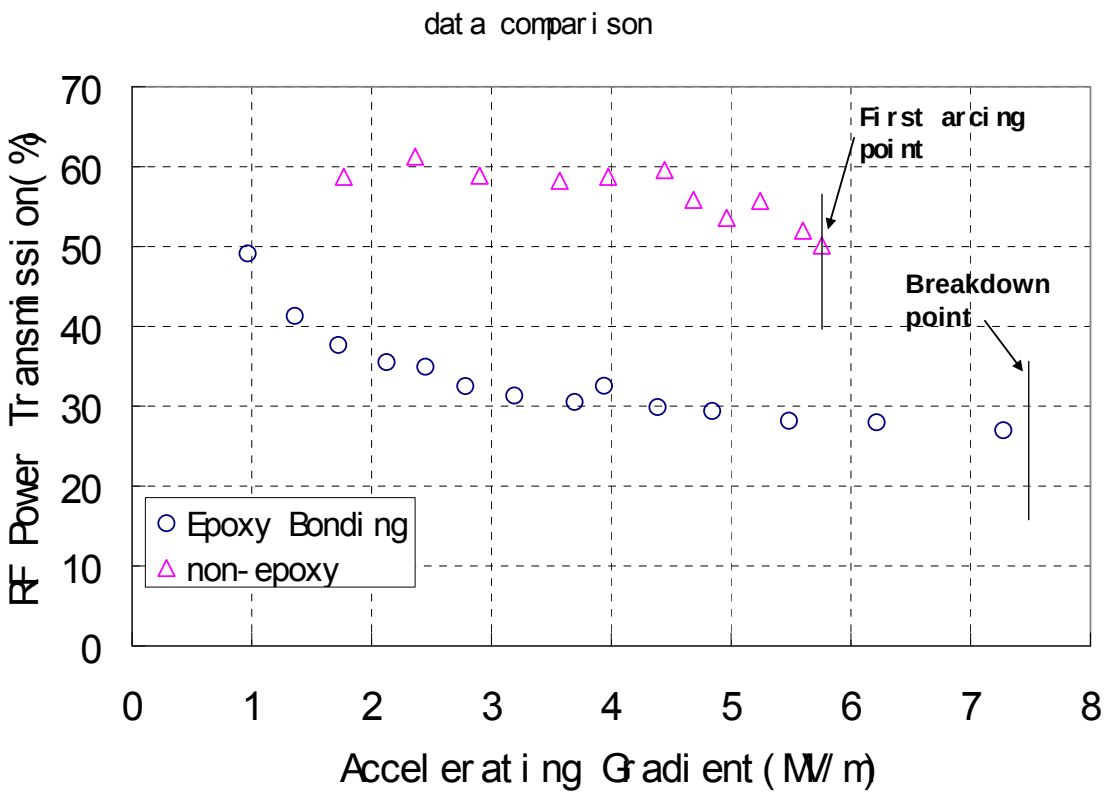

Figure 3.29. Comparison of High Power RF Transmission of Two Experiments, the Non-epoxy MCT DLA Structure and the Epoxy Bonding One.

CHAPTER 4

MULTILAYERED DIELECTRIC-LOADED ACCELERATING STRUCUTRE

4.1 Introduction

While the conventional DLA scheme has great potential as an advanced accelerating device, a major concern for it is its relatively high field attenuation per unit length, α_0. This is caused by strong magnetic fields at the metal wall ($r = b_1$) which in turn gives rise to large surface currents and hence large attenuation. Normally, one prefers high dielectric constant materials to keep the group velocity of the wave low ($v_g \approx 1/\varepsilon$) since that maximizes shunt impedance per unit meter, however, high dielectric constant materials further increase the attenuation. Our challenge is then to find a way to reduce the attenuation while simultaneously keeping the shunt impedance high.

Previous work in the optical regime on the Bragg Fiber (a hollow-core, multilayered, dielectric-lined cylindrical waveguide) has shown that this device is capable of low-loss and high-power transmission. It has found applications in both low-loss communications [64-69] and the high-power laser transmission [70, 71]. Theoretical efforts to apply the Bragg Fiber concept to communications can be traced back to Yeh [64], and more recent works by Xu [68, 69]. Their work provides us with a general method for solving for the modes in a cylindrical waveguide consisting of radially periodic layers of dielectrics. The Bragg Fiber has also been applied to high-power transmitting waveguide for lasers as shown in reference [70] and [71], where the authors have used a transmission line model to calculate the wave attenuation value for certain

guided modes. In all of the above analysis, however, the work was confined to non-accelerating TE or HEM modes.

The idea of using the Bragg Fiber as an optical accelerator (the Optical Bragg Accelerator) has been previously analyzed by Schächter [72] and Mizrahi [73]. Their motivation was to design an all-dielectric accelerator (i.e. one that uses no outer metal jacket) since dielectrics are known to sustain higher electric fields than metals in the optical regime. In the Optical Bragg Accelerator, the dielectric layers are used to create multiple reflections in order to confine the accelerating TM fields without using a metallic outer jacket. In another study, a five zone rectangular DLA structure was studied by Wang et al [74] which used two vacuum layers to reduce the wall losses.

In this chapter, we will extend the Bragg Fiber concept to the microwave regime in order to develop low-loss accelerating structures with high shunt impedance. We call this microwave device the multilayered DLA structure [shown in Figure 4.1]. It has a vacuum channel of radius b_0, surrounded by multiple dielectric layers in a cylindrical metallic waveguide of radius b_N. The dielectric layers serve as multiple reflectors that are used to reduce the magnetic field strength on the copper wall, thus making it possible to reduce the wall losses, and hence, the attenuation. However, instead of trying to achieve total field confinement of the leaky modes with an all dielectric structure (which requires many dielectric layers), here we use the multiple layers to reduce the attenuation to an acceptable level, while total confinement is achieved by the metallic wall. A modal analysis of the multilayered DLA structure is presented in section II along with the general design procedure for obtaining low losses.

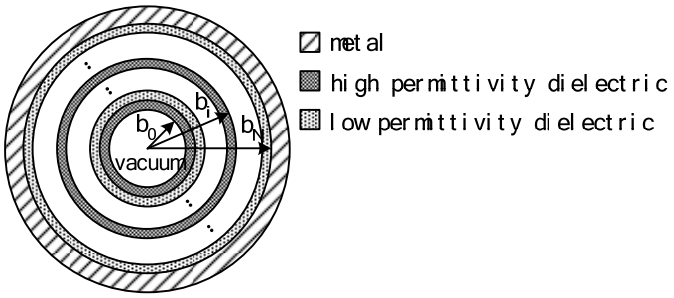

Figure 4.1. Cross-Section of the Multilayered Dielectric-Loaded Accelerating (DLA) Structure.

4.2 Theoretical Analysis

Consider the multilayered DLA structure shown in Fig.1. A hollow vacuum core of radius $r = b_0$ is surrounded by periodic dielectric layers with radius b_i (i =1, 2… N) and alternating permittivity (ε_{low} and ε_{high}), and the outer most dielectric layer is covered by metallic jacket at $r=b_N$. Unlike power transmission applications, here only the properties of the synchronous modes (phase velocity equal to particle velocity, typically close to the speed of light, c) are of interest. For a given RF frequency of accelerator operation, the radius b_i of each layer is determined by the synchronous condition and dielectric constants ε_i. One can optimize the accelerator properties by varying the b_i and ε_i.

Recursive Filed Relations. Modes supported by the multilayered DLA structure are either TM_{0n}, TE_{0n},or HEM_{mn} modes (HE and EH),. The general solutions for the longitudinal component of the electric and magnetic fields for the ith dielectric layer are

$$\begin{aligned} E_{zi}(z,r,\phi) &= [A_i J_m(k_i r) + B_i Y_m(k_i r)] e^{jm\phi} e^{j(\omega t - \beta z)} \\ H_{zi}(z,r,\phi) &= [C_i J_m(k_i r) + D_i Y_m(k_i r)] e^{jm\phi} e^{j(\omega t - \beta z)} \end{aligned} \quad , \tag{4.1}$$

where

$$\begin{aligned} k_i &= \omega \sqrt{\frac{\mu_{ri}\varepsilon_{ri}}{c^2} - \frac{1}{v_p^{\,2}}} \\ \beta^2 &= \omega^2 \mu_0 \varepsilon_0 \mu_{ri} \varepsilon_{ri} - k_i^{\,2} \end{aligned} \quad . \tag{4.2}$$

v_p is the phase velocity of the wave, c is speed of light in vacuum, k_i is the transverse wave number in the ith layer, β is the propagation constant along the z axis, and μ_{ri} and

ε_{ri} are the relative permeability and permittivity for the ith layer respectively. The transverse field components can be derived from the fields given by Equation (4.3)

$$\begin{aligned}
E_{ri} &= \frac{-j}{k_i^{\,2}}(\beta\frac{\partial E_{zi}}{\partial r} + \frac{\omega\mu_i}{r}\frac{\partial H_{zi}}{\partial \phi}) \\
E_{\phi i} &= \frac{-j}{k_i^{\,2}}(\beta\frac{\partial E_{zi}}{\partial \phi} - \omega\mu_i\frac{\partial H_{zi}}{\partial r}) \\
H_{ri} &= \frac{j}{k_i^{\,2}}(\frac{\omega\varepsilon_i}{r}\frac{\partial E_{zi}}{\partial \phi} - \beta\frac{\partial H_{zi}}{\partial r}) \\
H_{\phi i} &= \frac{-j}{k_i^{\,2}}(\omega\varepsilon_i\frac{\partial E_{zi}}{\partial r} + \frac{\beta}{r}\frac{\partial H_{zi}}{\partial \phi})
\end{aligned} \quad . \tag{4.3}$$

In each layer, there are four unknown coefficients A_i, B_i C_i and D_i. By applying the boundary condition at each of the radial boundaries, a 4×4 transfer matrix M*, which stands for the recurrence relation from the ith layer to the (i+1)th layer, is obtained as:

$$\begin{pmatrix} A_{i+1} \\ B_{i+1} \\ C_{i+1} \\ D_{i+1} \end{pmatrix} = M \begin{pmatrix} A_i \\ B_i \\ C_i \\ D_i \end{pmatrix} \qquad , i = 0,...N-1 , \tag{4.4}$$

where, $M = \begin{pmatrix} a_{11} & a_{12} & a_{13} & a_{14} \\ a_{21} & a_{22} & a_{23} & a_{24} \\ a_{31} & a_{32} & a_{33} & a_{34} \\ a_{41} & a_{42} & a_{43} & a_{44} \end{pmatrix}$

---

* Refer to [64], and notice the term of 1/x in Eq.(37) of [64] should be $\frac{k_2}{k_1^{\,2}\rho}$.

$$
\begin{cases}
a_{11} = Y_n^{'}(k_{i+1}r)J_n(k_i r) - \dfrac{k_{i+1}\varepsilon_i}{k_i\varepsilon_{i+1}} Y_n(k_{i+1}r)J_n^{'}(k_i r) \\
a_{12} = Y_n^{'}(k_{i+1}r)Y_n(k_i r) - \dfrac{k_{i+1}\varepsilon_i}{k_i\varepsilon_{i+1}} Y_n(k_{i+1}r)Y_n^{'}(k_i r) \\
a_{13} = \dfrac{\beta}{\omega\varepsilon_{i+1}}\left(\dfrac{1}{k_{i+1}r} - \dfrac{k_{i+1}}{k_i^2 r}\right)J_n(k_i r)Y_n(k_{i+1}r) \\
a_{14} = \dfrac{\beta}{\omega\varepsilon_{i+1}}\left(\dfrac{1}{k_{i+1}r} - \dfrac{k_{i+1}}{k_i^2 r}\right)Y_n(k_i r)Y_n(k_{i+1}r) \\
a_{21} = \dfrac{k_{i+1}\varepsilon_i}{k_i\varepsilon_{i+1}} J_n^{'}(k_i r)J_n(k_{i+1}r) - J_n^{'}(k_{i+1}r)J_n(k_i r) \\
a_{22} = \dfrac{k_{i+1}\varepsilon_i}{k_i\varepsilon_{i+1}} J_n(k_{i+1}r)Y_n^{'}(k_i r) - J_n^{'}(k_{i+1}r)Y_n(k_i r) \\
a_{23} = \dfrac{\beta}{\omega\varepsilon_{i+1}}\left(\dfrac{k_{i+1}}{k_i^2 r} - \dfrac{1}{k_{i+1}r}\right)J_n(k_i r)J_n(k_{i+1}r) \\
a_{24} = \dfrac{\beta}{\omega\varepsilon_{i+1}}\left(\dfrac{k_{i+1}}{k_i^2 r} - \dfrac{1}{k_{i+1}r}\right)J_n(k_i r)Y_n(k_i r) \\
a_{31} = \dfrac{\beta}{\omega\mu_{i+1}}\left(\dfrac{1}{k_{i+1}r} - \dfrac{k_{i+1}}{k_i^2 r}\right)Y_n(k_{i+1}r)J_n(k_i r) \\
a_{32} = \dfrac{\beta}{\omega\mu_{i+1}}\left(\dfrac{1}{k_{i+1}r} - \dfrac{k_{i+1}}{k_i^2 r}\right)Y_n(k_i r)Y_n(k_{i+1}r) \\
a_{33} = J_i(k_i r)Y_i^{'}(k_{i+1}r) - \dfrac{k_{i+1}\mu_i}{k_i\mu_{i+1}} J_n^{'}(k_i r)Y_n(k_{i+1}r) \\
a_{34} = Y_n(k_i r)Y_n^{'}(k_{i+1}r) - \dfrac{k_{i+1}\mu_i}{k_i\mu_{i+1}} Y_n(k_{i+1}r)Y_n^{'}(k_i r) \\
a_{41} = \dfrac{\beta}{\omega\mu_{i+1}}\left(\dfrac{k_{i+1}}{k_i^2 r} - \dfrac{1}{k_{i+1}r}\right)J_n(k_i r)J_n(k_{i+1}r) \\
a_{42} = \dfrac{\beta}{\omega\mu_{i+1}}\left(\dfrac{k_{i+1}}{k_i^2 r} - \dfrac{1}{k_{i+1}r}\right)Y_n(k_i r)J_n(k_{i+1}r) \\
a_{43} = \dfrac{k_{i+1}\mu_i}{k_i\mu_{i+1}} J_n(k_{i+1}r)J_n^{'}(k_i r) - J_n^{'}(k_{i+1}r)J_n(k_i r) \\
a_{44} = \dfrac{k_{i+1}\mu_i}{k_i\mu_{i+1}} J_n(k_{i+1}r)Y_n^{'}(k_i r) - J_n^{'}(k_{i+1}r)Y_n(k_i r)
\end{cases}
.
$$

J_n, Y_n, $J_n^{'}$, $Y_n^{'}$ are the nth order Bessel functions and their derivatives; k_i, *and* k_{i+1} are transverse cutoff wave number in the ith and (i+1)th layer respectively.

At $r=0$ we require that B_0 and D_0 to be zero. We then have (4×N)+2 unknown constants and 4×N equations for the multilayer DLA structure. The additional two equations come from the boundary conditions at inner surface of metallic wall, $Ez(r= b_N) = Hr(r= b_N) = 0$. Now, by applying the recurrence relation (Equation (4.4)), a simplified equation can be derived

$$\begin{pmatrix} A_N \\ B_N \\ C_N \\ D_N \end{pmatrix} = M_{N-1} \cdots M_1 M_0 \begin{pmatrix} A_0 \\ 0 \\ C_0 \\ 0 \end{pmatrix}, \tag{4.5a}$$

with

$$\begin{aligned} &A_N J_m(k_N b_N) + B_N Y_m(k_N b_N) = 0 \\ &C_N J_m'(k_N b_N) + D_N Y_m'(k_N b_N) = 0 \end{aligned}, \tag{4.5b}$$

where M_i, (i=0, 1….N-**1**) is the transfer matrix for the ith boundary, and b_N is radius to the inner surface of metal wall. If we know the electric and magnetic fields in any particular layer, then the unknown coefficients for any other dielectric layer can be calculated through this transfer matrix. The condition for a non-trivial solution to Equation (4.5) will determine the dispersion relation of this waveguide. By normalizing either the initial electric or magnetic field and combining Equation (4.2), the ω-β relation for the different modes can be found. As usual, the modes are represented by the orders of Bessel functions m and different number of roots n. For example, if the order of the Bessel functions m equals zero, then the transfer matrix M_i is reduced to a diagonal block, which represents two categories of degenerate modes---TM_{0n} and TE_{0n}, where the subscript n is the nth of root for Equation (4.5). Otherwise, the hybrid modes HEM_{mn}, with all six field components, are obtained from m>0.

While TE modes are of primary interest in optical transportation applications, we do not consider these modes since they cannot accelerate charged particles. Instead, we will concentrate on the accelerating modes (TM_{0n}) and some of the parasitic modes (HEM_{1n}) since they can be excited by the charged particles.

Optimization Procedure. Before computing the accelerator characteristics of the multilayer DLA structure, we need to find the optimal thickness of each dielectric layer. As stated at the beginning of this paper, the motivation for considering the multilayer DLA structure was to decrease the field attenuation by reducing the magnetic field at the metal wall. Borrowing the optimization procedure for the Bragg fiber [64, 69], we can accomplish this by reducing the fields in the outward direction much faster than in the single-layer dielectric structure. In other words, we can optimize the structure to have much weaker fields at the wall. For the TM_{0n} mode, this optimization criteria is

$$\begin{cases} H_\phi(r=b_i) = E_z'(r=b_i) = 0 & \text{if} \quad k_{i+1} < k_i \\ H_\phi'(r=b_i) = E_z(r=b_i) = 0 & \text{if} \quad k_{i+1} > k_i \end{cases}. \tag{4.6}$$

where the prime represents differentiation in the radial direction. Before optimization, implicit parameters in the transfer matrix M_i, such as frequency, phase velocity and the alternating dielectric constants, should be set. The minimum radius of the vacuum region b_0 is determined by the beam size and is not adjusted during this optimization. Then by replacing the outermost conductor boundary condition in Equation (4.5) with Equation (4.6) and implement Equation (4.6) into the boundary condition of each layer, the radius of boundary b_i can be easily obtained by sequential outward solving of Equation (4.5).

Plots of the longitudinal electric field for several *TM* (Figure 4.2(a)) and *HEM* (Figure 4.2(b)) modes supported in a 4-layer (N=4) dielectric-loaded metallic waveguide. In this example, we set the permittivity for the dielectric layers as 20 and 10, b_0=3mm and the found optimized dimensions as b_1=5.99mm, b_2=8.3mm, b_3=9.8mm, and b_4=12.1mm. The field amplitude of each mode is normalized to its field in the vacuum region when synchronized. For the multilayer DLA structure, the usual operating mode for particle acceleration is no longer the fundamental mode, TM_{01}. In this case, in order to minimize the power losses while maintaining other accelerating properties, the accelerating mode is chosen to be TM_{03}, which has its synchronized frequency at 11.424GHz.

The dispersion curves of several modes for the same structure are shown in Figure 4.3. The synchronous frequency for each mode can be obtained at the intersection point between each curve and the light line. And all important accelerating parameters are calculated using those synchronous frequencies. Figure 4.4 provides another view to see how the field of the accelerating mode TM_{03} is intensely confined inside the vacuum region by Bragg reflecting layers. That means that we can obtain higher Q or lower power loss than that for the other modes. Figure 4.4 also shows that, like single-layer DLA structure, the multilayer DLA structure also has good field confinement for high order hybrid mode HEM_{13} (parasitic mode), which may exert transverse force on off-center particles. However, we can use Chojnacki scheme [35] to damp those parasitic modes effectively. This will be discussed in section 4.4.

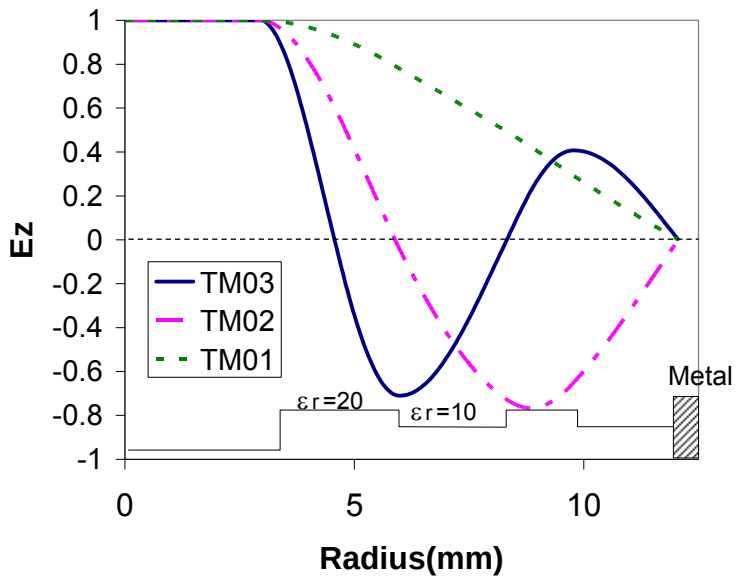

(a) TM Modes.

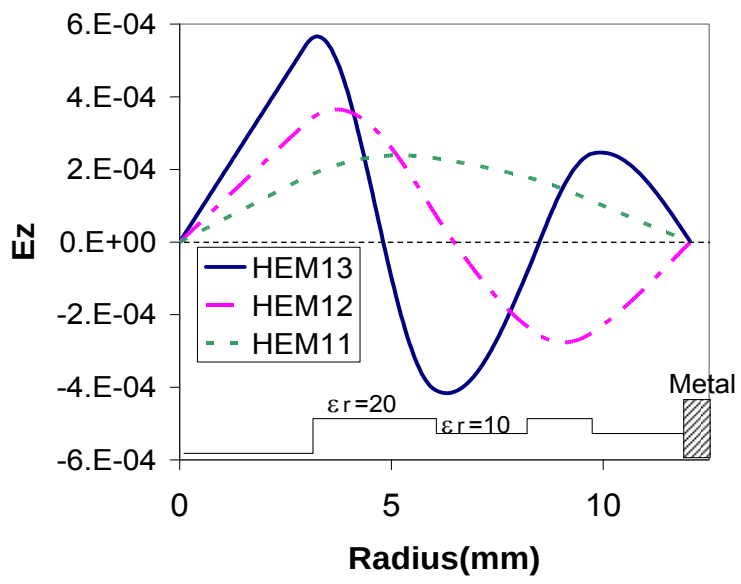

(b) Parasitic modes.

Figure 4.2. Profile of Longitudinal Electric Fields for Several TM Modes and Parasitic Modes Built In a 4-layer Dielectric-Loaded Accelerating Structure.

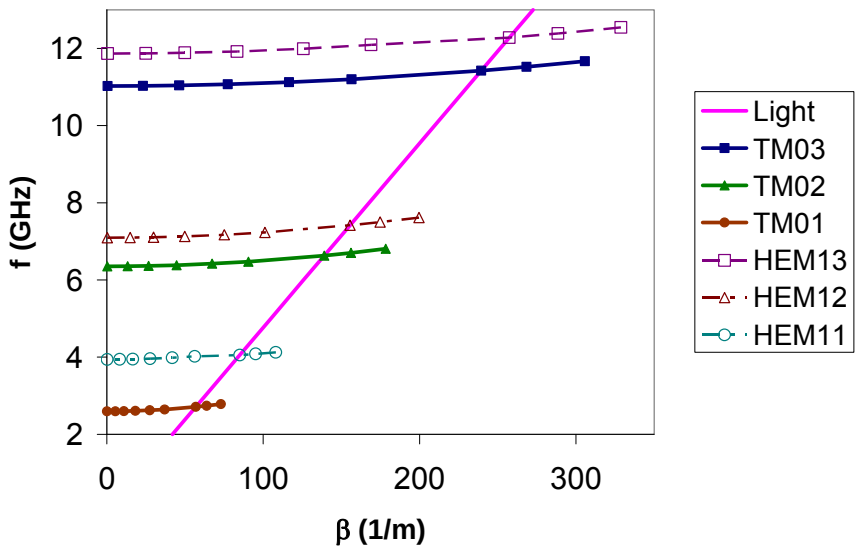

Figure 4.3. Dispersion Relations of Several Low Order Modes in 4-layer Dielectric-Loaded Metallic Cylindrical Waveguide with Same Dimension as Figure 4.2.

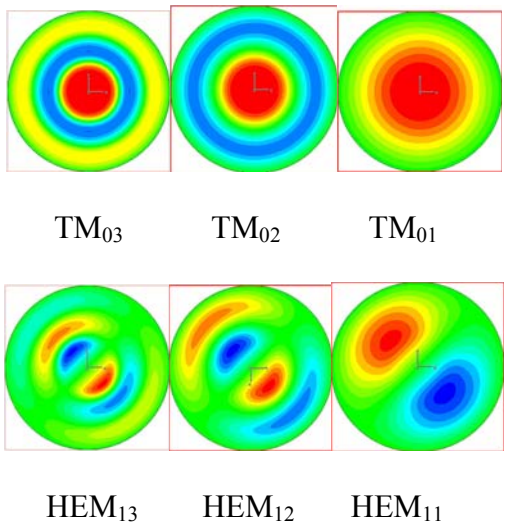

Figure 4.4. Longitudinal Electric Field Distribution of Some Lower Order Modes in Cross-section of the 4-layer Dielectric-Loaded Waveguide Which Has Same Dimensions as Shown in Figure 4.2.

4.3 Design of X-band Four-Layered DLA Structure

In this section, we give an example of an X-band multilayer DLA structure with 4-layers ($N=4$). The first column in Table 1 summarizes the characteristic parameters of this structure. Note that the Quality factor Q is computed based on only the copper wall losses since we assume that an extremely low loss dielectric material may be obtained. These same parameters were also calculated for a single-layer DLA structure in the second column of Table 1. Comparison between the 4-layer and the single-layer structures shows that both r and α_0 have been improved remarkably. Even though r/Q becomes smaller, due to much higher Q, than that of the single-layer DLA structure, the 4-layer structure still has comparable number referring to the all metal structure. More significantly, the shunt impedance has been improved from 25 MΩ/m to 89MΩ/m, which means the particle is accelerated much more efficiently.

After reading the above, the reader may suspect that the improved performance of the multilayered structure is not due to its multiple layers, but rather the choice of the TM_{03} mode as the accelerating mode. To demonstrate that this is not the case, we also calculated the corresponding parameters of the TM_{03} mode for the single-layer structure as shown in the third column of Table 4.1. As usual, the outside radius of single-layer, b_1, was chosen to make the TM_{03} mode synchronous at 11.424 GHz. Table1 shows that r is similar to that of the TM_{01} mode, which means that there is no improvement in the accelerator efficiency, even though Q was noticeably increased. This is because, instead of reduction of the wall loss, the increase in Q was mostly the result of the increase in stored energy per unit length, U, due to the increased volume. But for multilayer DLA structure, due to the suppressed fields as a ratio of the transverse cut-off wave number k_i

Table 4.1. Accelerating Modes RF Parameters Comparison for Different DLA Structures.

	4-layer accelerating mode (TM_{03})	Single-layer accelerating mode (TM_{01})	Single-layer accelerating mode (TM_{03})
Cut-off Freq.(GHz)	11.03	11.1	11.13
Synchronized Freq. (GHz)	11.424	11.424	11.424
Group Velocity (×c)	0.068	0.055	0.051
Q	33476	2865	12551
r (MΩ/m)	89	25.1	25.1
r/Q (Ω/m)	2658	8756	2007
Power Attn (dB/m)	-0.45	-6.6	-1.6

* Geometric parameters for 4-layer DLA structure: radius of each layer is, in sequence, b_0=3mm, b_1=5.99mm, b_2=8.3mm, b_3=9.8mm, b_4=12.1mm; single-layer DLA structure using TM_{01} as accelerating mode: b_0=3mm, b_1=4.567mm; single-layer DLA structure using TM_{03} as accelerating mode: b_0=3mm, b_1=10.57mm (choose different outmost radius is to keep same synchronized frequency for different accelerating mode).

to k_{i+1} in the periodic bragg reflectors (Equation (4.6)), the power dissipated in the copper wall was decreased and therefore the shunt impedance improved dramatically.

In section 4.2 we described the procedure to determine the radius of each dielectric layer except for that of the radius of vacuum core, b_0. While the lower limit of b_0 is set by the beam size, this does not mean that we can choose an arbitrary core size as long as it is above this lower limit. Figure 4.5, Figure 4.6, Figure 4.7 and Figure 4.8 show how b_0 influences each of the four accelerating parameters described above. Basically, increasing b_0 makes r and r/Q worse, but without much of an effect on v_g and α_0. A second factor which has a significant effect on all four parameters is the ratio of dielectric constants, $\varepsilon_{high}/\varepsilon_{low}$, in the alternating dielectric layers. For a given b_0, a large ratio of $\varepsilon_{high}/\varepsilon_{low}$ improves r, r/Q and α_0 but increases v_g significantly. Figure 4.5 to Figure 4.8 shows these effects when b_0 is varied from 2.5 to 5 mm. Lastly, the value of the absolute value of the dielectric constant in both layers should be kept high since the thickness of dielectric layer is related to the guided wave length and a higher dielectric constant makes the radius of whole structure smaller. By inspection of Figure 4.5 to Figure 4.8, we can choose the optimal accelerating features.

4.4 Parasitic Modes Damping

Like the single layer DLA structure, when an off-axis particle travels through the multilayer DLA structure, parasitic, HEM modes will be excited which can impart transverse deflection forces to trailing particles and degrade the beam quality if they are not sufficiently suppressed. In the case of an iris-loaded (metal) accelerating structure, manifolds can be used to damp the parasitic modes. For a DLA structure, we use the

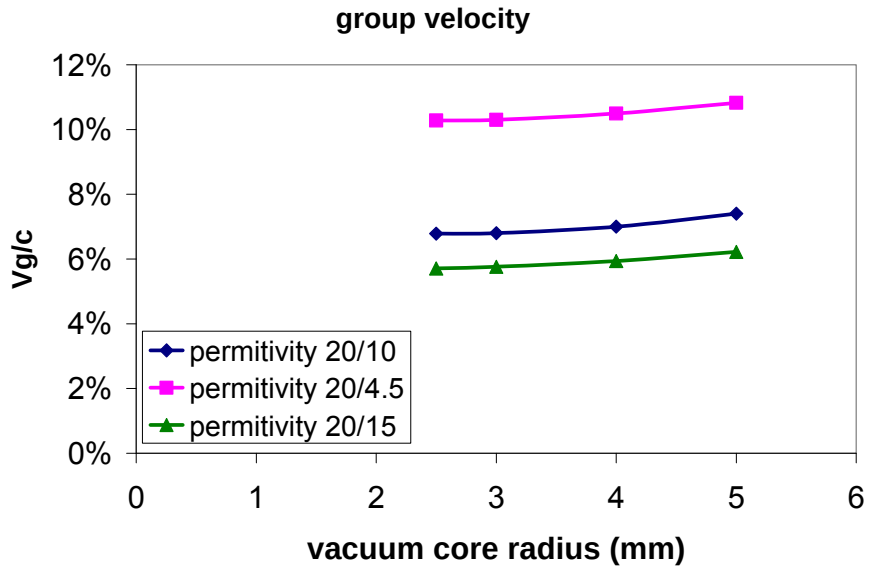

Figure 4.5. Effect of Both Vacuum Core Size and Dielectric Permittivity Ratio on the Group Velocity. Still, This Model is Based on 4-layer Structure.

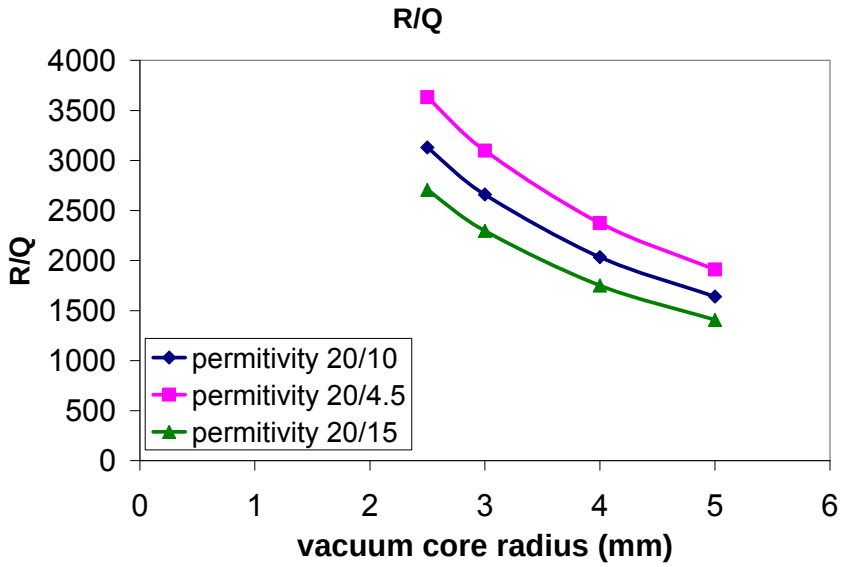

Figure 4.6. Effect of Both Vacuum Core Size and Dielectric Permittivity Ratio on the R/Q. Still, This Model is Based on 4-layer Structure.

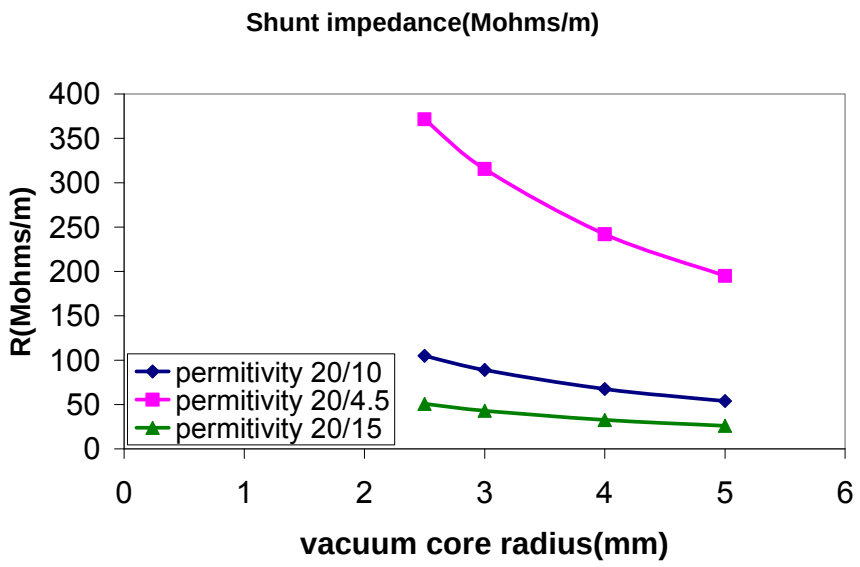

Figure 4.7. Effect of Both Vacuum Core Size and Dielectric Permittivity Ratio on the Shunt Impedance. Still, This Model is Based on 4-layer Structure.

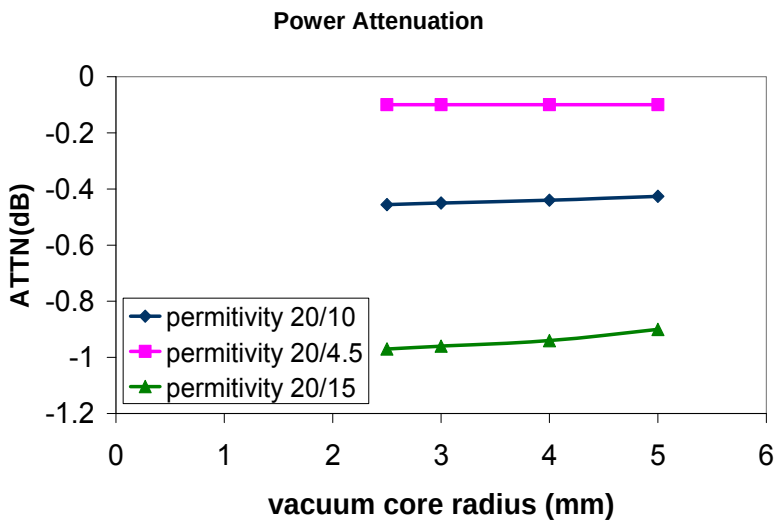

Figure 4.8. Effect of Both Vacuum Core Size and Dielectric Permittivity Ratio on the Power Attenuation. Still, This Model is Based on 4-layer Structure.

method presented in [35] to suppress the HEM modes. This method places segmented conductors around the outside of the outermost dielectric layer. These segmented conductors interrupt the azimuthal surface currents which are needed to support the magnetic component of HEM modes. But for the TM modes which require longitudinal currents, these conductors are still capable of confining the wave and thus have no influence on the TM modes. Therefore, the HEM modes will not be confined within the segmented conductors. If we then surround the segmented conductors with a lossy material, the parasitic modes will be highly attenuated.

The matrix Equation (4.4) is again used to solve for the HEM modes in the multilayer DLA waveguide. Some results for the parasitic modes for the same 4-layer DLA structure example are shown in Table 4.2. The r and r/Q of the parasitic mode is calculated for a particle that is 1mm off-axis (Given in units of MV/m/mm). Note that we use a complex permeability for outside lossy material layer in the parasitic mode damping case. We use the numerical solver to find the complex propagation constants of each mode directly.

A similar damping scheme was undertaken by Chou [75] that demonstrates that, even without a segmented conductor, a thin ferrite film can suppress the HEM modes. In this case, alternative to solve the complex transcendental equations for the multilayer structure, we can apply perturbation theory and achieve acceptable accuracy since the lossy foil is very thin. The complex propagation constant perturbation for a ferrite-loaded-waveguide problem can be expressed as [76]

Table 4.2. Parasitic Modes RF Parameters Comparison for Multilayered and Single Layered DLA Structures.

	4-layer parasitic mode (HEM_{13})	Single-layer parasitic mode (HEM_{11})
Cut-off Freq.(GHz)	11.886	9.2
Synchronized Freq. (GHz)	12.28	9.87
Group Velocity (×c)	0.067	0.06
Q	33638	2623
r (MΩ/m/mm)	2	0.1
r/Q (Ω/m/mm)	60	40
Power Attn (dB/m)	-0.5	-5.7

* Geometric parameters for 4-layer DLA structure: radius of each layer is, in sequence, b_0=3mm, b_1=5.99mm, b_2=8.3mm, b_3=9.8mm, b_4=12.1mm; single-layer DLA structure using TM_{01} as accelerating mode: b_0=3mm, b_1=4.567mm. The r and r/Q of the parasitic mode is calculated for a particle that is 1mm off-axis (Given in units of MV/m/mm).

$$\gamma + \gamma_0^* = \frac{j\omega \int_{\Delta S} (\Delta\varepsilon \vec{E} \cdot \vec{E}_0^* + \Delta\mu \vec{H} \cdot \vec{H}_0^*) dS}{\int_S \vec{\alpha}_Z \cdot (\vec{E} \times \vec{H}_0^* + \vec{E}_0^* \times \vec{H}) dS}, \tag{4.11}$$

where the complex propagation constant is $\gamma=\alpha+j\beta$, in which α represents attenuation constant and β propagation constant. Subscript 0 means the unperturbed electromagnetic fields. If the filling factor (percentage of filling material in whole volume) is very small, less than 3 percent, we can obtain very accurate results.

Some results are shown in Figure 4.6. The ferrite foil used to suppress the HEM modes is 0.2mm thick, with a complex permeability of $\mu=2-j1.5$. The same geometry and electron beam source (1mm off-axis particles) are used for the curves shown in Figure 4.9; the dashed lines are for original waves and the solid lines are for the damped ones.

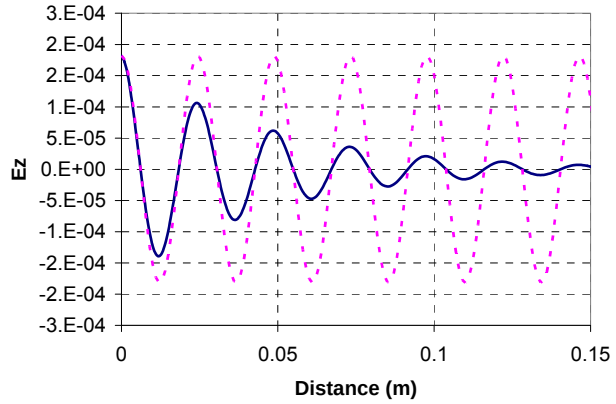

(a) HEM_{13}

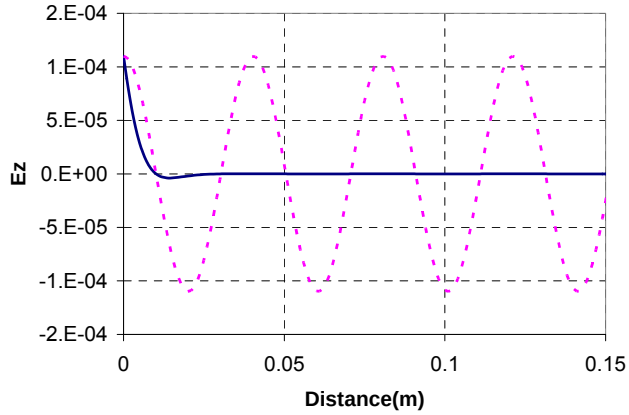

(b) HEM_{12}

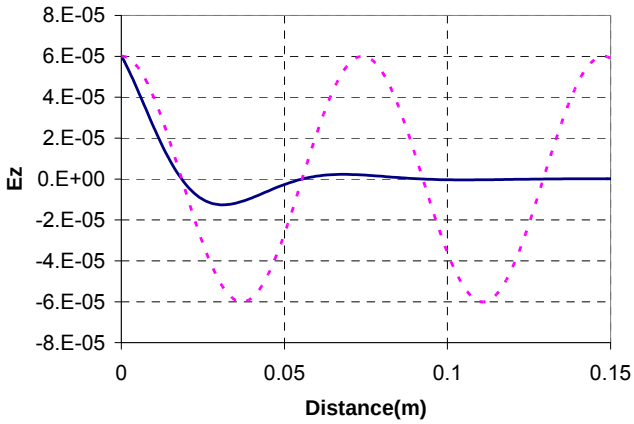

(c) HEM_{11}

Figure 4.9. Parasitic Modes Damping by Thin Ferrite Foil. Dashed Lines Represent Longitudinal Electric Field without Damping and Solid Lines are those After Damping.

CHAPTER 5

CONCLUSIONS

As one of major research programs on the regime of Advanced Accelerator Concepts (AAC), dielectric-loaded accelerator has been developed for near twenty years at Argonne National Laboratory (ANL). Quite a few milestones have been reached since the construction of Advanced Accelerator Test Facility (AATF). Later on, Argonne Wakefield Accelerator (AWA) at ANL was built. Besides the main aspects of the theoretical studies of the dielectric-loaded waveguide as particle acceleration, which is summarized in the Chapter 2, most recently, we have accomplished a series of high power RF testing on the external RF powered X-band DLA structures in the Naval Research Laboratory/ ANL joint program.

The most attracting feature of the dielectric-loaded accelerating structure relative to the entirely metal structure is its potentially high surface breakdown voltage. Therefore, a major purpose of high power RF tests is to investigate this point. So far, several experiments have been carried out for two different dielectric materials based DLA structures, alumina and $Mg_xCa_{1-x}TiO_3$ at NRL where the Magnicon can provide up to 12MW, 200ns pulsed RF at frequency 11.424GHz.

The DLA structure used in the high power RF experiment is a modular traveling wave structure which consists of three separate functional parts: input/output RF coupler, input/output impedance matching section, and central acceleration section. One of the big advantages of this modular design is that, unlike the prior design, the coupling slot of the metal RF coupler is far away from the loaded dielectric materials so that it effectively eliminates the RF breakdown at that location. Another advantage is that RF coupler can

be reused for different dielectric material based DLA structures. Therefore, the experimental cycles are dramatically increased. Besides, the RF simulation of the structure design can be finished individually, cutting down the requirement of computer's capability.

For the high power RF testing of alumina based DLA structure, the accelerating gradient at the upstream end has reached 8MV/m without dielectric breakdown. During the experiment, we were first to ever observed the multipactor in the partially dielectric-loaded waveguide while the high power RF applied. It occurs with a stimulated light and a large amount of RF power absorption. A simple model based on the secondary electron emission on the inner surface of the alumina tube has successfully demonstrated this phenomenon. Although, the multipactor is an unexpected issue for the application of the DLA structure, we have started to investigate various suppression methods. Experiments on TiN coated DLA structure have demonstrated that it can make the predicted saturation of the multipactoring process in advance. We expect that both the coating thickness and evenness play important roles in the multipactor suppression. In addition, we studied certain influence of the external magnetic field on the multipactor of the alumina based DLA structure as well.

On high power testing of the $Mg_xCa_{1-x}TiO_3$ based DLA structure, the accelerating gradient has reached 5.7MV/m without any dielectric breakdown. During the experiment, we observed apparently less multipactoring process than that for the alumina DLA structure. However, when the accelerating gradient inside the tube is greater than 5.7MV/m, we observed for the first time dielectric breakdown occurred at the dielectric joint where a strong local field enhancement is expected due to the micro-scale vacuum

gap in between. The local electric field at the breakdown point is estimated to be around 80~100MV/m. Because of the electric field pattern of the accelerating mode this joint breakdown indirectly demonstrated the accelerating gradient may be able to reach 80MV/m without breakdown for the uniform dielectric tube. Some dielectric bonding techniques have been investigated. An epoxy gap filling experiment was carried out.

In addition, we proposed a new multilayered DLA structure design to reduce the large RF power attenuation in the single layered DLA structure, meanwhile, improve its shunt impedance. RF power loss in the single layered DLA structure is mainly due to the surface current induced from the strong magnetic field on the metal wall. Proper designed multilayered dielectrics can confine the most EM energy inside the vacuum area; therefore, reducing the surface current on the metal wall. Initial theoretical study has been presented in Chapter 4.

Accurate three dimension model of the multipactor in the DLA structure has not been built up. Physical mechanism of the dielectric joint breakdown also has not been totally understood. Both of them are very important factors to the application of the DLA structure, but beyond the scope of our discussion in the thesis. Various techniques to suppress, even eliminate, the multipactor and local field enhancement need to be extensively studied in the future.

Over-mode propagation is a problem for the multilayered dielectric-loaded accelerating structure. Because the accelerating mode is no longer chosen to be the lowest order TM mode, a highly efficient mode-selective RF coupler becomes a challenge in the multilayered DLA structure design. Otherwise, mode conversion may cause strong energy loss in the wave propagation. These aspects have not been discussed in the thesis.

Beam experiment is the final stage for the DLA structures. A NRL/ANL joint research program---building a compact dielectric-loaded accelerator will provide a ideal platform to test various dielectric material based DLA structures. Those experiments are expected to lead to the discovery of new phenomena, study and answer more fundamental questions in near future.

During the process of discovering, studying and solving technical issues, we have no doubt that further progress will be made on the way to build applicable dielectric-loaded accelerators.

APPENDIX A

RESONANT LOOP TECHNIQUE

Perturbation method presented in Chapter 3 for finding the profile of the electric field inside the structure are based on passive technique, in which the microwave source and the cavity are independent of each other. In contrast, another approach is active frequency technique in which a microwave oscillation loop with the under tested cavity is involved. This method is commonly used to measure the permittivity of samples of dielectric [77, 78], and it can be applied to do cavity perturbation experiment as well [79]. In our work, we will investigate the theory behind of this active perturbation method, and apply this technique to obtain the accelerating field of a cavity by beadpull experiment.

An active oscillation loop consisting of amplifier, phase shifter, power limiter, directional coupler and a cavity with dielectric perturber inside is shown in Figure A1.

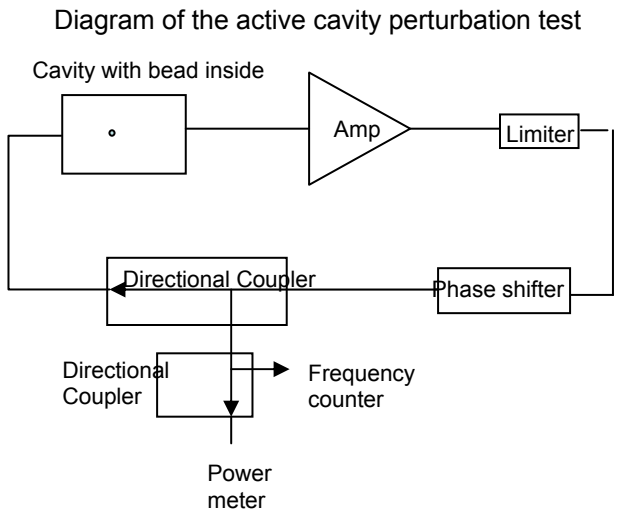

Figure A1. Diagram of the Active Bead-pull System.

The block diagram illustrates the oscillation constraint should be given by phase and gain equations as phase $\Phi=2N\pi$ and gain G=1. In [78] the authors re-examined the validity of this condition and proved that it is valid only in the special case when either loop s-parameters $S_{11}=S_{21}=0$ or $S_{22}=S_{12}=0$. The loop frequency under the oscillation condition mentioned above will shift provided that external perturbation is applied to cavity in the loop [53].

The tested cavity is a simple L-Band cylindrical pillbox with a central hole to pass the beam. The accelerating mode is TM01 mode for obtaining a constant accelerating gradient. The feed-in coupling of the cavity uses magnetic field by a small coupling loop on the side wall of the cavity, and an electric dipole installed nearby the center of the top cover of the cavity is used to couple the signal out. This will let TM01 mode to be excited based on the pattern of TM01 mode. The EM fields of the cavity are simulated by Microwave Studio® and shown in Figure A2. The coupling loop at the sidewall can excite all TM modes but only the TM01 mode can be most easily picked up by the electric probe near the center of the cavity, where the strongest electric field exsits.

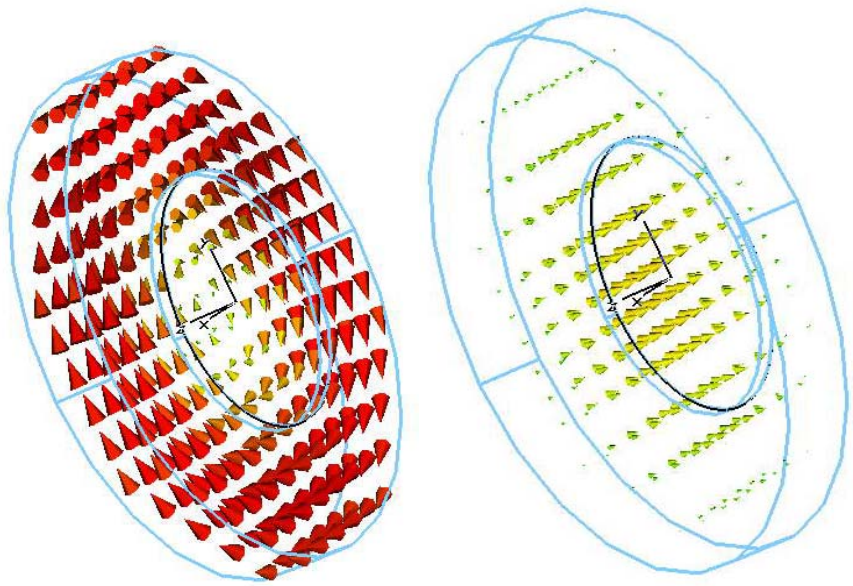

Magnetic field Electric field

Figure A2. EM Field of the TM01 Mode in the L-Band Cavity.

In the experiment, we first accomplished a linear phase scan to obtain the accurate cavity frequency without the perturber. Figure A3 shows the frequency and amplitude responses of the constructed resonant loop while changing the length of the delay line (phase shifter) in the loop. The solid lines (calculated the cavity characteristics) are obtained by the following equations:

$$|T(\omega)| = \frac{T(\omega_0)}{\left[1 + 4Q_L^2\left(\frac{\omega - \omega_0}{\omega}\right)^2\right]^{\frac{1}{2}}} \tag{A.1}$$

$$\phi(\omega) = -\arctan\left[2Q_L\left(\frac{\omega - \omega_0}{\omega}\right)\right] \tag{A.2}$$

where, the T(ω) and ϕ(ω) are the amplitude and the phase of the transmission characteristics for the cavity. Q_L is the loaded the quality factor of the cavity, and ω_0 is the resonant frequency. The resonant frequency at the top the bell curve is 1.1847GHz. As shown in the plot, the transmission characteristic of the cavity is slightly different from that of the loop when the loop oscillates out of range of the cavity resonant frequency. This is due to the effects of loop components, like amplifier, transmission line, and power limiter, etc.

Once the cavity resonant frequency is obtained, we can use perturber, a dielectric bead, to detect the electric field profile at the center of the cavity by recording the frequency variance when moving the bead (refer to equation (3.1)). During the experiment, we use a computer controlled step-motor to accurately move the bead along the axis of the cavity. The frequency change is recorded simultaneously by a frequency counter. The Figure A4 plots the electric field obtained from the bead-pull experiment.

The circuit loop oscillates at the frequency of the TM01 mode, therefore, the constant electric field at the center is expected by the theory.

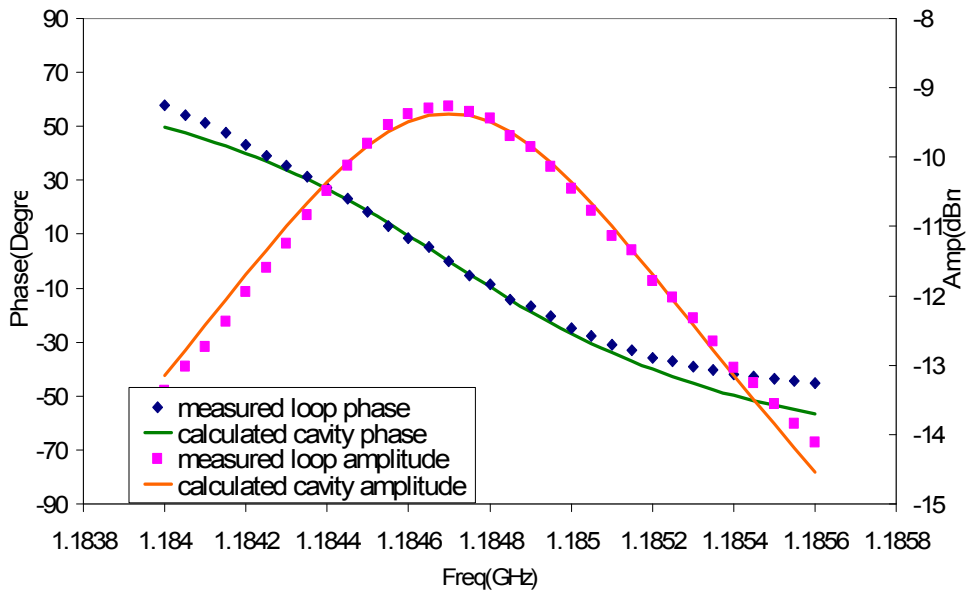

Figure A3. The Phase and Amplitude Responses of the Resonant Loop by the Phase Scan.

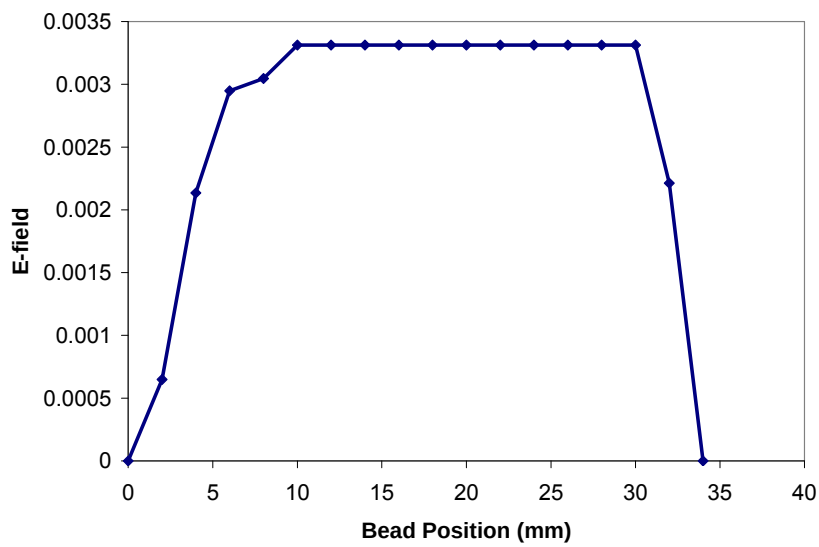

Figure A4. Electric Field at the Center of the Cavity by Beadpull Experiment.

APPENDIX B

DIRECT WAKEFIELD MEASUREMENT

Witness beam technique has been successfully used in the wakefield measurement at the AWA facility [23]. Here we present a method to measure wakefield directly by a simple RF circuit and data post-processing without using witness beam. Single electron bunch is launched and a heterodyne receiver circuit is employed to measure coupled out wakefields in a fast oscilloscope in which local oscillation is from the frequency doubler because the Ku band RF source is unavailable. The signal is supposed to be around 5GHz after demodulation. We have accomplished an experiment of use this technique to measure the wakefield of a 15.6GHz standing wave DLA structure at the AWA beamline on Dec. 2004.

Experiment Setup Limited by the availability of the 15GHz oscilloscope, we cannot observe the high frequency wakefield signal in time domain directly. Therefore, the basic idea of the wakefield RF measurement technique is to down-covert the high frequency wakefield to a certain low frequency then restore it by the data processing. However, due to the wakefield signal of the tested 15.6GHz DLA structure is a very short (ns scale) RF pulse there exists a frequency down-conversion limit to acquire the full wakefield information. The block diagram of the experiment configuration is shown in Figure B1. The hardware enclosed in the left box consists of 1) a probe antenna which is located in the coupling slot of the 15.6GHz DLA structure under test with a coupling coefficient of ~ -60dB; 2) a broadband mixer to down convert the wakefield signal, which has a major frequency component of 15.6GHz, to 5.2GHz; 3) a local oscillator circuit provides 10.4GHz RF signal; 4) a loss pass filter with cutoff frequency of 5.3GHz to block the high frequency interference; 5) a Lecory 6GHz oscilloscope operated at the sampling rate of 20Gs/s. The down-converted wakefield signal is sampled by the digital scope and export to the software post-processor enclosed in the right box in the Figure 1 which has an inverse function of the hardware subsystem to restore the real 15.6GHz wakefield signal. The signal flow in the post- processor is shown as follows: the digitized down-converted wakefield signal is firstly interpolated to raise the sampling rate up to 80Gs/s that is to match the sampling rate of the 10.4GHz digital local oscillator; then these two signals are mixed up in a multiplicator; the final step is to use a digital high pass filter to block the low frequency interference from the signal multiplication. All data processing is finished in MATLAB® environment.

Experimental Data The tested 15.6GHz standing wave DLA structure has parameters of the inner radius a=5mm, outer radius b=7.49mm, length l= 101.6 mm, and dielectric constant ε=4. The electron bunch launched in the experiment is around 1 nC, and the excited wakefield is expected up to have peak power of 400kW in the theoretical model. During the experiment, we first used a fast response diode to detect the wakefield signal from the probe antenna. A few ns wakefield pulse obtained from the crystal detector is shown in Figure B2. Figure B3 shows a typical waveform and power spectrum of the down-converted wakefield signal exported from the digital scope at the sampling rate of 20Gs/s. It is noticed that, unlike we expect, the major wakefield component appears at around 3.4GHz instead of 5.2GHz. A plausible explanation is due to the dielectric constant variance of the loaded ceramic material.

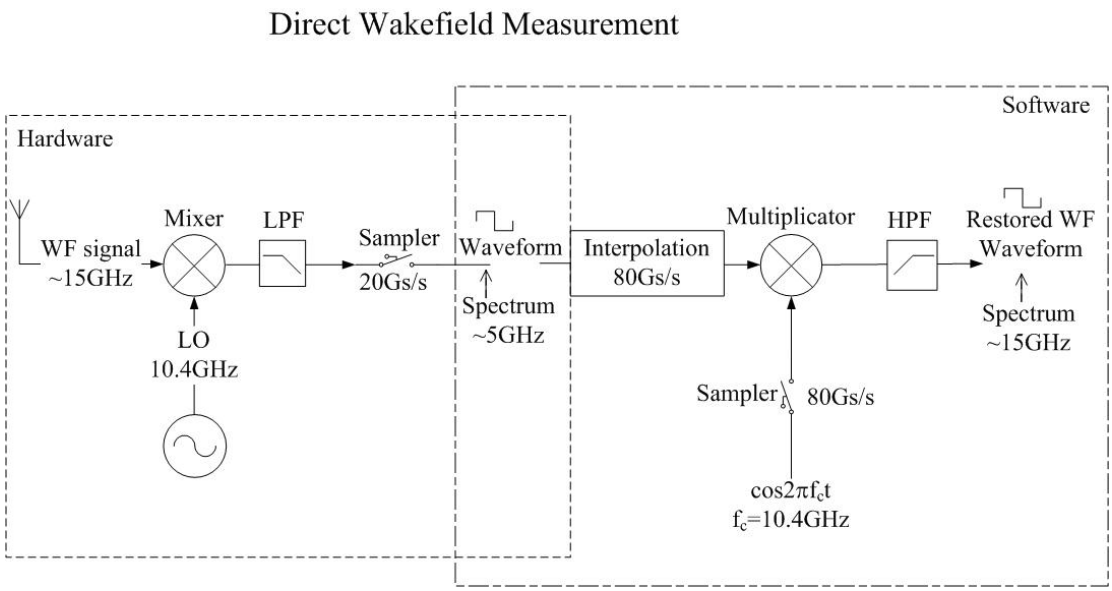

Figure B1. Block Diagram of Wakefield RF Measurement Technique.

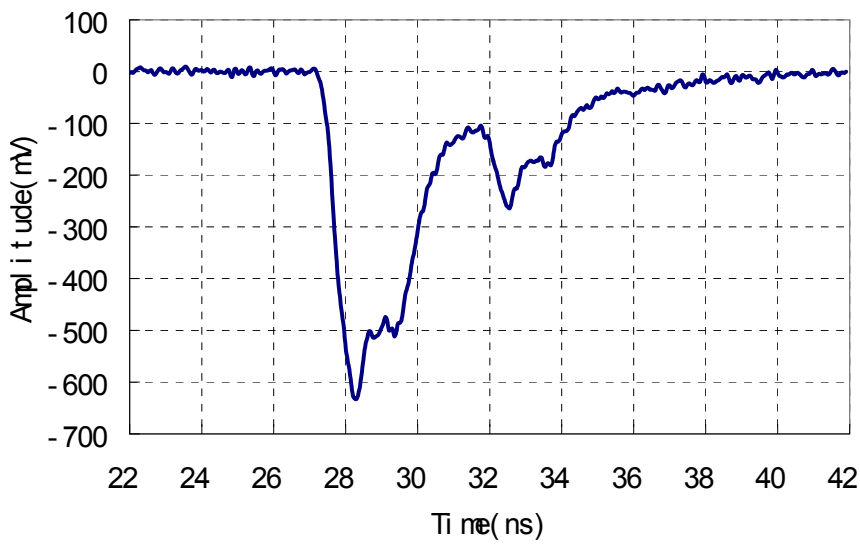

Figure B2. Wakefield Signal Detected by a Fast Response Diode. The Charge is around 1nC.

The up-converted wakefield signal is a double side band signal. Through a designed 64 section FIR high pass filter with the cutoff frequency of 10GHz, the wakefield signal is restored. Figure B4 shows the restored wakefield signal and its spectrum. The wakefield signal has major frequency component at 10.4GHz + 3.4GHz = 13.8GHz.

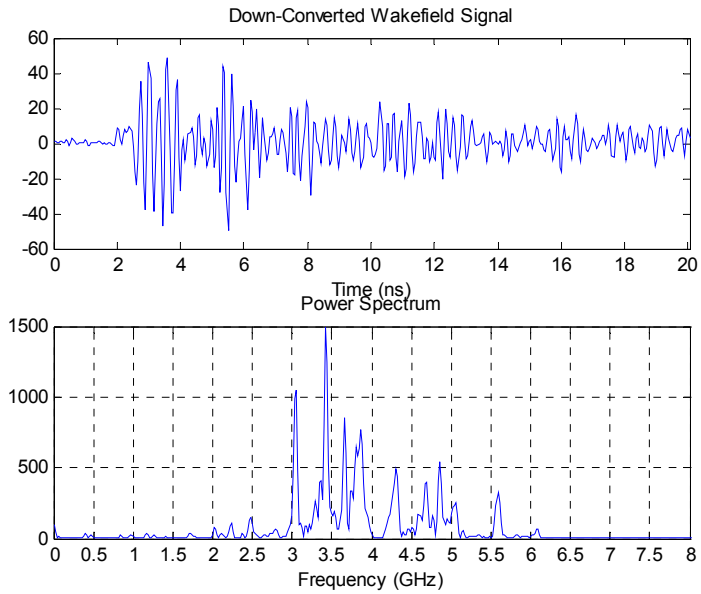

Figure B3. Down Converted Wakefield Signal with the Major Frequency Shown at 3.4GHz.

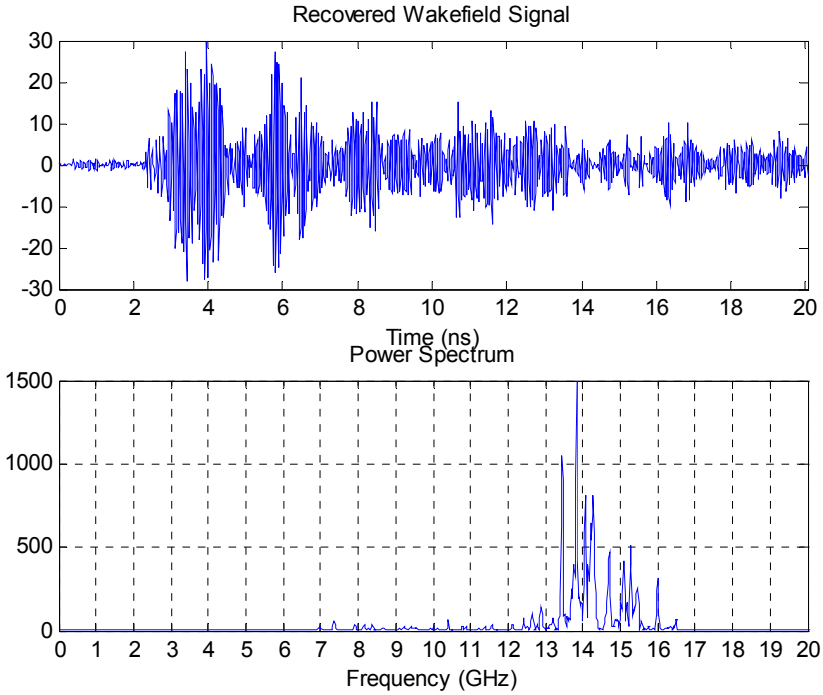

Figure B4. Restored Wakefield Signal.

Discussion of Wakefield Frequency Variance Although the frequency of the measured wakefield signal varied shot by shot because of the instability of the electron bunches, there always exists a greater than 1GHz frequency difference compared to the simulation results for the major frequency component of the wakefield. A most likely reason is the

dielectric constant of the ceramic loaded in the tested DLA structure is far from 4. Figure B5 shows the dependence of the synchronized frequency of TM01mode, a dominant mode in the wakefield signal, on the variance of dielectric constant. This can be verified once the DLA structure took apart from the beamline.

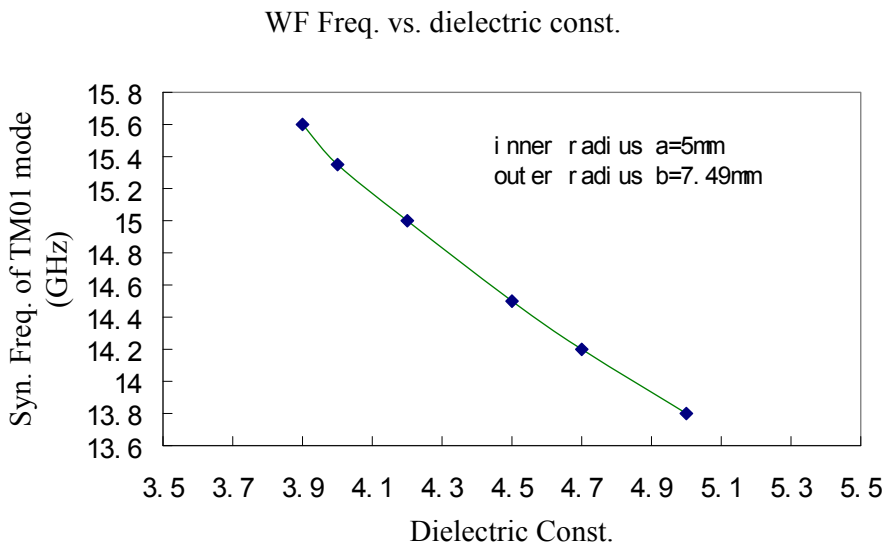

Figure B5. Synchronized Frequency of TM_{01} Mode vs. Dielectric Constant of the Loaded Ceramic tube.

BIBLIOGRAPHY

[1] Katsouleas, T., "Overview of Plasma Accelerators." *Proceedings of Advanced Accelerator Concepts 8th Workshop*, AIP Conference Proceedings. 472 Baltimore, (1998): 19-26.

[2] Assmann, R., P. Chen, F.J. Decker, R. Iverson, P. Raimondi, T. Raubenheimer, S. Rokni, R. Siemann, D. Walz, D. Whittum, S. Chattopadhyayb, W. Leemansb, T. Katsouleasc, S. Leec, C. Claytond, C. Joshid, K. Marshd, W. Morid, and G. Wang, "Proposal for a One GeV Plasma Wakefield Acceleration Experiment at SLAC." *Nuclear Instruments and Methods in Physics Research Section A: Accelerators, Spectrometers, Detectors and Associated Equipment* 410.3 (June 1998): 396-406.

[3] Plettner, T., J.E. Spencer, Y.C. Huang, R.L. Byer, R.H. Seimann, and T.I. Smith, "The Laser Driven Particle Accelerator Project: Theory and Experiment." *Proceedings of Advanced Accelerator Concepts 8th Workshop*, AIP Conference Proceedings. 472 Baltimore, (1998): 118-27.

[4] Fisher, A., J. Gallardo, A.V. Steenbergen, and J. Sandweiss, "IFEL Accelerator Development." *Nuclear Instruments and Methods in Physics Research Section A: Accelerators, Spectrometers, Detectors and Associated Equipment* 341 (March 1994): ABS111,

[5] Schoessow, P., "High Gradient Dielectric Wakefield Device Measurements at the Argonne Wakefield Accelerator." *Proceedings of 1997 Particle Accelerator Conference*, Vancouver, (May 1997): 639-41.

[6] Fang, J., T.C. Marshall, J.L. Hirshfield, M.A. Lapointe, T.B. Zhang, and X.J. Wang, "An Experimental Test of the Theory of the Stimulated Dielectric Wakefield Accelerator." *Proceedings of 1997 Particle Accelerator Conference*, New York, (1999): 3627-30.

[7] Zou, P., W. Gai, R. Konecny, X. Sun, T. Wong, and A. Kanareykin, "Construction and Testing of an 11.4GHz Dielectric Structure Based Traveling Wave Accelerator." *Review of Scientific Instruments* 71.6 (2000): 2301-04.

[8] Yakimenko, V., M. Babzien, I. Ben-Zvi, K. Kusche, I. Progorelsky, X.J. Wang, D. Cline, and F. Zhou, "Parameter Optimizations for Vacuum Laser Acceleration at ATF/BNL." *Proceedings of 2001 Particle Accelerator Conference*, Chicago, IL (June 2001): 111-13.

[9] Mizrahi, A. and L. Schachter. "Optical Bragg Accelerator." *Physical Review E* 70. (2004): 016505.

[10] Kroll, N., S. Schultz, D.R. Smith, and D.C. Vier, "Photonic Band Gap Accelerator Cavity Design at 90GHz." *Proceedings of the Particle Accelerator Conference,* Chicago, (1999): 830.

[11] Joshi, C., "Review of Beam Driven Plasma Wakefield Accelerators," *Proceedings of Advanced Accelerator Concepts 11th Workshop*, AIP Conference Proceedings. 737 New York, (June 2004): 2-10.

[12] Thompson, M.C., J.B. Rosenzweig, G. Travish, N. Barov, H. Edwards, P. Piot, J. Santucci, and R. Tikhoplav, "Status of the UCLA/NICADD Plasma Density Transition Trapping Experiment." *Proceedings of Advanced Accelerator Concepts 11th Workshop*, AIP Conference Proceedings. 737 New York, (June 2004): 440-46.

[13] Muggli, P., B.E. Blue, C.E. Clayton, S. Deng, F.J. Decker, M.J. Hogan, C. Huang, R. Iverson, C. Joshi, T.C. Katsouleas, S. Lee, W. Lu, K.A. Marsh, W.B. Mori, C.L. O'Connell, P. Raimondi, R. Siemann, and D. Walz, "Meter-Scale Plasma-Wakefield Accelerator Driven by a Matched Electron Beam." *Physical Review Letters* 93.1. (July 2004):014802.

[14] Muggli, P., M.J. Hogan, B.E. Blue, C. O'Connell, R.H. Siemann, D. Walz, R. Assmann, C.E. Clayton, F.J. Decker, E.S. Dodd, R.H. Iverson, C. Joshi, T.C. Katsouleas, S. Lee, K.A. Marsh, W.B. Mori, P. Raimondi, and S. Wang, "Status of the Plasma Wakefield Acceleration Experiment at the Stanford Linear Accelerator Center." *Proceedings of 2001 Particle Accelerator Conference*, Chicago IL, (June, 2001):122-25.

[15] Leemans, W.P., P. Volfbeyn, K.Z. Guo, S. Chattopadhyay, C.B. Schroeder, B.A. Shadwick, P.B. Lee, J.S. Wurtele, and E. Esarey, "Laser-driven plasma-based accelerators: Wakefield excitation, channel guiding, and laser triggered particle injection." *Physics of Plasmas* 5.5 (May, 1998):1615-23.

[16] Malka, V., S. Fritzler, E. Lefebvre, M.-M. Aleonard, F. Burgy, J.-P. Chambaret, J.-F. Chemin, K. Krushelnick, G. Malka, S.P.D. Mangles, Z. Najmudin, M. Pittman, J.-P. Rousseau, J.-N. Scheurer, B. Walton, and A.E. Dangor, "Electron Acceleration by a Wake Field Forced by an Intense Ultrashort Laser Pulse." *Science* (Nov 22 2002):1596-1600.

[17] Esarey, E., S. Tochitsky, H.M. Milchberg, and C.B. Schroeder, "Summary Report of Working Group: Laser-Plasma Acceleratio." *Proceedings of Advanced Accelerator Concepts 11th Workshop*, AIP Conference Proceedings. 737 New York, (2004):223-30.

[18] Courant, E.D., C. Pellegrini, and W. Zakowicz, , "High-energy inverse free-electron-laser accelerator." *Physical Review A* 32 (1985):2813-23.

[19] Kimura, W.D., A. Steenbergen, M. Babzien, I. Ben-Zvi, L.P. Campbell, C.E. Dilley, D.B. Cline, J.C. Gallardo, S.C. Gottschalk, P. He, K.P. Kusche, Y. Liu, R.H. Pantell, I.V. Progorelsky, D.C. Quimby, J. Skaritka, L.C. Steinhauer, and V. Yakimenko, "First Staging of Two Laser Accelerator." *Physical Review Letters* 86 (2001):4041-43.

[20] Flesher, G., and G. Cohn. "Dielectric Loading for Waveguide Linear Accelerators." *AIEE Transactions* 70 (1951):887-93.

[21] Zhang, B., "Microwave Inverse Cerenkov Accelerator." *Proceedings of 7th Advanced Accelerator Concepts Workshop*, AIP Proceedings 398 (1996)

[22] Gai, W., R. Konecny, and J. Simpson, "Externally Powered Dielectric Loaded Waveguides as Accelerating Structures." *Proceedings of 1997 Particle Accelerator Conference,* Vancouver, (1997):636-38.

[23] Gai, W., P. Schoessow, B.Cole, , R. Konecny, J. Norem, J. Rosenzweig, and J. Simpson, "Experimental Demonstration of Wakefield Effects in Dielectric Strucures." *Physical Review Letters* 61 (1988):2756.

[24] Schoessow, P., M.E. Conde, W. Gai, R. Konecny, J. Power, and J. Simpson, "High Power RF Generation by Relativistic Beams in Dielectric Structures." *Journal of Applied Physics* 84 (1998):663.

[25] Tremaine, A., J. Rosenzweig, and P. Schoessow, "Electromagnetic Wake-fields and Beam Stability in Slab-symmetric Dielectric Structures." *Physical Review E* 56 (1997):7204.

[26] Zhan, T-B., J. Hirshfield, T. Marshall, and B. Hafizi, "Stimulated dielectric wake-field accelerator." *Physical Review E* 56 (1997):4647-55.

[27] Gai, W., "Performance of the Argonne Wakefield Accelerator Facility and Initial Experimental Results." *Proceedings of 7th Advanced Accelerator Concepts Workshop*, AIP Proceedings. 398 (1996).

[28] Gold, S.H., A.K. Kinkead, O.A. Nezhevenko, V.P. Yakovlev, J.L. Hirshfield, A.L. Vikharev, O.A. Ivanov, S.V. Kuzikov, A.M. Gorbachev, V.A. Isaev, W. Gai, R. Konecny, and J.G. Power, "High Power Accelerator R&D at the NRL 11.424GHz Magnicon Facility." *Proceedings of 10th Advanced Accelerator Concepts*, AIP Conference Proceedings. 647 Mandalay Beach, CA, (June 2002):439-47.

[29] Yu, D., D. Newsham, and A. Smirnov, "21GHz Ceramic RF Power Extractor." *Proceedings of 10th Advanced Accelerator Concepts*, AIP Conference Proceedings. 647 Mandalay Beach, CA, (June 2002):484-505.

[30] Zhang, T-B., T.C. Marshall, and J.L. Hirshfield, "A Cerenkov Source of High Power Picosecond Pulsed Microwaves." IEEE *Transactions on Plasma Science* 26 (June 1998): 787-93.

[31] Hill, M.E., C. Adolphsen, W. Baumgartner, R.S. Callin, X.E. Lin, M. Seidel, T. Slaton, and D.H. Whittum, "High-Gradient Millimeter-Wave Accelerator on a Planar Dielectric Substrate." *Physical Review Letters* 87 (August 2001): 094801.

[32] Jing, C., R. Konecny, W. Gai, S.H. Gold, J.G. Power, A.K. Kinkead, and W. Liu, "High Power rf Test on X-band $Mg_xCa_{1-x}TiO_3$ Based Dielectric-Loaded Accelerating Structure." *Proceedings of Advanced Accelerator Concepts 11th Workshop*, AIP Conference Proceedings. 737 New York, (2004): 258-64.

[33] Power, J.G., W. Gai, and P. Schoessow, "Wakefield Excitation in Multimode Structures by a Train of Electron Bunches." *Physical Review E* 60.5 (1999): 6061-67.

[34] Gai, W., M.E. Conde, R. Konecny, J.G. Power, P. Schoessow, X. Sun, and P. Zou, "Experimental Demonstration of Dielectric Structure Based Two Beam Acceleration." *Proceedings of 9th Advanced Accelerator Concepts* (June 2000): 287-93.

[35] Gai, W. and C-H. Ho. "Modeling of the Transverse Mode Suppressor for Dielectric Wake-field Accelerator." *Journal of Applied Physics* 70 (October 1991):3955-57.

[36] Power, J.G., W. Gai, M.E. Conde, W.M. Liu, H.T. Wang, and Z.M. Yusof, "Transverse beam envelope measurements and the limitations of the 3-screen emittance method for space-charge dominated beams." *Nuclear Instruments and Methods in Physics Research Section A: Accelerators, Spectrometers, Detectors and Associated Equipment* (2005) To be published.

[37] Yusof, Z.M., M.E. Conde, and W. Gai, "Schottky-Enabled Photoemission in a rf Accelerator Photoinjector: Possible Generation of Ultralow Transverse Thermal-Emittance Electron Beam." *Physical Review Letters* 93 (2004): 114801.

[38] Conde, M.E., W. Gai, C. Jing, R. Konecny, W. Liu, J.G. Power, H. Wang, and Z. Yusof, "A New High Intensity Electron Beam for Wakefield Acceleration Studies." *Proceedings of 2003 Particle Accelerator Conference*, Oregon, (2003):2032-34.

[39] Power, J., W Gai, C. Jing, R. Konecny, S.H. Gold, and A.K. Kinkead, "High Power Testing of ANL X-band Dielectric Loaded Accelerating Structures." *Proceedings of Advanced Accelerator Concepts 2002*, AIP Conference Proceedings. 647 Oxnard, (June 2002): 556-64.

[40] Liu, W.M. and W. Gai. "Design of Dielectric Accelerator using TE-TM Mode Converter." *Proceedings of Advanced Accelerator Concepts 2002*, AIP Conference Proceedings. 647 Oxnard, (June 2002): 469-75.

[41] Gold, S.H., A.W. Fliflet, A.K. Kinkead, B. Hafizi, O.A. Nezhevenko, V.P. Yakovlev, J.L. Hirshfield, R. True, and R.J. Hansen, "X-Band Magnicon Amplifier for the Next Linear Collider." *Proceedings of 1997 Particle Accelerator Conference,* Vancouver, (1997): 3153-55.

[42] Zou, P., "X-Band Dielectric Loaded RF Driven Accelerator Structures: Theoretical and Experimental Investigations." PhD Dissertation, Illinois Institute of Technology, 2001.

[43] Panofsky, W.K.H. and W.A. Wenzel. "Some Considerations Concerning the Transverse Deflection of Charged Particles in Radio-Frequency Fields." *Review of Scientific Instruments* 27 (1956): 967.

[44] Ng, K.-Y., "Wake Fields in a Dielectric-lined Waveguide." *Physical Review D* (1990):1891-28.

[45] Rosing, M., and W. Gai. "Longitudinal- and Transverse-wake-field Effects in Dielectric Structures." *Physical Review D* (1990):1829-34.

[46] Wangler, T.P. *RF Linear Accelerators,* John Wiley & Sons, Inc., Chapter 11, pp.314-353, 1998.

[47] Wangler, T.P. *RF Linear Accelerators,* John Wiley & Sons, Inc., Chapter 11, pp.57-86, 1998.

[48] Braun, H.H., CERN-CLIC-Note 364, (1998): 150-58, unpublished.

[49] D.H. Whittum, "Introduction to Electrodynamics for Microwave Linear Accelerators." SLAC-PUB-7802, (1998):52-54, unpublished.

[50] Xiao, L., W. Gai, and X. Sun, "Field Analysis of a Dielectric-loaded Rectangular Waveguide accelerating Structure." *Physical Review E* 65 (2001): 016505.

[51] Jing, C., W. Liu, L. Xiao, W. Gai, and T. Wong, "Dipole-mode Wake fields in Dielectric-loaded Rectangular Waveguide Accelerating Structures." *Physical Reivew E* 68, (2003): 016502.

[52] Liu, W., "On the design of Dielectric Taper Section for Epislon=20.", WF-Note-206, Argonne National Laboratory, http://www.hep.anl.gov/pmalhotr/AWA .

[53] Maier, L.C. and J.C. Slater, "Field Strength Measurements in Resonant Cavities." *Journal of Applied Physics* 23, (1952): 68.

[54] Carter, R.G., "Accuracy of Microwave Cavity Perturbation Measurements." *IEEE Transaction on MTT* 49.5 (2001): 918-23.

[55] Steele, C.W., "A Nonresonant Perturbation Theory." *IEEE Transaction on MTT-14* 2 (1966):70-74.

[56] Collin R.E. *Field Theory of Guided Waves*, McGRAW-HILL Book Co., 1960, pp.525-530.

[57] Mallory, K.B. and R.H. Miller. "On Nonresonant Perturbation Measurements." *IEEE Transaction on MTT-14* 2 (1966): 99-100.

[58] Chou, P.J., "RF Measurements of a Traveling-Wave Muffin-Tin Accelerating Structure at 90GHz." *SLAC-PUB-7499*, May 1997, unpublished.

[59] Vaughn, J.R.M., "A New Formula for Secondary Emission Yield." *IEEE Transaction on Electron Device*s 36 (1989): 1963.

[60] Power, J.G., W. Gai, S.H. Gold, A.K. Kinkead, R. Konecny, C. Jing, W. Liu, and Z. Yusof, "Observation of Multipactor in an Alumina-Based Dielectric-Loaded Accelerating Structure." *Physical Review Letters* 92.16 (2004):164801.

[61] Ang, L.-K., Y.Y. Lau, R.A. Kishek, and R.M. Gilgenbach, "Power Deposited on a Dielectric by Multipactor." *IEEE Transaction on Plasma Science* 26 (1998): 290.

[62] Kishek, R.A. and Y.Y. Lau. "Multipactor Discharge on a Dielectric." *Physical Review Letters*, 80 (1998):193.

[63] CST Microwave Stuido®, developed by Computer Simulation Technology, Available at www.cst.com .

[64] Yeh, P. and A. Yariv. "Theory of Bragg Fiber." *Journal of Optical Society of America* 68 (1978): 1196-1201.

[65] Ibanescu, M., S.G. Johnson, M. Soljacic, J.D. Joannopoulos, Y. Fink, O. Weisberg, T.D. Engensess, S.A. Jacobs, and M. Skorobogatiy, "Analysis of Mode Structure in Hollow Dielectric Waveguide Fibers." *Physical Review E* 67 (2003): 046608.

[66] Harrington, J.A., "A Review of IR Transmitting, Hollow Waveguides." *Fiber and Integrated Optics* 19 (2000): 211-17.

[67] Johnson, S.G., M. Ibanescu, M. Skorobogatiy, O. Weisberg, T.D. Engeness, M. Soljacic, S.A. Jacobs, J.D. Joannopoulos, and Y. Fink, "Low-loss Asymptotically Single-mode Propagation in Large-core OmniGuide Fibers." *Optics Express* 9 (2001): 749-79.

[68] Xu, Y., R.K. Lee, and A. Yariv, "Asymptotic Analysis of Bragg Fiber." *Optics Letters* 25 (2000): 1756-1758.

[69] Xu, Y., G.X. Ouyang, R.K. Lee, and A. Yariv, "Asymptotic Matrix Theory of Bragg Fiber." *Journal of Lightwave Technology* 20 (2002): 428-40.

[70] Miyagi, M., A. Hongo, and S. Kawakami, "Transmission Characteristics of Dielectric-Coated Metallic Waveguides for Infrared Transmission: Slab Waveguide Model." *IEEE Journal of Quantum Electronics* QE-19, (1983): 136-45.

[71] Miyagi M. and S. Kawakami. "Design Theory of Dielectric-Coated Circular Metallic Waveguides for Infrared Transmission." *Journal of Lightwave Technology* 2 (1984):116-26.

[72] Schachter, L., R.L. Byer, and R.H. Siemann, "Wake Field in Dielectric Acceleration Structures." *Physical Review E* 68 (2003): 036502.

[73] Mizrahi, A., L. Schachter, R.L. Byer, and R.H. Siemann, "Dielectric Bragg Accelerator." *Proceedings of 2003 Particle Accelerator Conference*, Portland, OR, (2003): 728-30.

[74] Wang, C., V.P. Yakovlev, and J.L. Hirshifield, "Rectangular Dielectric-lined Accelerator Structure." *Proceedings of Advanced Accelerator Concepts 11th Workshop*, AIP Conference Proceedings. 737 New York, (2004): 871-79.

[75] Chou, R.C. and S.W. Lee. "Modal Attenuation in Multilayered Coated Waveguides." *IEEE Transaction on MTT-36* (1988): 1167-76.

[76] Lax, B. and K.J. Button. *Microwave Ferrites and Ferrimagnetics*, McGRAW-HILL, 1962, Chapter 8.

[77] Akyel, C. and R.G. Bosisio. "New Developments on Automated-Active Circuits for Permittivity Measurements at Microwave Frequencies." *IEEE Tran. on Instrumentation and Measurement* 38.2 (April 1989): 496-504.

[78] Tian, B. and W.R. Tinga. "A Microwave Oscillation Loop for Dielectric Constant Measurement." IEEE MTT-42 2 (Feb. 1994):169-76.

[79] Cevdet Akyel, Renato G. Bosisio and Georges-Emile April An Active Frequency Technique for Precise Measurements on Dynamic Microwave Cavity Perturbation *IEEE Tran. on Instrumentation and Measurement* 27.4 (Dec. 1978): 364-68.